Observational Studies of Supernovae and Intermediate Luminosity Optical Transients

Licentiate of Philosophy Thesis
University of Turku
Dept. of Physics and Astronomy
Astronomy
January 2020
M.Sc. Jussi Harmanen
Supervisors:
Prof. Seppo Mattila
Dr. Erkki Kankare
Examiners:
Prof. Juri Poutanen
Docent Mika Juvela

The originality of this thesis has been checked in accordance with the University of Turku quality assurance system using the Turnitin OriginalityCheck service.

TURUN YLIOPISTO – UNIVERSITY OF TURKU
Department of Physics and Astronomy

HARMANEN JUSSI: Observational Studies of Supernovae and Intermediate Luminosity Optical Transients

Licentiate of Philosophy Thesis, 78 p, 9 app.p.
Astronomy
April 2020

Thanks to modern all-sky surveys, thousands of astronomical transient events are discovered annually. Although many of these, such as regular supernovae (SNe), are fairly well understood, new rarer classes of transients have been discovered since the late 20th century. These include SNe interacting with dense circumstellar matter (CSM) and intermediate luminosity optical transients (ILOTs a.k.a. gap transients). Because of the limited number of facilities available, only a small fraction of all transients are spectroscopically classified.

As a part of international collaborations, I have participated in the acquisition and processing of data for classification and follow-up of a variety of transient events. The main telescopes used were the Nordic Optical Telescope and the European Southern Observatory's New Technology Telescope. The wavelength regions observed span from the optical to the near-infrared.

A total of 111 spectroscopic classifications and five selected follow-up papers that I have contributed to are discussed in this work. Two of the events, SNe 2015bh and 2016bdu are possibly produced by SNe interacting with CSM although other interpretations cannot be completely ruled out. The other three objects are ILOTs. SNhunt248 was likely produced either by an outburst from a yellow hypergiant star (SN impostor) or a binary merger (luminous red nova, LRN). The LRN M101 OT2015-1 was probably produced by a merger. A sub-energetic SN explosion in a dusty environment is favoured as the origin for the intermediate luminosity red transient (ILRT) AT 2017be.

Even though ILOTs share many common observable similarities, such as their early spectral features and maximum luminosities, there are distinguishable characteristics to each subclass. SN impostors exhibit strong variability prior to their outbursts. The progenitors of ILRTs are low mass stars (compared to other SN progenitors, that is) surrounded by dusty CSM. LRNe are produced by binary merger and they tend to develop molecular spectral lines during the later stages of their evolution.

In the case of so-called SN 2009ip -like transients (such as SNe 2015bh and 2016bdu), more data are required to fully understand these events. Although their photometric and spectral evolution is conspicuously similar, it is still not clear whether or not they are produced by a terminal SN explosion or, for instance, some erratic progenitor activity.

Keywords: instrumentation: detectors, spectrographs – stars: individual: SNhunt248, M101 OT2015-1 – supernovae: general – supernovae: individual: SN 2015bh, SN 2016bdu, AT 2017be – telescopes

TURUN YLIOPISTO – UNIVERSITY OF TURKU
Fysiikan ja tähtitieteen laitos

HARMANEN JUSSI: Observational Studies of Supernovae and Intermediate Luminosity Optical Transient

Filosofian lisensiaatintutkielma, 78 s, 9 liites.
Tähtitiede
Huhtikuu 2020

Jatkuvasti taivasta kartoittavien havainto-ohjelmien ansiosta tuhansia lyhytikäisiä tähtitieteellisiä kohteita löydetään vuosittain. Tavallisimmat näistä kohteista – kuten supernovat – ovat varsin hyvin ymmärrettyjä. Harvinaisemmille kohteille tämä ei päde. Harvinaisiksi lasketaan muun muassa viime vuosituhannen loppupuolelta alkaen löydetyt uudet kohteet, joihin kuuluvat esimerkiksi tiheän tähteä ympäröivän aineen kanssa vuorovaikuttavat supernovat ja keskikirkkaat lyhytikäiset optiset kohteet (ILOT-kohteet). Havaintolaitteiden määrän rajallisuudesta johtuen uusista kohteista luokitellaan kuitenkin vain pieni murtoosa.

Olen ollut mukana suurissa kansainvälisissä hankkeissa havaitsemassa ja käsittelemässä aineistoa monelle eri havaintokohteelle. Keskeisimmät käytössä olleet kaukoputket ovat Nordic Optical Telescope ja Euroopan eteläisen obsevatorion New Technology Telescope. Havainnot painottuivat näkyvän valon ja lähi-infrapunan alueille.

Tässä työssä esitellään 111 kohteen spektroskoopiset luokitukset ja viisi valittua artikkelia, joihin olen kerännyt ja käsitellyt havaintoaineistoa. Kaksi kohteista, SN 2015bh ja SN2016bdu, ovat todennäköisesti seurausta tähteä ympäröivän aineen kanssa vuorovaikuttavasta supernovasta, joskaan muita tulkintoja ei voi täysin sulkea pois. Kohteen SNhunt248 kirkastumiselle on esitetty kaksi mahdollista tulkintaa: keltaisen ylijättiläistähden purkaus tai kaksoistähtijärjestelmän yhteensulautuminen. Kohteelle M101 OT2015-1 on myös esitetty jälkimmäistä tulkintaa. Pölyisessä ympäristössä räjähtänyt matalaenergeettinen supernova on puolestaan todennäköisin selitys kohteelle AT 2017be.

Vaikkakin ILOT-kohteilla on yhteneväisiä havaittuja piirteitä, kuten spektrin yksityiskohtien kehitys ja kirkkauden maksimi, on jokaisella kohteella myös omat tunnusomaiset piirteensä. Esimerkiksi suuren tähden massiivista purkausta edeltää usein epästabiilisuus vuosien aikaskaalalla.

Niin kutsutuille SN 2009ip -tyyppisille kohteille – joita myös kohteet SN 2015bh ja SN2016bdu edustavat – lisähavainnot ovat tarpeen. Vaikkakin havaitut ominaisuudet ovat suurilta osin samat, ei vielä tiedetä, että ovatko nämä kohteet seurausta supernovaräjähdyksestä vai esimerkiksi tähden epästabiilisuudesta, joka tuottaa supernovaa muistuttavia havaittavia piirteitä.

Avainsanat: havaintovälineet: ilmaisimet, spektografit – tähdet: yksittäinen: SNhunt248, M101 OT2015-1 – supernovat: yleinen – supernovat: yksittäinen: SN 2015bh, SN 2016bdu, AT 2017be – kaukoputket

Contents

Acknowledgements **1**

List of abbreviations **2**

Introduction **3**

1 Supernovae **4**

1.1 Explosion mechanisms 4

1.1.1 Thermonuclear supernovae 4

1.1.2 Core–collapse and electron capture supernovae 5

1.1.3 Pair instability, magnetar formation and jets 11

1.2 Classification of Supernovae 13

1.2.1 Type Ia 13

1.2.2 Type Ib 13

1.2.3 Types Ic and Ic-BL 13

1.2.4 Types IIP and IIL 15

1.2.5 Type IIn 15

1.2.6 Types IIb and Ibn 15

1.2.7 Superluminous supernovae 17

1.3 Observed properties 17

1.3.1 Thermonuclear supernovae 17

1.3.2 Core–collapse supernovae 19

2 Interaction with circumstellar matter **23**

2.1 Spherically symmetric standard model 24

2.2 Numerical simulations 26

3 Intermediate luminosity optical transients **34**

3.1 Supernova impostors . . . 34
3.1.1 SN 2009ip . . . 39
3.2 Intermediate luminosity red transients . . . 42
3.2.1 SN 2008S . . . 42
3.3 Luminous red novae . . . 44
3.3.1 V838 Monocerotis . . . 44

4 Telescopes and instrumentation **47**
4.1 The Nordic Optical Telescope . . . 47
4.1.1 NOTCam . . . 47
4.1.2 ALFOSC . . . 48
4.2 The New Technology Telescope . . . 50
4.2.1 EFOSC2 . . . 50

5 Observing programmes **52**
5.1 NOT studentship . . . 52
5.2 Normal programmes . . . 54
5.2.1 Studies of peculiar supernovae with NOT and TNG . . . 54
5.2.2 Survey of nuclear transient in galaxies with Gaia . . . 55
5.3 Large programmes . . . 55
5.3.1 NUTS . . . 56
5.3.2 PESSTO and ePESSTO . . . 57
5.4 Summary . . . 58

6 Results **59**
6.1 Astronomer's Telegrams . . . 59
6.2 Journal Articles . . . 62
6.2.1 SNhunt248 . . . 63
6.2.2 SN 2015bh . . . 65

6.2.3 M101 OT2015-1 68
6.2.4 SN 2016bdu 71
6.2.5 AT 2017be 74
6.3 Discussion 75

7 Conclusions **78**

References **79**

Appendix **85**

A Transient classifications **85**

B Journal articles **90**

Acknowledgements

I would like to thank my supervisors Seppo and Erkki who introduced me to the transient astronomy already in summer 2011 when I worked as a research intern at the Tuorla observatory. They have guided me ever since. I would also like to thank the examiners of this particular work, Juri Poutanen (University of Turku) and Mika Juvela (University of Helsinki).

I would like to recognise the importance of the education and support from both staff and students of Tuorla observatory (especially the all-knowing coffee table) and the Nordic Optical Telescope. Furthermore, I would like to appreciate the opportunities provided by the (extended) Public ESO Spectroscopic Survey of Transient Objects collaboration.

For their financial support for this work, I would like to acknowledge the Nordic Optical Telescope Scientific Association, The Finnish Cultural Foundation and the Vilho, Yrjö and Kalle Väisälä Foundation of the Finnish Academy of Science and Letters.

Finally, I am eternally grateful for my parents, Mauri and Marja, who have always been there to support my journey.

List of abbreviations

AGN - active galactic nucleus

ALFOSC - Alhambra Faint Object Spectrograph and Camera

ATel - Astronomer's telegram

BH - black hole

BSG - blue supergiant

BL - broad line

CC - core collapse

CE - common envelope

CV - cataclysmic variable

CCD - charge-coupled device

CDS - cool dense shell

CCSN - core–collapse supernova

CSM - circumstellar matter

EC - electron capture

EDP - electron degeneracy pressure

EFOSC2 - ESO Faint Object Spectrograph and Camera v.2

EOS - equation of state

(e)PESSTO - (extended) public ESO spectroscopic survey for transient objects

ESO - European Southern Observatory

FIES - fibre-fed echelle spectrograph

HR - high resolution

HST - *Hubble Space Telescope*

ILOT - intermediate luminosity optical transient

ILRT - intermediate luminosity red transient

IR - infrared

LBV - luminous blue variable

LRN - luminous red nova

MOS - multi-object spectroscopy

NOT - Nordic Optical Telescope

NOTCam - Nordic Optical Telescope Near-Infrared Camera and Spectrograph

NS - neutron star

NTT - New Technology Telescope

NUTS - NOT Unbiased Transient Survey

OB - observing block

PI - principal investigator

PNS - proto-neutron star

PP - pair production

RLOF - Roche lobe overflow

RSG - red supergiant

SASI - standing accretion shock instability

SN - supernova

SSA - student support astronomer

TDE - tidal disruption event

TNG - Telescopio Nazionale Galileo

ToO - target of opportunity

UV - ultraviolet

WD - white dwarf

WF - wide field

YHG - yellow hypergiant

Introduction

Thanks to modern all-sky surveys, thousands of astronomical transients are discovered every year. A vast majority of *extragalactic* transients observed are supernovae (SNe). This is due to their immense brightness that enables us to observe them over vast distances. Our understanding of them has increased throughout the past century or so, especially during the previous few decades. Still, the theory to fully describe them is far from complete. Only by classifying and monitoring these events we can, piece by piece, hope to understand their nature. Of course, it is impossible to spectroscopically classify all transients due to the limited number of facilities and observing time.

In some rarer cases, a SN progenitor star has a dense circumstellar medium (CSM) around it at the time of the explosion. This produces clear imprints on the observable properties of these so-called interacting SNe. Other processes, such as outbursts of massive stars, can produce transients with similarities making it difficult to separate these events.

With the increasing effort to classify as many transients as possible, new types of objects have been discovered during the recent years. Intermediate Luminosity Optical Transients (ILOTs) display peak brightnesses in between novae and supernovae. Additionally, the spectral features are often reminiscent of those displayed by interacting SNe, making ILOTs even more interesting targets.

This thesis is structured as follows. The first three sections provide introduction to various topics: the theory, observables and classification of SN explosions in Section 1; the theory and observables of SN interaction with CSM in Section 2; and the theory and observables of ILOTs in Section 3. Sections 4 and 5 provide descriptions of the main telescopes and observing programmes, respectively, that enabled this work. In Section 6, the results of SN classifications and selected articles are reviewed and additional remarks to them provided. Finally, the main conclusions are presented in Section 7.

1 Supernovae

Theory and observed properties of SNe are briefly reviewed in this section. First, the theory behind SN explosions is discussed in Section 1.1. Then, an introduction to the classification scheme of SNe is described in Section 1.2 and, finally, certain observed properties of SNe are explained and linked to theory and classification in Section 1.3.

1.1 Explosion mechanisms

The vast majority of SNe are caused either by a thermonuclear explosion of a white dwarf (WD) star or core collapse (CC) in a massive star. Additional explosion mechanisms have been proposed to explain some of the more peculiar SNe, such as sub/superluminous events. Additionally, SN ejecta interacting with dense CSM plays a key role in the display of some SNe.

1.1.1 Thermonuclear supernovae

As core–collapse supernovae (CCSNe) and SN impostors are the main topic of this thesis, thermonuclear SNe are only briefly addressed here.

Type Ia SNe are caused by thermonuclear explosions of carbon-oxygen (C/O) WDs. These WDs are steadily produced by stars of $M_{\mathrm{ZAMS}} \sim 0.5 - 8$ $\mathrm{M}_{\odot}$[1] as end products of their lives. (Laughlin et al., 1997; Herwig, 2002)

In order for a C/O WD to explode, it has to grow in mass up until the Chandrasekhar limit ($M \sim 1.4$ $\mathrm{M}_{\odot}$) when the instabilities in the star trigger the explosion. Although the specific circumstances leading to a thermonuclear explosion are highly debated, the general idea is quite well understood. As a WD grows in mass, the self-gravity tends to collapse the star. As no nuclear burning is taking place, electron degeneracy pressure (EDP) is halting the collapse. As the Chandrasekhar limit is reached, the nuclear matter is

[1] M_{ZAMS} is the Zero Age Main Sequence mass i.e. the mass of a star when it enters the main sequence in the Hertzsprung-Russell diagram.

highly degenerate, and the following ignition of C/O leads to a runaway fusion reaction. As a consequence, a shock front travels through the star leading to a SN explosion which completely obliterates the star. See e.g. Hillebrandt & Niemeyer (2000) for a review of different models.

There are two main paths to achieve the critical mass. In the classical model a WD has a binary companion which evolves out of the main sequence. Under certain conditions this causes a mass overflow onto the WD via, for instance, the Roche lobe overflow (RLOF) or stellar wind. If the mass accretion is sufficient enough and nova eruptions do not eject too much mass, the limit can be reached. This is known as the single degenerate channel to SNe Ia. (Maoz, 2014)

There is more and more observational evidence that binary WD mergers may have a significant contribution to the population of Type Ia SNe. In this scenario, two WDs eventually exceed the Chandrasekhar limit by merging. It is unclear, however, whether or not the merging immediately leads to an explosion even if the total mass exceeds the limit. Additional, although far less likely, scenario is a direct collision of two WDs. These are known as the double degenerate scenarios. (Maoz, 2014)

Even though the theory is fairly well established, a direct confirmation of SN Ia progenitors is still missing. The Milky Way has a number of candidates, such as cataclysmic variables, but the SN Ia rate has been estimated to be low. Li et al. (2011b) estimated a rate of 0.54 ± 0.12 $(100\ \mathrm{yr})^{-1}$ based on the observations by the Lick Observatory Supernova Search (LOSS) and by averaging results from different galaxy type and luminosity assumptions for the Milky Way. (Maoz, 2014)

1.1.2 Core–collapse and electron capture supernovae

Massive stars ($M_{\mathrm{ZAMS}} \gtrsim 8\ \mathrm{M}_{\odot}$) are able to burn elements all the way to the iron group in their cores. At the end they are believed to have an onion-like structure of elements formed during the different burning stages. Starting from the Fe core the different layers

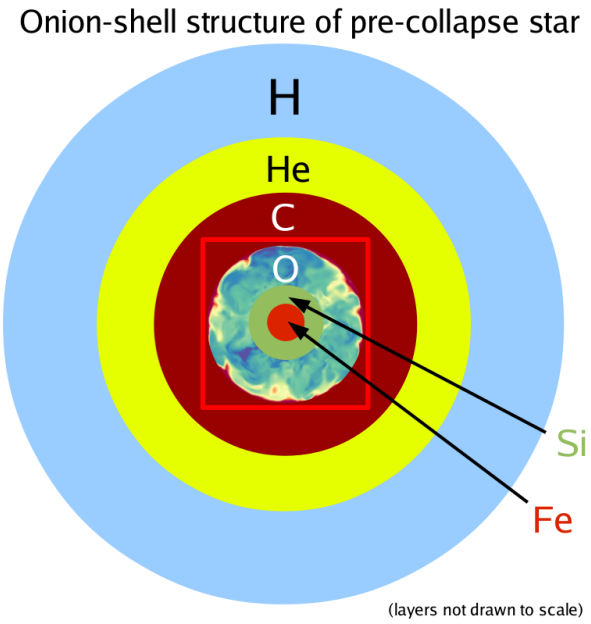

Figure 1. The schematic configuration of a CCSN progenitor star prior to explosion. The red box indicates a zoom-in to the collapsing region shown in detail in Fig. 2. Perturbations caused by the convective burning in O and Si layers are explicitly shown. These perturbations alter the exact structures of the progenitors whereas the cores are practically identical. Adopted from Janka (2017).

consist of progressively lighter elements towards the surface up until the H envelope (see Fig. 1). Of course, this is a schematic picture as some mixing does take place throughout the evolution of these stars (e.g. dredge-up episodes). See e.g. reviews by Smartt (2009) and Langer (2012) on SN progenitors.

The basic idea of the CC mechanism is well-established: an Fe core of a massive star collapses triggering a SN explosion. Even though the process has been studied for several decades (see e.g. reviews by Burrows (2013) and Janka (2017)), the exact details leading to a successful SN explosion are not fully understood. The input physics are numerically heavy to calculate as the conditions in the stellar cores are extreme. With increasing computing power it has been only recently possible to include full dimensionality and as realistic physics as possible to these simulations.

The process from the onset of the collapse to the SN explosion is described below and shown in the six panels of Fig. 2. All six steps are as described in detail by Janka (2017).

Fig. 2, upper left panel: As the Fe core grows in mass, the EDP increases since the gravity tends to compress the core. Eventually the density of the inner core (ρ_c) reaches a critical value of $\rho_c \sim 10^9 - 10^{10}$ g cm^{-3} (depending on the progenitor mass). As the threshold is reached, electrons (e^-) are captured by the protons in nuclei ($X(A,Z)$) and by free protons (p) producing a flux of electron neutrinos (ν_e) and neutrons (n):

$$e^- + X(A,Z) \longrightarrow \nu_e + X(A,Z-1), \tag{1}$$

$$e^- + p \longrightarrow \nu_e + n, \tag{2}$$

where A and Z are the mass and atomic number, respectively, of a given nucleus. Additionally, a fraction of the nuclei are photodissociated to free nucleons and α particles that further enhance the rate of electron capturing (Ivanov & Shulman, 1990):

$$^{56}\mathrm{Fe} + \gamma \rightleftharpoons 13\alpha + 4n \tag{3}$$

$$^{4}\mathrm{He} + \gamma \rightleftharpoons 2p + 2n. \tag{4}$$

As the electrons are captured, the electron degeneracy is lifted and the EDP decreases. As a consequence, the internal pressure in the core suddenly drops and triggers the collapse that further increases the density. At first, the neutrinos are able to freely escape from the core. While the density in the inner core increases, however, the mean free path of the neutrinos is decreasing. At $\rho_c \sim 10^{11}$ g cm^{-3}, the neutrinos are forced to diffuse out by the scattering from the heavy nuclei. Eventually, at $\rho_c \sim 10^{12}$ g cm^{-3}, the neutrinos are trapped as the diffusion timescales become larger than the infall of the outer core. (Janka, 2017)

Fig. 2, upper right: Free collapse of the inner core is finally stopped when the nuclear saturation density ($\rho \sim 10^{14}$ g cm^{-3}) is reached and the equation of state (EOS) stiffens. This is due to the nucleon-nucleon repulsion i.e. the nucleon gas cannot be compressed further. A proto-neutron star (PNS) is formed. Since the EOS stiffening occurs when the compression has already overshot the equilibrium state, the PNS expands (bounces). This creates a pressure wave propagating outwards which, upon hitting the supersonically

infalling outer core, steepens into a shock wave. (Janka, 2017)

Fig. 2, middle left: While the shock propagates through the infalling outer core, kinetic energy is effectively transformed to increase the temperature at the shock. As a consequence, high-energy photons that are able to disintegrate Fe into free nucleons, are created. About a millisecond after the bounce the shock wave has slowed down due to the pressure drop in the post-shock region caused by the dissipation of kinetic energy. At this point the shock is still located within the outer core. The density in the post-shock region has also decreased and the neutrinos produced by electron capture (EC) by free protons are able to escape freely. This further increases the energy losses behind the shock. These lead to stalling of the shock at which point it turns into an accretion shock. (Janka, 2017)

Fig. 2, middle right: Post-shock region becomes radiation-dominated as the aforementioned processes decrease the temperature and density in it. Simultaneously, the neutrino spectrum from the PNS hardens. In combination, these lead to increase in the fraction of neutrinos absorbed by the free protons and neutrons (while producing electrons and positrons (e^+)):

$$\nu_e + n \longrightarrow p + e^-, \tag{5}$$

$$\nu_e + p \longrightarrow n + e^+, \tag{6}$$

that is effectively heating up the shock. This, in turn, leads to instabilities in the post-shock region. The so called standing accretion shock instability (SASI) grows and deforms the shock front which causes stirring in the whole post-shock region. This may lead to formation of non-uniform entropy structures which further increases the neutrino heating efficiency. (Janka, 2017)

Fig. 2, bottom left: As a consequence of the neutrino heating of the shock, the pressure in the post-shock region increases. If this increase is high enough, the shock is revived and it continues propagating outwards. SASI and other instabilities increase the neutrino heating efficiency by, for instance, expanding the shock region and thus increasing the volume where the neutrino absorption occurs. If the shock is able to overcome the rest of

the infalling outer core, a SN explosion is inevitable. At that point the shock also triggers explosive nucleosynthesis that produces heavy elements such as radioactive ^{56}Ni (Eq. 9). It takes several hours for the shock to propagate all the way through the progenitor. (Janka, 2017)

Fig. 2, bottom right: Neutrino energy deposition launches a wind of free protons and neutrons from the surface of the newly-born neutron star (NS). This may, depending on the proton/neutron fraction, eventually lead to certain interesting nucleosynthesis as the wind expands and cools. (Janka, 2017)

As already mentioned, even after decades of advancement in theory, the understanding of the neutrino-driven explosion is far from being fully understood. Although modern computational facilities have allowed hydrodynamical simulations to be performed in 3D, there are still several limitations in computing these models. These include, for instance, approximations in the applied neutrino transport and grid resolution. Additionally, the growing instabilities during the post-bounce phase tend to break the spherical symmetry further increasing the numerical complexity. (Janka, 2017)

The only direct observational evidence to support the CC scenario so far is the neutrinos observed simultaneously with the optical brightening of SN 1987A, which exploded in the Large Magellanic Cloud in 1987 (Hirata et al., 1987). Current and future neutrino and gravitational wave facilities will have a huge impact in constraining the CC mechanism whenever the next Galactic CCSN explodes. (Janka, 2017)

Some theoretical models predict that stars at the lower limit of SN progenitor masses (in a narrow mass range around $\sim 8 - 10$ $M_{\odot}$) could explode already before the onset of Si burning. At this stage the star has formed an ONeMg core which grows in mass due to the C burning around it. As the pressure rises, the electron degeneracy increases as well. However, the conditions at the core are not adequate to ignite the Ne burning. Eventually, the density in the core exceeds certain critical values after which a chain of certain EC

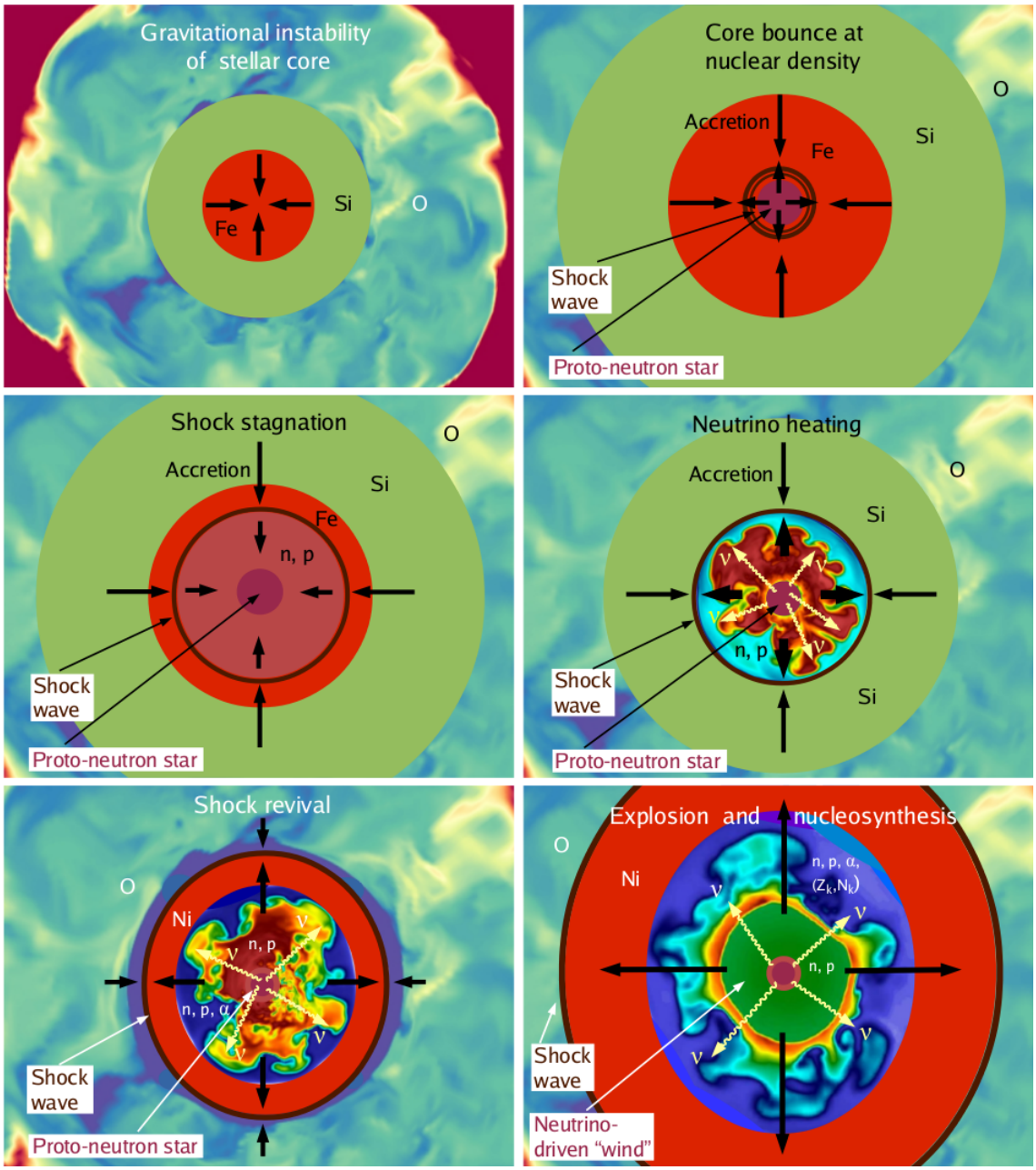

Figure 2. Stages of the neutrino-driven explosion explained in the text. Different layers are not in scale. Non-uniformly coloured regions (O shell convection, post-shock instabilities) are actually superimposed results of various simulations. Horizontal scales range from $\sim 5 \cdot 10^4$ km (upper left) to $\sim 2 \cdot 10^3$ km (bottom left). Adopted from Janka (2017).

reactions occur:

$$e^- + {}^{24}\mathrm{Mg} \longrightarrow {}^{24}\mathrm{Na} + \nu_e \qquad (\rho_c \approx 4 \cdot 10^9\,\mathrm{g\,cm^{-3}}) \tag{7}$$
$$e^- + {}^{24}\mathrm{Na} \longrightarrow {}^{24}\mathrm{Ne} + \nu_e$$

and

$$e^- + {}^{20}\mathrm{Ne} \longrightarrow {}^{20}\mathrm{F} + \nu_e \qquad (\rho_c \approx 5 \cdot 10^9\,\mathrm{g\,cm^{-3}}) \tag{8}$$
$$e^- + {}^{20}\mathrm{F} \longrightarrow {}^{20}\mathrm{O} + \nu_e,$$

where ρ_c indicates the threshold density in the core required by the first reaction in the chain. (Nomoto, 1987)

As the electrons are captured, the EDP diminishes and the core starts to contract thus further increasing the density. Because of the compression, the temperature in the core also increases. At $\rho_c = 2.4 \cdot 10^{10}$ g cm^{-3} the O burning rate reaches a critical point and a deflagration front is formed. As a consequence, the rate of the EC reactions goes up additionally increasing the contraction of the core. (Nomoto, 1987)

Although this process is slower than Fe CC[2], the end result is similar: a PNS is formed due to neutronisation of matter and a shock front produced by the core bounce triggers the explosion. However, this EC mechanism is expected to produce weaker explosions than Fe CCSNe. (Nomoto, 1987)

1.1.3 Pair instability, magnetar formation and jets

While the CC mechanism is indeed able to explain the observed energetics of normal SNe, an additional energy source is required to explain superluminous supernovae (SLSNe). Several models have been suggested in the literature. Although these models often require certain specific conditions to occur, they are usually able to reproduce the properties of some of the most energetic SNe observed.

[2] Although Fe CC is also caused by electron capture (see Eq. 1), SNe caused by the collapse of an ONeMg core are usually called as electron-capture SNe (ECSNe) in the literature.

It is fairly intuitive to think that perhaps extremely massive stars produce energetic explosions. Fowler & Hoyle (1964) demonstrated that instabilities caused by electron-positron pair-production (PP) in the cores of massive ($M_{\mathrm{ZAMS}} \gtrsim 100\ \mathrm{M}_{\odot}$), metal-poor stars are able produce a SN explosion. It is believed that in such massive stars the core reaches high enough temperatures and densities for considerable PP to occur already before the O ignition. As internal energy is effectively converted to the mass of electron-positron pairs, pressure is quickly lost and the core contracts rapidly. This leads to explosive O burning which completely disrupts the star. If the O mass is high enough ($M_{\mathrm{ZAMS}} \gtrsim 240\ \mathrm{M}_{\odot}$) even the O ignition is not enough to reverse the contraction and the core collapses directly into a black hole (BH). See Heger & Woosley (2002) and references therein.

Duncan & Thompson (1992) showed that if a strong dynamo is produced during the formation of a NS, a strong magnetic field ($B \sim 10^{15}$ G) is induced if the rotation period of the star is short enough ($P \sim 1$ ms). They also coined the term magnetar for these stars. Kasen & Bildsten (2010) modeled the effect of magnetar spin-down energy losses via magnetic dipole radiation to the expanding SN ejecta. They demonstrated that this mechanism is able to explain the light curve evolution of some SLSNe up to $E_{rad} \sim 10^{52}$ ergs.

An alternative to the core bounce model is a proposed scenario in which an accretion disk is formed around the PNS during the collapse. A process similar to the one believed to be powering active galactic nuclei launches bipolar jets that eventually eject the stellar envelope. Due to the mildly relativistic velocities of the jets, this process can also explain why many long gamma-ray bursts have been observed with an accompanying SN explosion. In case the core collapses directly into a BH, the model is also able to explain the energetics of SLSNe. This model requires, however, several strict assumptions starting from the fact that a disk has to form. See Soker (2010) and references therein.

1.2 Classification of Supernovae

Classification of SNe is based on their observed properties in the optical light. The first classification scheme was introduced by Minkowski (1941) based on the lines of hydrogen in the spectrum. If H is not detected, the SN is of Type I whereas Type II SNe show prominent H lines. Various subclasses of SNe have since been introduced as increasing amount of observational data has shown that the original scheme is insufficient. Main classification features are seen in the spectra of SNe around the time of the maximum light[3]. Additionally, the light curve evolution is used in certain subclasses. (Filippenko, 1997; Gal-Yam, 2016)

1.2.1 Type Ia

Type Ia SNe are characterised by prominent absorption features of Si II – 6150 Å being the strongest – and S II. Additionally, the lines of some other intermediate-mass elements are typically visible in the spectra, e.g. Ca II and O I. Examples of Type Ia SN spectra are shown in Fig. 3. (Gal-Yam, 2016)

1.2.2 Type Ib

The main features in the spectra of Type Ib SNe are the prominent absorption lines of He I at 5876, 6678 and 7065 Å. Additionally, a shallow absorption feature of O I at 7774 Å is typical. Examples of Type Ib SN spectra are shown in Fig. 4. (Gal-Yam, 2016)

1.2.3 Types Ic and Ic-BL

Type Ic SNe are spectroscopically similar to Ib SNe except, by definition, they do not show any He features. Type Ic events showing broad lines (BLs) are dubbed as Ic-BL. A

[3]Unless defined otherwise, the maximum light means the measured brigthness peak on a given wavelength band.

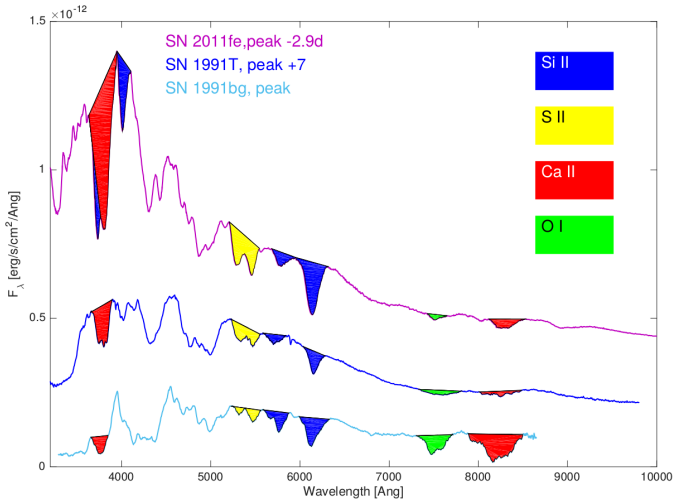

Figure 3. Spectra of various SNe Ia around the maximum light: normal SN 2011fe (Mazzali et al., 2014), overluminous SN 1991T (Filippenko et al., 1992a) and subluminous SN 1991bg (Filippenko et al., 1992b). Characteristic features are highlighted. Adopted from Gal-Yam (2016)

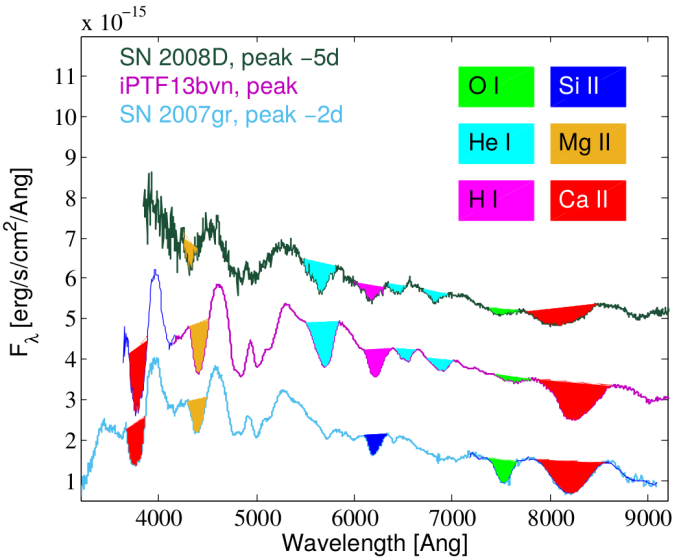

Figure 4. Comparison of normal Type Ib SNe 2008D (Modjaz et al., 2009) and iPTF 13bvn (Cao et al., 2013) to a normal Type Ic SN 2007gr (Valenti et al., 2008) around the maximum light. Note that although a possible H feature is mentioned here, it does not mean that these SNe are of Type II (see Fig. 6). The origin of this feature is debated. Adopted from Gal-Yam (2016)

comparison of a SN Ic to Type Ib SNe is shown in Fig. 4 and to Type Ic-BL SNe in Fig. 5. (Gal-Yam, 2016)

1.2.4 Types IIP and IIL

Events showing strong, broad Balmer emission lines[4] are classified as Type II SNe. Typically Hα shows a prominent P Cygni profile. Historically, normal Type II SNe have been further classified as Type IIL (linear) or Type IIP (plateau) depending on the light curve evolution after maximum light (Barbon et al., 1979). In recent years, however, observational evidence has suggested that there are no different subgroups of normal Type II SNe but a continuum of different light curve shapes (see e.g. Anderson et al. (2014); Sanders et al. (2015); Galbany et al. (2016); Valenti et al. (2016); de Jaeger et al. (2018)). The debate is still on-going (see e.g. Li et al. (2011a); Arcavi et al. (2012); Faran et al. (2014)). See Fig. 6 for spectral examples. (Gal-Yam, 2016)

1.2.5 Type IIn

Events showing narrow Balmer emission lines are classified as Type IIn SNe. This class is the most heterogeneous one. For instance, the line profiles may have multiple components. See Fig. 7 for spectral examples. (Gal-Yam, 2016)

1.2.6 Types IIb and Ibn

Type IIb SNe show prominent H features at first, but later on spectroscopically evolve towards Ib SNe i.e. the H lines fade while He lines grow stronger. Type Ibn SNe are characterised by narrow He emission lines analogous to SNe IIn showing narrow H lines. Some Type Ibn SNe, however, develop evidence of H in their spectra (see Pastorello et al. (2016) and references therein). (Gal-Yam, 2016)

[4] Hα: 6563 Å, Hβ: 4861 Å, Hγ: 4341 Å, Hδ: 4102 Å, Hϵ: 3970 Å, …

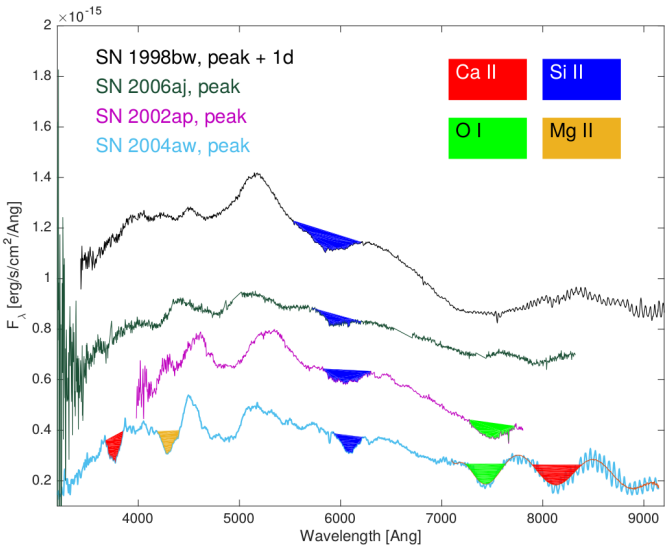

Figure 5. Examples of SNe Ic-BL: SN 1998bw (Patat et al., 2001), SN 2006aj (Pian et al., 2006), SN 2002ap (Gal-Yam et al., 2002) and SN 2004aw (Taubenberger et al., 2006). SN 2004aw is considered to be a transitional object showing some line broadening as well as the typical Ic features. Adopted from Gal-Yam (2016).

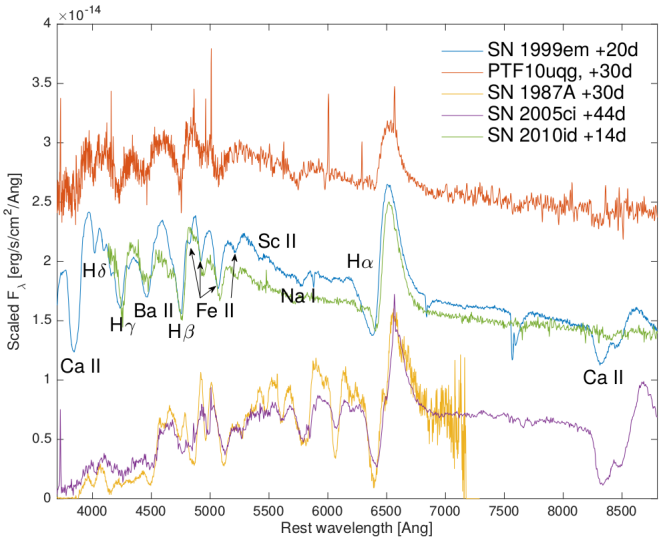

Figure 6. Selection of spectroscopically normal Type II SNe in photospheric phase: SN 1999em with long plateau (IIP) after the maximum light (Hamuy et al., 2001), PTF 10uqg showing a steep decline (IIL) after the maximum (Rubin et al., 2016), atypical SN 1987A (Pun et al., 1995) and SN 2005ci with a slow rise to maximum (Taddia et al., 2016). Subluminous event SN 2010id (Gal-Yam et al., 2011) is shown for comparison. Adopted from Gal-Yam (2016).

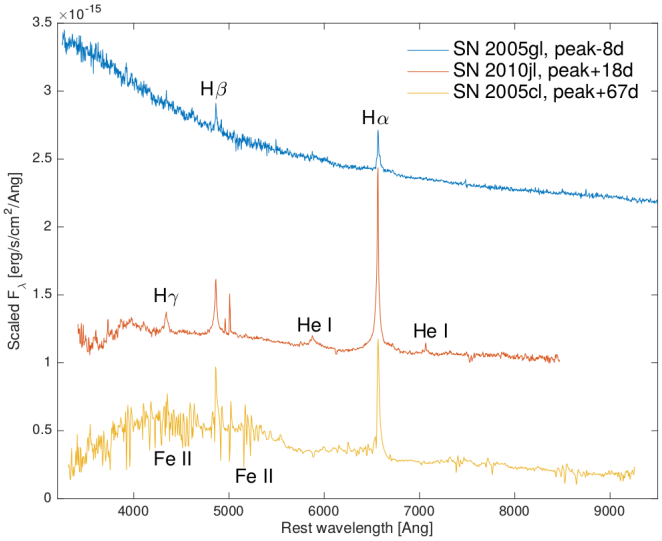

Figure 7. Three Type IIn SNe at different phases: pre-maximum spectrum of SN 2005gl (Gal-Yam et al. (2007), see also Fig. 37), post-maximum spectrum of overluminous and long-lasting SN 2010jl (Zhang et al., 2012) and late-phase spectrum of SN 2005cl showing several Fe II lines in the blue wavelengths (Kiewe et al., 2012). Adopted from Gal-Yam (2016).

1.2.7 Superluminous supernovae

As suggested by their name, SLSNe are brighter than normal SNe. The limiting absolute magnitude at the maximum brightness is defined as $M = -21$ mag in the optical light. They are, therefore, more than one magnitude brighter than the brightest among normal SNe. Further subclassification to Type I (SLSNe–I) or Type II (SLSNe–II) is based on the presence of H in their spectra similarly to the original SN classification by Minkowski. See Fig. 8. (Gal-Yam, 2016)

1.3 Observed properties

In the following, certain key properties and their origin in selected SN types are discussed.

1.3.1 Thermonuclear supernovae

In principle, the shock breakout should be observable as a brief γ-ray flash followed by a short duration brightening in the ultraviolet (UV) and optical wavelengths caused by

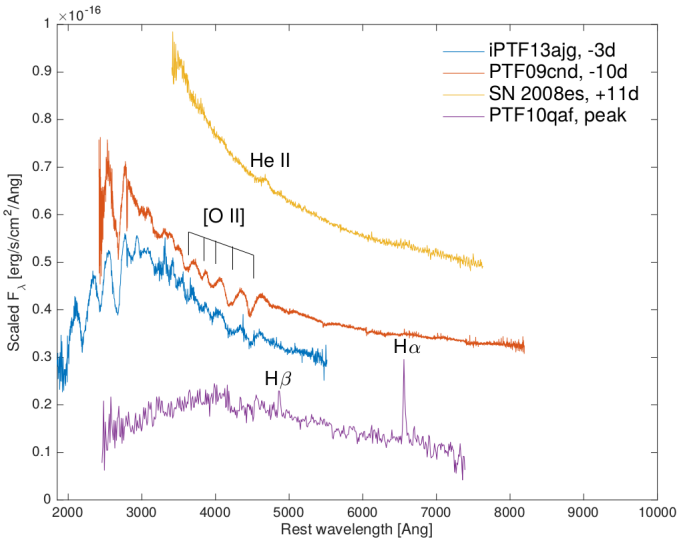

Figure 8. Selected spectra of SLSNe around the maximum light. Typical features of SLSNe–I (e.g. PTF 09cnd (Quimby et al., 2011) and iPTF13ajg (Vreeswijk et al., 2014)) are [O II] lines and strong absorption in the ultraviolet. By definition, SLSNe–II show H emission lines (e.g. PTF 10qaf (Gal-Yam et al., 2012)) although it might take some time for the features to develop (e.g. SN 2008es (Gezari et al., 2009)). Adopted from Gal-Yam (2016).

the shock heating of the ejecta. However, the main brightening follows a few days after the detonation when the photons created by the radioactive decay of the heavy elements formed in the explosion are diffusing out. (Maoz, 2014)

The main power source at early times is known to be the radioactive decay of ^{56}Ni via chain

$$^{56}\mathrm{Ni} \xrightarrow{6\,\mathrm{d}} {}^{56}\mathrm{Co} \xrightarrow{77\,\mathrm{d}} {}^{56}\mathrm{Fe}, \tag{9}$$

where the approximate half-lives of the isotopes are shown in days (Colgate & McKee, 1969). These decays produce γ-rays and positrons which, after being reprocessed while diffusing through the ejecta, have their energy emitted on the optical wavelengths. The optical luminosities at the maximum light are typically on the order of $\sim 10^{43}$ erg s^{-1}, while the total kinetic energy of the ejecta is usually $\sim 10^{51}$ erg. (Maoz, 2014)

Thanks to the similarity of the progenitors of Type Ia SNe, they can be used as standard candles making use of a strong correlation between their maximum luminosity and the light curve evolution around the maximum light. A larger amount of synthesized ^{56}Ni

produces brighter explosions. Additionally, increase in the amount of iron-group elements produced causes broadening of the light curve as the opacity is increased as well. As shown in Fig. 9, they typically (depending on the observed band) have a brightening period of $\sim 2-3$ weeks followed by a drop of ~ 3 magnitudes in one month and ~ 1 magnitude per month after the initial drop. This makes them an important tool in cosmology as standard candles. The acceleration of the expansion of the Universe was discovered using SNe Ia as distance indicators (Riess et al., 1998; Perlmutter et al., 1999). (Maoz, 2014)

1.3.2 Core–collapse supernovae

What happens after the central collapse is better, but not completely, understood. In addition to the explosive nucleosynthesis in inner regions of the star, the outward propagating shock ejects and ionises the overlaying layers of stellar matter. In case of H rich progenitors (Types IIP/L, IIb, IIn), it is believed that the ionisation has an important effect on the observed properties. For a more thorough description of the following three stages, see Arcavi (2017) and references therein.

When reaching the surface of the star, the shock front produces a short (minutes to hours long) flash of light in X-ray and UV energies. Due to the very short window in time and limited facilities available in these wavelength regions, this "shock breakout" has been rarely observed, e.g. SN 2008D (Chevalier & Fransson, 2008) and PS1-13arp (Gezari et al., 2015).

Cooling of the shock-ionised H-rich ejecta produces a more pronounced effect. While the ejecta cools as it expands (with kinetic energy on the order of $\sim 10^{51} - 10^{52}$ erg depending on the progenitor/SN type, Smartt (2009)), the H ionisation temperature front moves inwards in mass coordinates (i.e. towards the centre of the mass). This creates an inwards-moving H recombination front within the outwards-expanding ejecta effectively creating a more or less constant photosphere (in radius and temperature) at the recombination front. This is caused by the fact that neutral H outside the front is transparent to

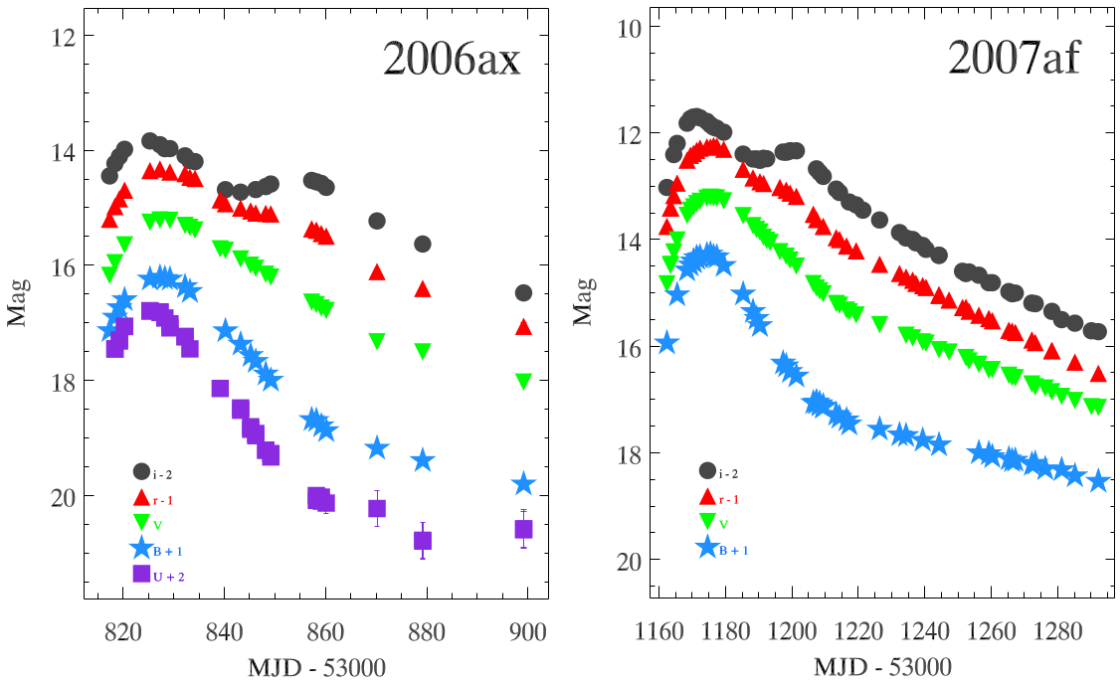

Figure 9. Multi-band optical light curves of normal SNe Ia: SN 2006ax and SN 2007af. Three phases of evolution mentioned in the text are clearly seen in the bluer bands. Faster evolution in U and B bands as well as the typical secondary peak in the i-band are caused by the line blanketing and opacity change effects of Fe and Co *within* the receding photosphere (see e.g. Dhawan et al. (2015) and references therein). In short, the emission from the radioactive decay (Eq. 9) is effectively shifted towards redder wavelengths as the ejecta expands. Adopted from Hicken et al. (2009).

continuum radiation whereas the ionised H (or free electrons, to be more precise) causes Thompson scattering within the front. This stage of evolution is known as the "plateau phase" and is shown schematically in Fig. 10.

After the expanding H envelope has fully recombined, the main energy source left to power the SN luminosity is believed to be the radioactive decay of ^{56}Co (Eq. 9) produced in the explosion deep within the progenitor by the shock. Due to the down-scattering in energy while diffusing outwards, the photons emerge mostly in the optical/near-infrared wavelengths. This stage is known as the "radioactive tail phase" due to the power source.

To demonstrate the effect of the H envelope mass on the light curves, two extreme examples are considered: a H-rich Type IIP SN 2013ab in Fig. 11 and a H-deficient Type IIb SN 1993J in Fig. 12. It is instantly clear that, although spectroscopically both are

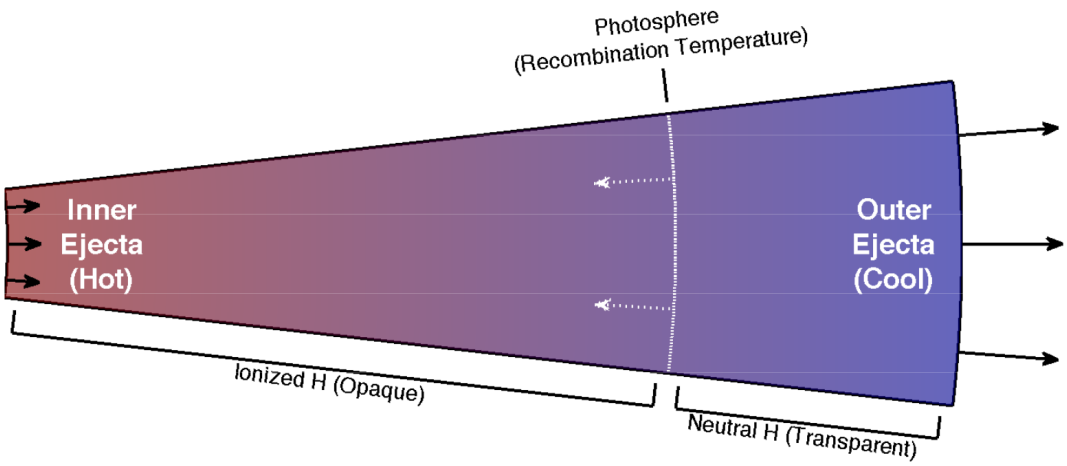

Figure 10. A slice of H-rich ejecta in Type IIP SN. Black arrows show the direction of expansion whereas white arrows show the direction of the recombination front (photosphere). Temperature outside the front is lower than the H ionisation temperature. H within the recombination front is still ionised and therefore optically thick. Adopted from Arcavi (2017)

showing H at early times, these SNe have completely different luminosity evolution.

H-rich SN 2013ab has a clear plateau lasting for months. This is due to the nearly-constant photosphere formed in the ejecta. Faster drop in the bluer bands is due to line blanketing effects, which are increasing when the photosphere recedes in mass coordinates. Sudden drop at around 100 days post-explosion means that all H has recombined and the radioactive tail phase has started. ^{56}Co decay, of course, contributes to the luminosity already earlier but is minuscule in comparison to the luminosity from the cooling H-rich ejecta. (Arcavi, 2017)

The light curves of SN 1993J, on the other hand, show two maxima. This is due to the lower H envelope mass at the time of the explosion. It takes only a short period of time for the H to cool after which the radioactive decay is the main power source. It is also easy to see that the diffusion from the inner parts (where the decay mostly happens) takes some time as the second maximum, in this case, occurs few weeks after the explosion. (Arcavi, 2017)

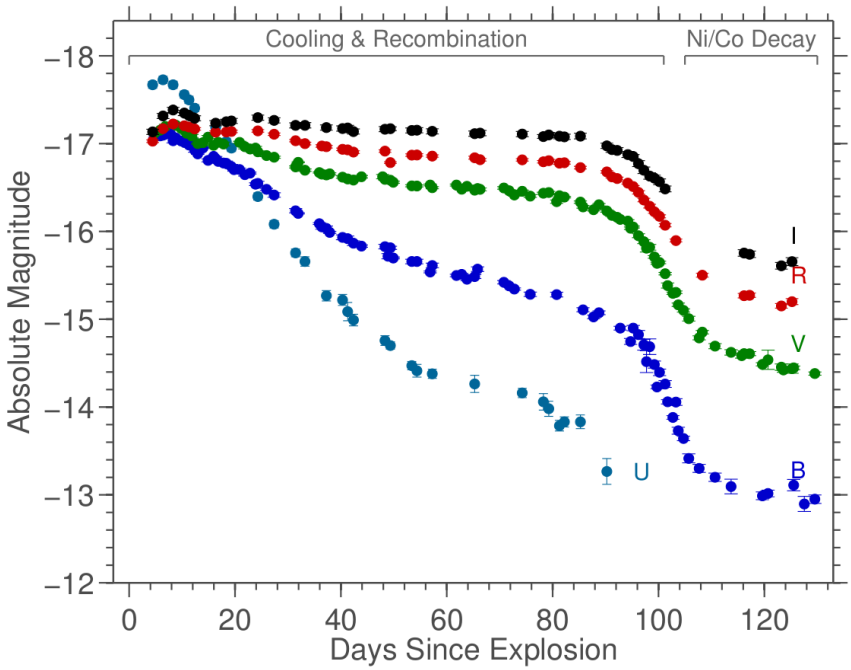

Figure 11. Multi-band light curves of Type IIP SN 2013ab (Bose et al., 2015). A plateau lasting about 100 days is clearly observed. Adopted from Arcavi (2017)

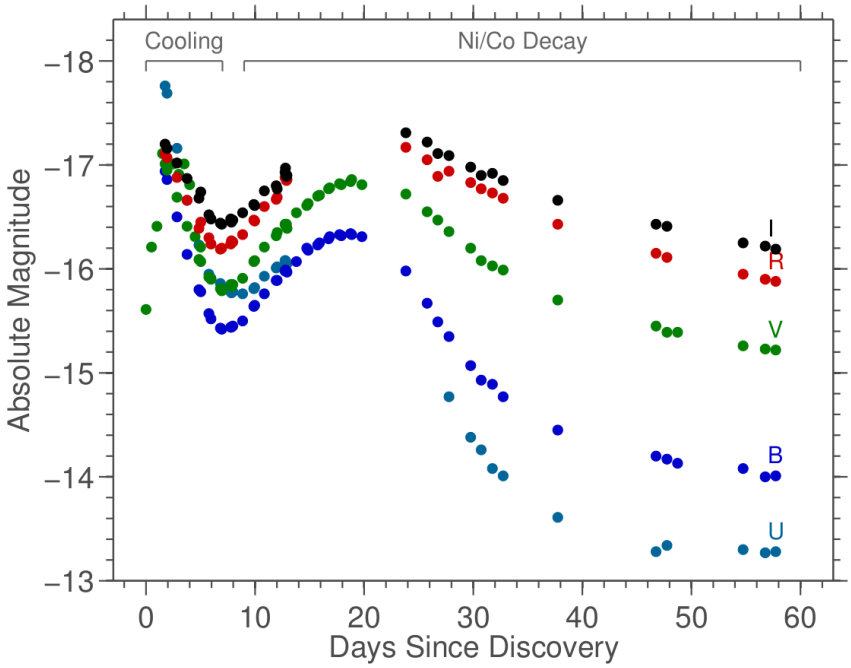

Figure 12. Multi-band light curves of Type IIb SN 1993J (Richmond et al., 1994). Two distinct maxima are evident. Adopted from Arcavi (2017)

2 Interaction with circumstellar matter

In some rare cases a SN is surrounded by a dense region of CSM. There are several scenarios for the formation of this kind of CSM, such as massive outbursts and strong stellar winds from the progenitor star prior to SN explosion. In order for the CSM interaction to outshine – or even block – the normal SN emission, the mass-loss rate of the progenitor must be at least $\dot{M} > 0.01$ $M_\odot$ yr^{-1} Smith (2016a). Galactic examples, such as luminous blue variables (LBVs) η Carinae (η Car, see Fig. 13) and P Cygni (P Cyg), have demonstrated that the most massive stars may produce dense and complex CSM structures during the late stages of their evolution (Humphreys & Davidson, 1994). Massive enough CSM will leave an imprint to the observable properties of these SNe. It should be emphasised that interacting SNe are not an intrinsic class of SNe but are affected by *external* CSM[5].

Type IIn SNe are H-rich events showing narrow ($\sim 10^2 - 10^3$ km s^{-1}, Filippenko (1997)) Balmer emission lines in their spectra. Schlegel (1990) was the first to propose that these events are a separate subclass of SNe[6] while also speculating that CSM may be the cause for the line features. Chevalier (1990) showed that CSM interaction can indeed explain the narrow lines. In short, the kinetic energy of the SN ejecta is transformed into radiation by the CSM interaction.

Although the underlying idea of CSM interaction is fairly straightforward, modeling of the observable properties is not. As mentioned already, the CSM is usually asymmetric and heterogeneous. This leads to the fact that not only the CSM configuration (geometry, composition, density, opacity and so on) alters the observed properties but the viewing angle may have an effect as well. Selected models from the literature are briefly reviewed below. For a thorough theoretical review of various thermal and non-thermal emission processes related to CSM interaction, see Chevalier & Fransson (2016).

[5]In principle any other type of SN may produce a SN IIn (or Ibn) provided that the progenitor has, for any reason, a H- (or He-) rich CSM. Additionally, for instance and as explained below in Section 2.2, colliding H-rich shells of matter can produce a SN IIn-looking spectrum.

[6]Coining also the designation IIn (for "narrow").

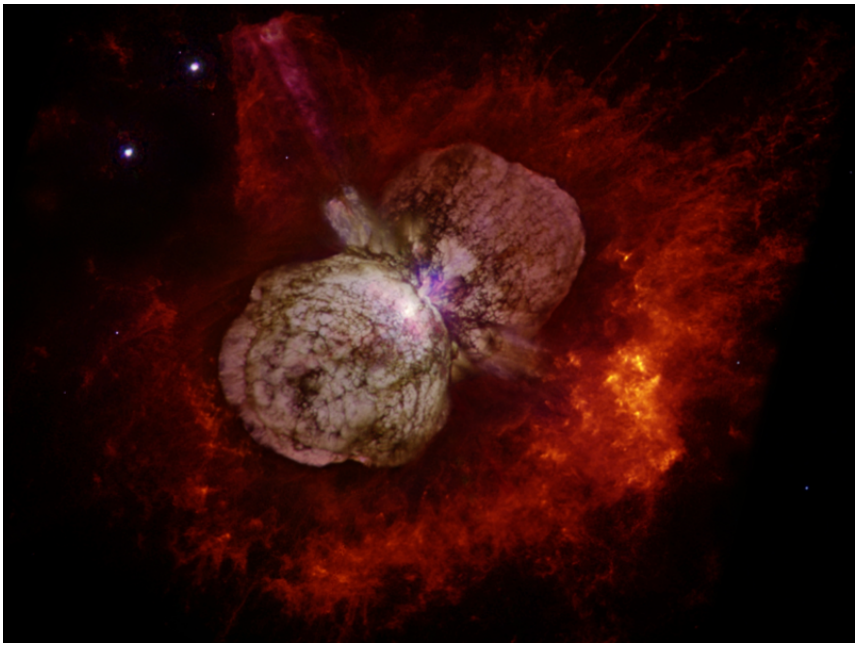

Figure 13. The bipolar lobes (The Homunculus nebula) of η Car. The eruption causing them was observed in the late 1830s as a rapid brightening lasting for almost two decades with relatively small fluctuation in brightness. Smith et al. (2003) estimated that at least 12 $M_\odot$ of matter was ejected at velocity of roughly 650 km s^{-1} during this period. The projected diameter across the lobes is roughly 0.2 pc ($16''$) whereas the central star is somewhere within the innermost 0.01 pc ($< 1''$). Also noticeable are the radially elongated structures on a disk-like plane between the lobes. Additional diffuse material surrounding these aforementioned structures makes the CSM geometry extremely non-spherical. This is a problem not only for the modelers of the CSM interacting SNe but also for the theory of stellar evolution of massive stars. See e.g. a review by Humphreys & Davidson (1994). Image: NASA/Nathan Smith

2.1 Spherically symmetric standard model

As usual, it is easier to begin with a spherically symmetric case even though the reality is probably different. Fig. 14 shows a basic scheme of the ejecta-CSM interaction model. The following description is from a review by Smith (2016a).

In this simplified picture the photosphere moves through the zones from 1 to 4 as time passes. This also changes the line profiles[7]. At early times, assuming that the unshocked CSM (1) is dense enough and ionised by the radiation produced by the forward shock (FS), the photosphere is located in the CSM due to electron scattering. At this stage a spectrum

[7]To emphasise: lines of H (IIn) or He (Ibn).

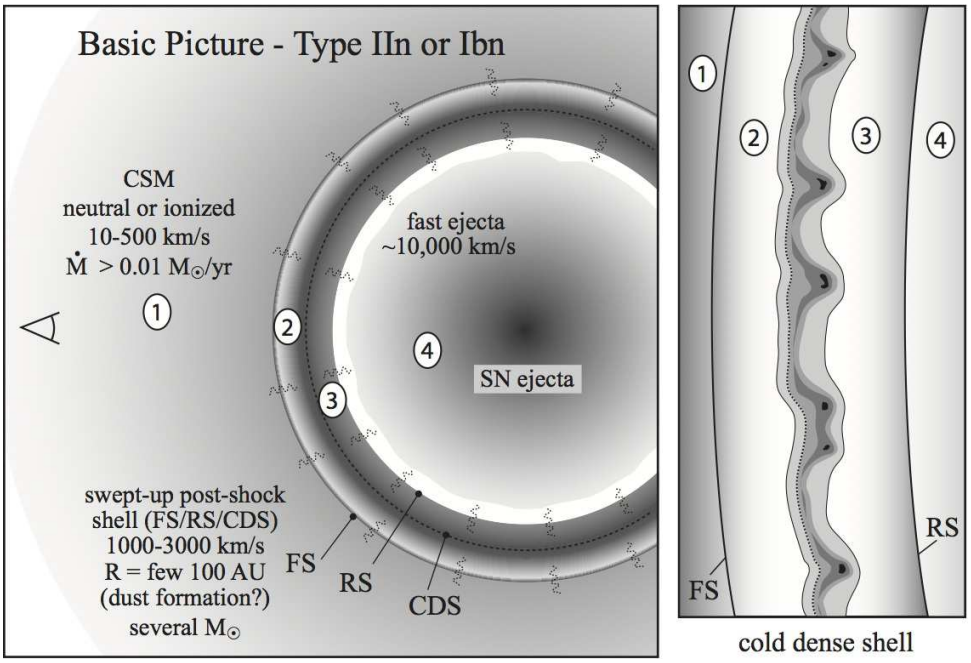

Figure 14. Basic spherically symmetric model for interacting SNe. Four different zones indicated are as follows. **(1)** Unshocked CSM produced by the progenitor (stellar wind and/or outbursts) recently prior to explosion. **(2)** Shocked CSM behind the forward shock (FS) propagating radially outwards. **(3)** Shocked SN ejecta behind the reverse shock (RS) propagating inwards. As a whole, the shock region propagates outwards. Note that this shock is not from the shock breakout (see Section 1.3.2), but a consequence of the ejecta-CSM interaction. **(4)** unshocked SN ejecta. **Left:** Squiggly lines indicate X-ray and UV photons generated by the shock which can propagate inwards to the ejecta or outwards to the unshocked CSM. **Right:** zoom-in to the shock region. Because of the forward and reverse shocks, a contact discontinuity is formed in the middle. A thin layer known as the CDS (Chevalier & Fransson, 1985) is formed as the radiative cooling is efficient within the discontinuity. As illustrated, Rayleigh-Taylor instabilities are typically mixing this region. Adopted from Smith (2016a).

shows a blue continuum and narrow emission lines with Lorentzian wings[8].

While the ejecta expands, the CSM density drops (assuming CSM was produced by a steady wind, for instance) and, eventually, the photosphere recedes into the shock region (2-3). At this point broader line profiles appear and, in certain cases, they can also show P Cygni absorption features. This radiation is produced in the efficiently cooling cool dense

[8]These are usually called as electron scattering wings due to the fact that they are produced by partial up and down scatter of line photons by free electrons (Chugai, 2001). See Dessart et al. (2009) for theoretical consideration.

shell (CDS) which is continuously reheated by the radiation from the shock fronts (forward and reverse).

Eventually, the photosphere recedes into the unshocked ejecta (4). At this point normal SN features (P Cygni profiles in H lines for Type II SNe, for instance) would be observable if the CSM interaction is weak or has stopped altogether. If strong CSM interaction continues, however, these normal features are never seen and narrow emission lines are persistent in the spectra. In some intermediate case the spectral properties might be altered by the heating of the ejecta by the emission from the RS before the interaction stops. It is also possible to have a CSM configuration in which the CDS becomes optically thin in the line of sight but the limb-brightening at the edges results to optically thick CDS "ring" around the ejecta. In this case the spectra would show some form of blend of normal SN features superimposed by the narrow emission lines in different characteristic velocities.

As explained above, even with the spherically symmetric case it might be difficult to make conclusions based on the spectral evolution. In case of asymmetric CSM the spectral evolution is even harder to deduce. In this case, the emission might be originating from any of the aforementioned zones simultaneously, which potentially produces multi-component spectral properties and a "bumpy" light curve evolution.

2.2 Numerical simulations

Before moving to the results from recent numerical simulations of CSM interaction, the observed properties of a couple of well-sampled Type IIn SNe are briefly reviewed. SNe 1994W (e.g. Sollerman et al. (1998); Chugai et al. (2004)) and 1998S (e.g. Fassia et al. (2000, 2001); Leonard et al. (2000); Liu et al. (2000); Chugai (2001)) were among the first well-sampled cases of bright transients showing narrow emission lines.

SN 1994W was discovered on 29 July 1994. The light curve shows a rise time of roughly a month to the maximum light, followed by a steady decline for three months and a quick drop and a faster decline after that. Spectra exhibit narrow Balmer emission lines

with narrow P Cygni absorption components. Emission lines of various metals strengthen towards the later epochs. Spectra are shown later in Fig. 16.

SN 1998S was discovered on 3 March 1998. Although the explosion date is not well constrained, the light curve shows a rapid rise in 2-3 weeks to the maximum light. After this, the brightness declines fairly constantly for several months. The decline seems to slow down a bit two months after the maximum light. Spectroscopic evolution is completely different compared to SN 1994W. Only the very early spectrum exhibits narrow emission lines. The lines fade within two weeks leaving relatively featureless and blue continuum. A couple of months later, a broad Hα and Ca II near-infrared (near-IR) triplet (8498,8542,8662 Å) lines appear. Spectra are shown later in Fig. 15.

It is noteworthy that, although Type IIn SNe are heterogeneous in their observed properties, similar SNe have been observed. For instance, observations of SNe 2009kn (Kankare et al., 2012) and 2013fc (Kangas et al., 2016) show comparable evolution to SNe 1994W and 1998S, respectively.

Due to the complexity in the treatment of hydrodynamics and radiative transfer, the state-of-the-art simulations still assume spherical symmetries. Even so, a variety of different spectral and photometric outcomes can be achieved by varying the physical properties of the ejecta and/or the CSM. Such simulations were run, for instance, by Dessart et al. (2016) (D16 in this Section) and the main results are reviewed below.

In their simulation, D16 collide two shells of material. In case of SNe IIn, the inner shell would be the SN ejecta and the outer shell dense CSM. However, this model is – in principle – valid also for non-terminal explosions, such as colliding shells from LBV-like outbursts as discussed further in Section 3. Summary of different model parameters is given in Table I.

In model A they attempt to reproduce the observed properties of the Type IIn SN 1994W in a similar fashion as previously modelled by Chugai et al. (2004): a SN explosion surrounded by an extended CSM shell. The main difference is the type of the CSM. Chugai

Table I. Different configurations and parameters for inner and outer shells. Numbers in the parentheses indicate the powers of ten. Adopted from D16

	Inner shell						Outer shell					
Model	Type	Age (d)	$E_{\rm kin}$ (erg)	$M_{\rm tot}$ ($M_\odot$)	$V_{\rm m}$ (km/s)	$R_{\rm t}$ (10^{15} cm)	Type	Age (d)	$E_{\rm kin}$ (erg)	$M_{\rm tot}$ ($M_\odot$)	$\dot{M}$ ($M_\odot$/yr)	$V_{\rm m}$ (km/s)
A	E	12.0	1.00(51)	9.96	3000	1.00	W	1157.4	3.49(46)	0.35	0.1	100
B1	E	11.5	4.95(49)	0.98	2189	0.85	W	167.2	3.56(48)	1.0	1.0	600
B2	E	22.9	9.57(49)	9.20	970	1.29	W	253.3	3.56(47)	0.1	0.1	600
B3	E	6.9	9.56(50)	9.50	3042	1.18	W	233.4	3.56(47)	0.1	0.1	600
R1	E	36.2	4.70(49)	1.0	2150	1.00	W	1971.1	3.39(46)	1.0	1.0	60
R2	E	55.1	8.90(49)	9.54	937	0.97	W	1889.0	3.42(45)	0.1	0.1	60
R3	E	22.2	9.28(50)	9.54	3027	1.33	W	2598.8	3.42(45)	0.1	0.1	60
C	E	2.3	8.56(49)	0.31	4755	0.20	E	127.9	1.19(49)	6.3	...	396
D	E	23.4	6.77(49)	0.29	4730	1.80	E	941.7	0.94(49)	6.1	...	377

Model label as explained in the text.

Type: either a massive ejecta (E) or steady wind (W).

Age: time since shell ejection or start of the wind at the onset of interaction

$\mathbf{R_t}$: initial radius of interaction

$\dot{\mathbf{M}}$: mass-loss rate for outer shells produced by a steady wind.

$\mathbf{E_{kin}}$: kinetic energy, $\mathbf{M_{tot}}$: total mass, $\mathbf{V_m}$: mean mass-weighted velocity

et al. (2004) concluded that a shell of 0.4 $M_\odot$ was most likely ejected by an explosive outburst 1.5 years prior to SN explosion.

D16, on the other hand, assume that the CSM shell was produced by a strong and steady wind with a mass-loss rate of $\dot{M} = 0.1$ $M_\odot$ yr^{-1}. In order to obtain similar CSM mass and initial radius ($R_t \sim 10^{15}$ cm) at the start of interaction, they assume that the wind ($V_m = 100$ km s^{-1}) lasted for 3.5 years and abated 3 years prior to explosion. They then explode a 10 $M_\odot$ ejecta expanding at $V_m = 3000$ km s^{-1} with the canonical energy of $E_{kin} = 10^{51}$ erg. After 12 days the ejecta reaches the CSM shell. This model is, in principle, the same as the spherically symmetric model explained in the previous Section.

Spectral evolution of model A is shown in Fig. 15. This model fails to reproduce the evolution of SN 1994W (spectra shown in Fig. 16). SN 1994W shows narrow lines throughout its evolution indicating continuous CSM interaction. Model A, however, de-

velops broad Hα and pronounced Ca II near-IR triplet lines later on. These features typical for normal Type II SNe indicate that the expanding CDS in the interaction region has become optically thin and the dominant contribution to the luminosity is coming from the inner SN ejecta. This is also evident in the bolometric light curve shown in Fig. 17.

Interestingly, as shown in Fig. 15, the main features of the spectral evolution do resemble that of the Type IIn SN 1998S instead. Although SNe 1994W and 1998S show completely different spectral evolution, they do have similar light curves. Modeled V-band light curve (see Fig. 7 in D16) matches their evolution further strengthening this model as an interpretation for SN 1998S.

In an attempt to reproduce the spectral evolution of SN 1994W, D16 also explode a low-mass ejecta colliding with a massive CSM shell previously ejected by a massive outburst instead of a steady wind lasting for years. In model C an inner shell of $M \approx 0.3$ M$_\odot$ and $E_{kin} \approx 9 \cdot 10^{49}$ erg expanding at $V_m \approx 4760$ km s^{-1} rams against an outer shell of $M \approx 6$ M$_\odot$ expanding at $V_m \approx 400$ km s^{-1}. The initial radius is set at $R_t = 2 \cdot 10^{14}$ cm which means that the shells collide already 2.3 days after the explosion.

As shown in Fig. 16 the spectral evolution is quite different and fits the observations of SN 1994W better. Narrow Balmer emission lines showing narrow P Cygni absorption components are visible throughout the simulation time. This is due to the completely different model configuration. In model A the photosphere is, at first, located in the ionised outer shell. As time passes, the expanding CDS overtakes this photosphere effectively changing the location of the photosphere to the CDS. Eventually, both the CDS and the outer shell become optically sufficiently thin so that the underlying Type II SN features begin to dominate the spectra. As expected, the electron scattering wings of Hα profile vanish simultaneously.

In model C, however, the CSM shell never becomes optically thin (in the timescales in question, at least) and dominates the spectral evolution. Additionally, due to the fact that a less-massive but faster-moving ejecta rams into the outer shell, the interaction is initially

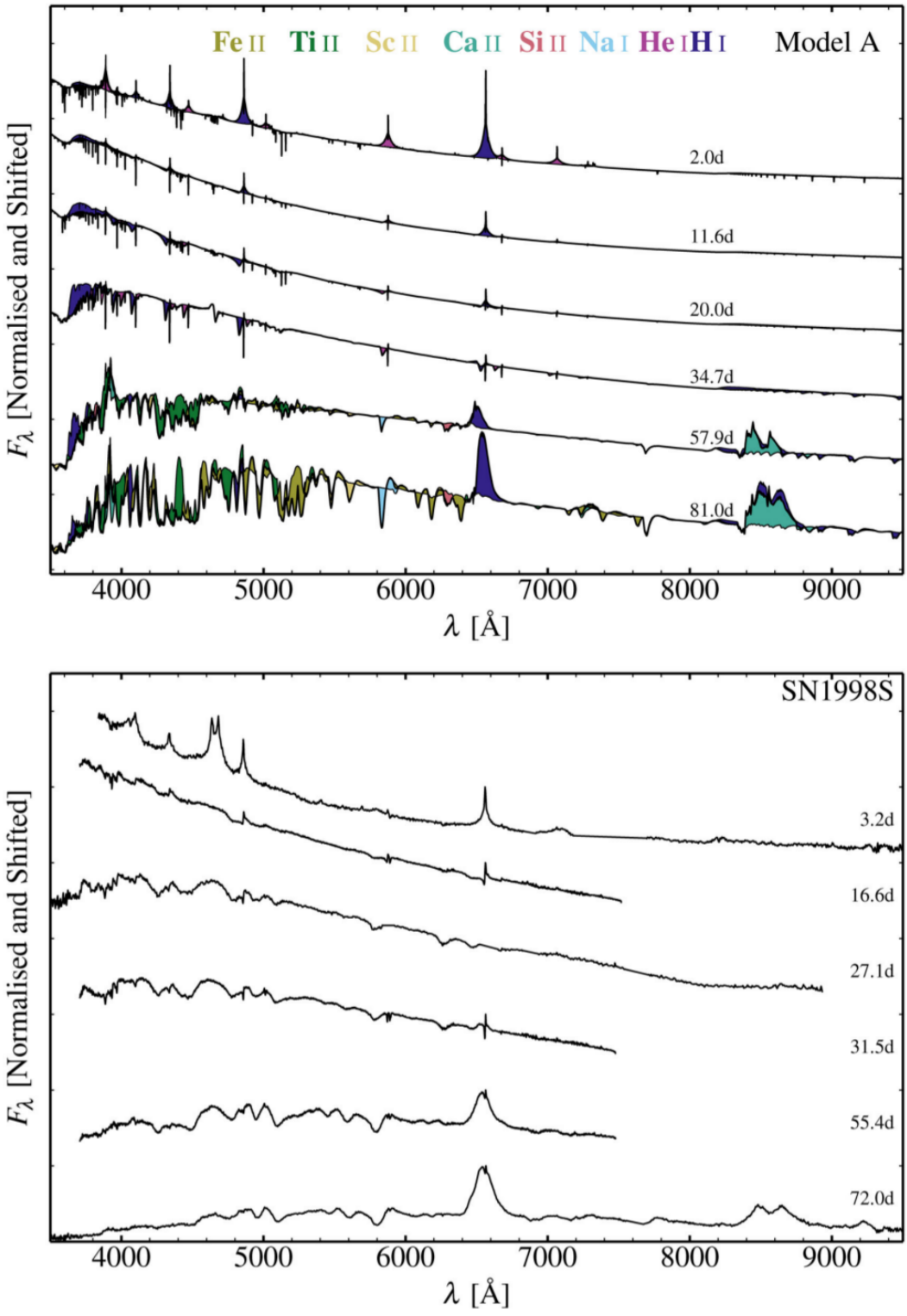

Figure 15. Model A spectral evolution compared to SN 1998S (Fassia et al., 2001; Leonard et al., 2000) at similar epochs. Adopted from Dessart et al. (2016)

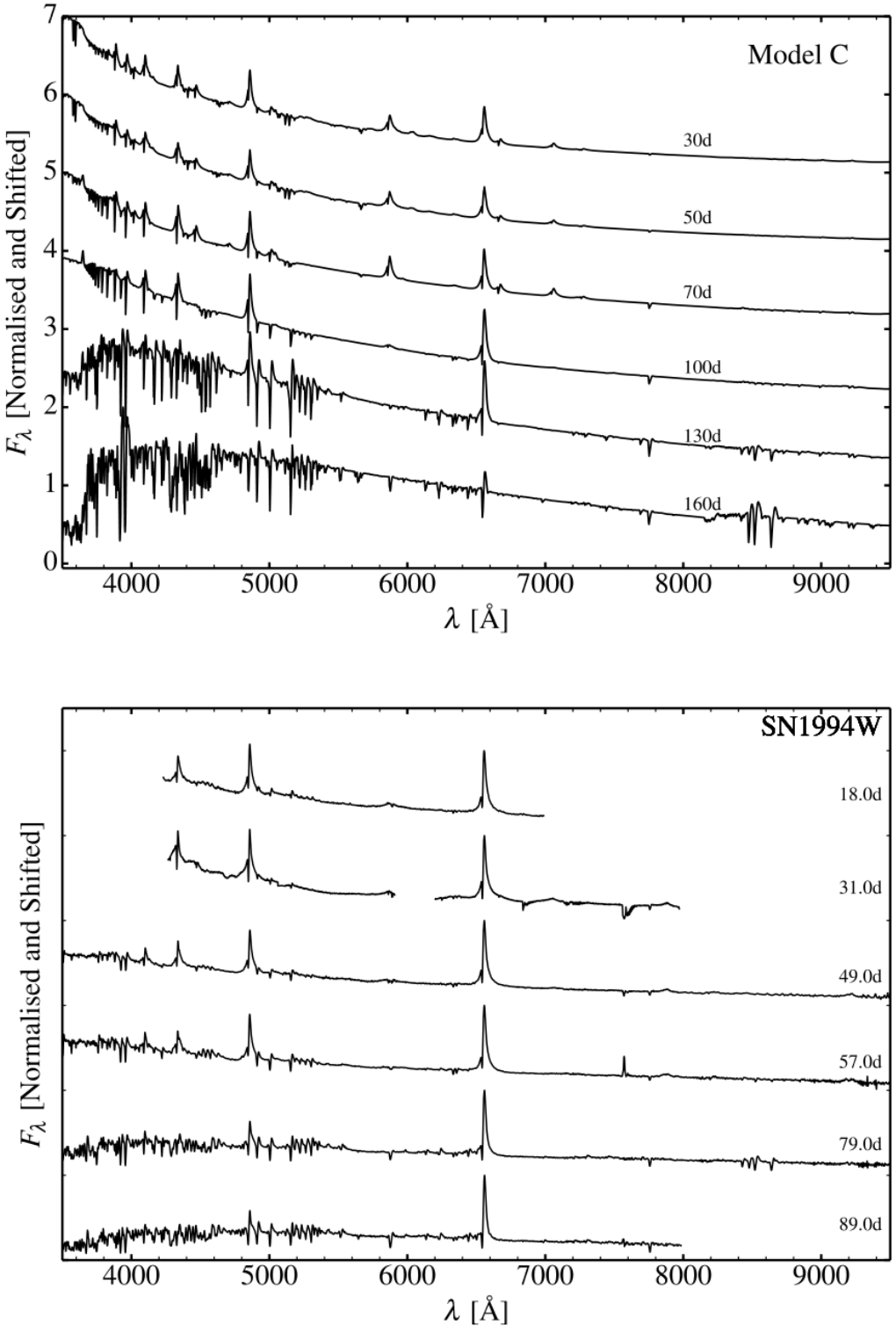

Figure 16. Model C spectral evolution compared to SN 1994W (Chugai et al., 2004; Sollerman et al., 1998) at similar epochs. Adopted from Dessart et al. (2016)

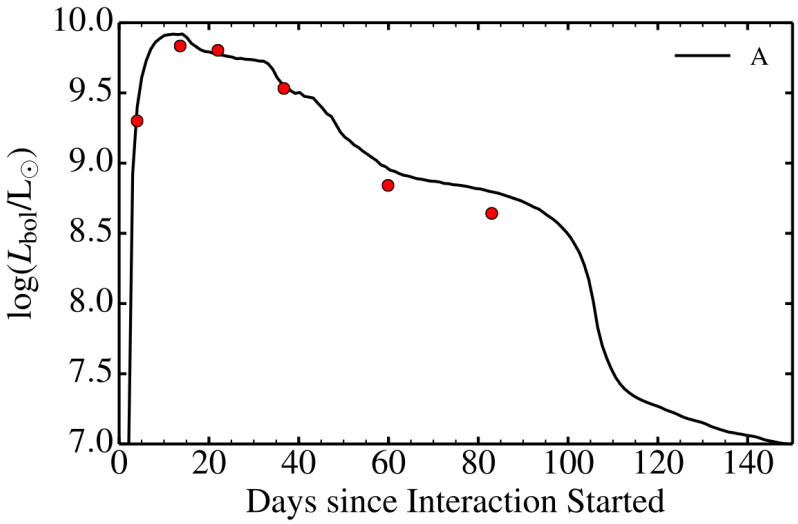

Figure 17. Bolometric light curve of model A (solid line) compared to luminosities calculated independently from the synthetic spectra (dots). Evolution approximately 60 days after the onset of interaction is similar to a normal SN II. This is also clearly evident in the spectra (Fig. 15). Adopted from D16

extremely strong compared to model A. This means that the inner shell – while quickly decelerating – heats the inner parts of the outer shell up producing an optically thick hot shell. Within 10 days this shock is quenched and the kinetic energy of the inner shell is mostly reprocessed into radiation which is trapped within the optically thick outer shell. Inner heating effectively pushes the photosphere further out as the radiation ionises the outer shell from within.

The aforementioned evolution is evident in the Hα line evolution. At first, the profile is dominated by the electron scattering wings that vanish as time passes. The P Cygni absorption, on the other hand, deepens while the profile as a whole starts to look similar to normal Type II SN. The main difference, due to the lower expansion velocity compared to a SN, is the narrower profile than in a genuine Type II SN. Even though the underlying SN explosion was sub-energetic, the peak magnitude (as shown in Fig. 16 in D16), however, is comparable with a normal SN explosion. This is caused by the reprocessing of the kinetic energy of the inner ejecta.

Although model C reproduces the spectral evolution of SN 1994W, it fails when comparing to the observed light curve (Fig. 16 in D16): the model predicts longer plateau and

less luminous peak than observed. Model D explains this discrepancy with a different interaction radius of $R_t = 1.8 \cdot 10^{15}$ cm. This means that both shells are cooler and less dense when the interaction begins. This happens approximately 3 weeks after the explosion and has important consequences.

First of all, the shock is not quenched within the simulation time. This means that shock heating is a continuous power source in this case. Additionally, the CDS is effectively blocking the emission from the inner ejecta so that no normal SN features are seen. Electron scattering wings persist throughout the evolution as the ionised volume of the outer shell stays large. Secondly, due to lower optical depths, the light curve rise is faster reaching a brighter peak magnitude and a shorter plateau afterwards as observed in SN 1994W (Fig. 16 in D16). The spectral evolution is reproduced also with this model (Fig. 20 in D16).

In addition to aforementioned models, D16 also further investigate models similar to model A in a grid of various parameter values. There are two types of progenitors that produce a wind-type outer shell: blue supergiants (BSGs) (models B1, B2 and B3, see Table I) with a steady wind of $V_m = 600$ km s^{-1} and red supergiants (RSGs) (models R1, R2 and R3) with a steady wind of $V_m = 60$ km s^{-1}. Then, the evolution is modeled with various mass loss rates as well as different masses and energies of the inner shell. In D16, selected epochs of spectral evolution are shown in Fig. 9 and evolutionary implications of these models discussed in Section 6.

3 Intermediate luminosity optical transients

Three types of ILOTs are considered below: SN impostors, intermediate luminosity red transients (ILRTs) and luminous red novae (LRNe)[9]. All have similarities in their observed properties, such as the peak brightness in between classical novae and SNe. There are, however, certain differences. Below, an introduction is given and a well-studied example is presented for each subclass of ILOTs.

3.1 Supernova impostors

Van Dyk et al. (2000) suggested that not all of Type IIn SNe-like transients are necessarily caused by a terminal explosion of a star. Their follow-up campaign of nearby SN 1997bs, originally classified as Type IIn SN, revealed that its brightness, peaking at $M_V \approx -13.8$ mag, never reached values even close to typical SNe. Light curve comparison shown in Fig. 18 clearly shows that SN 1997bs is similar to known LBV-outbursts.

Furthermore, by comparing the late-time plateau magnitude to a magnitude of a possible progenitor star obtained from a pre-explosion image of the site, Van Dyk et al. (2000) suggested that the star could have survived the event. In conclusion, they proposed that SN 1997bs was not a genuine SN explosion but a massive outburst similar to the one experienced by η Car (Fig. 13).

Since SN 1997bs, several new transients have been discovered that showed similar observed features: SN IIn-like spectra accompanied by low peak luminosity and variable light curves. In certain cases it has also been possible to estimate the brightness evolution prior to the outburst using archival images. In these cases the light curves typically show variations indicating progenitor instabilities prior to the outburst.

[9]There seems to be certain discrepancies in the literature about the classification scheme. In some cases ILOTs and ILRTs are dubbed as one subclass, whereas in other cases an ILOT is a general description further divided into subclasses. Latter is used in this thesis. Another term suggested for these events is a "gap transient" (Kasliwal , 2012; Pastorello & Fraser , 2019a).

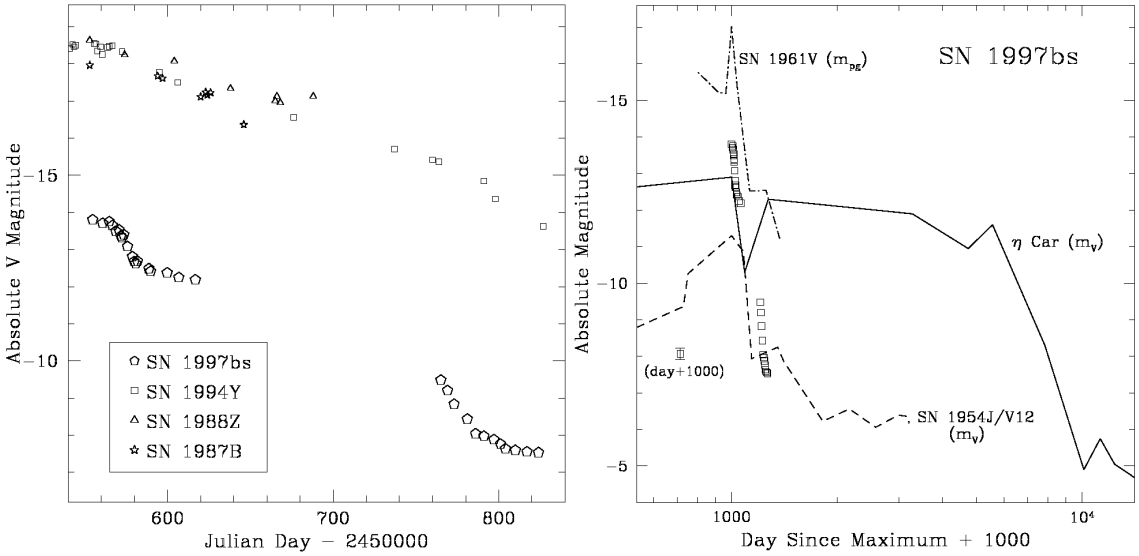

Figure 18. **Left:** comparison of V-band light curve of SN 1997bs to three Type IIn SNe: SN 1994Y (Ho et al., 2001), SN 1998Z (Turatto et al., 1993) and SN 1987B (Schlegel et al., 1996). Although spectroscopically similar to the others, SN 1997bs is clearly fainter at peak brightness. **Right:** comparison to known LBV-like eruptions: η Car and, originally classified as SNe, SN 1954J and SN 1961V (Humphreys et al., 1999). SN 1954J is also known as a variable star V12 in NGC 2403. SN 1997bs exhibits a similar peak magnitude and subsequent brightness drop as the others. Noteworthy is the long plateau of η Car before the drop. Adopted from Van Dyk et al. (2000)

Example spectra of impostors and ILRTs are shown in Fig. 19. In all cases the early spectra are dominated by narrow lines. Fig. 20 shows the location of impostors in a peak magnitude–fading time diagram and a peak magnitude comparison to Type II SNe. Many impostors have similar fading time scales as SNe but are typically fainter at maximum light. Due to their pre-explosion photometric variability and spectral features, LBVs are promising candidates as SN impostor progenitors.

Originally categorised as massive non-Wolf-Rayet stars by Conti (1984), LBVs are characterised by their photometric variability in variety of timescales and magnitudes. In quiescence, LBVs look like hot O/B -type ($\sim$ 12000−30000 K) supergiants with prominent H and He I emission. For many, Fe II and [Fe II] emission lines are strongest at this stage. At optical maximum LBVs evolve towards spectral classes A or F with lower temperatures ($\sim$ 7000 − 8000 K) and weaker Fe lines. LBV stage is a part of post-main sequence evolution of a supergiant star. (Humphreys & Davidson, 1994)

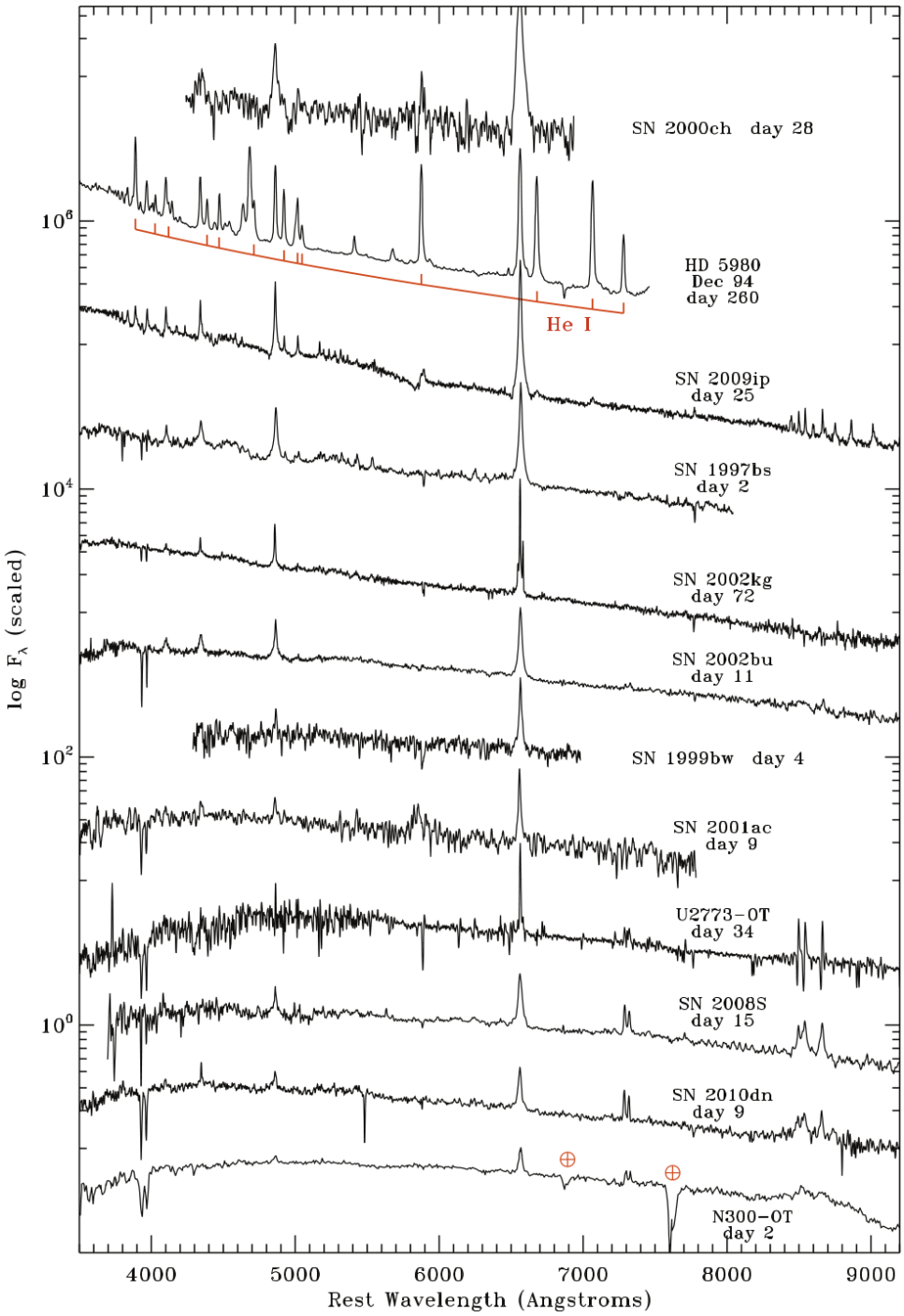

Figure 19. Early spectra of selected ILOTs. Many were published by Smith et al. (2011) except SN 2008S (Smith et al., 2009), U2773-OT and SN 2009ip (Smith et al., 2010), N300OT (Bond et al., 2009), SN 2002kg (Van Dyk et al., 2006) and SN 1997bs (Van Dyk et al., 2000). A spectrum of HD 5980 (Koenigsberger et al., 1998) few months after its giant LBV outburst in 1994 is shown for comparison. At this time several prominent lines of He are observed. Adopted from Smith et al. (2011)

Several types of variability have been observed in LBVs. Small oscillations of < 0.5 mag in time scales of months to years are common. Eruptions of $1-2$ mag in the optical are typical. Bolometric luminosity, however, remains constant meaning that the brightening is caused by a change in the bolometric correction. In other words, an LBV in this stage does not brighten but the peak emission shifts from the UV to the optical wavelengths. Quiescent and eruptive stages typically last for years while the brightening after the onset of an eruption takes place in timescales of months. Giant eruptions of ≥ 2 mag are rarer. In this stage an LBV increases also its bolometric luminosity. After this brief stage, the luminosity typically declines rapidly and an LBV remains in quiescence for a longer time. (Humphreys & Davidson, 1994)

This drastic change in the appearance of an LBV during an outburst is believed to be caused by the change in the location of the photosphere. During quiescence, the photosphere more or less defines the surface of a star similar to main sequence stars. While in outburst, the mass-loss rate significantly increases and a pseudo-photosphere forms in the opaque CSM. This outward moving matter blocks the "real" photosphere while cooling. This changes the *appearance* of an LBV towards cooler spectral classes. Eventually this matter becomes transparent and an LBV resumes to its quiescent stage. (Humphreys & Davidson, 1994)

Exact processes leading to a variety of different outbursts (in brightness and duration) are poorly known. The luminosities of LBVs in quiescence are typically close to the classical Eddington limit[10], L_{Edd}, which is likely to cause instabilities. This alone could explain the small-scale variations. During an outburst the luminosity greatly exceeds L_{Edd} which could mean that the outflow of matter is driven by the increased mass-loss rate caused by a super-Eddigton wind (Smith et al., 2011). In this case the mass-loss would be triggered by a process close to the surface of the star. (Humphreys & Davidson, 1994)

Smith (2008), however, discovered a blast wave propagating outwards in the outer

[10]Limit in which the outwards pushing radiation pressure is equal to the binding self-gravity.

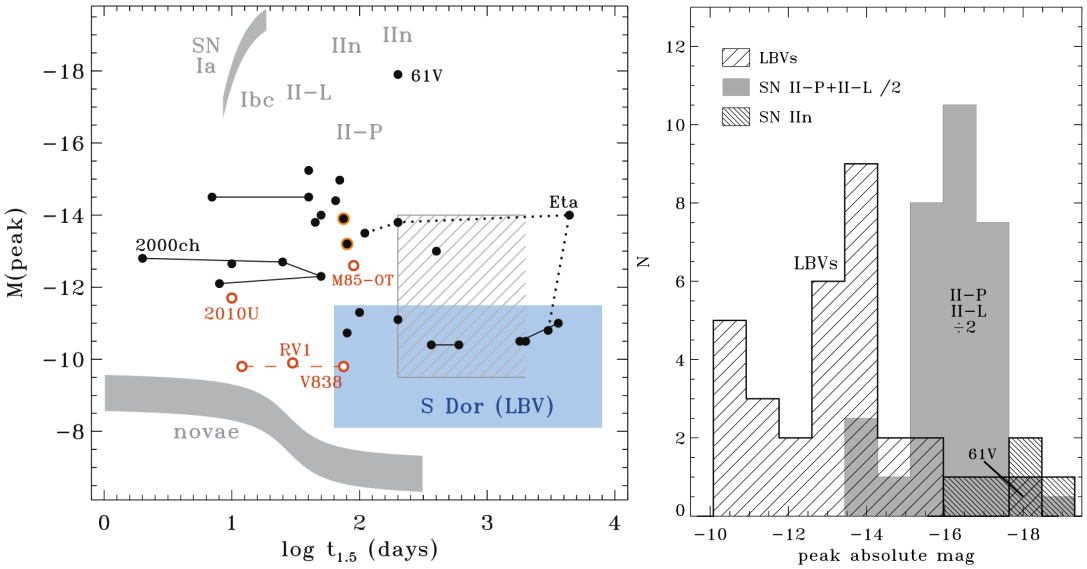

Figure 20. **Left:** a collection of SN impostors (see Table 9 in Smith et al. (2011)) shown as black points. In x-axis, $t_{1.5}$ is a characteristic time scale, in days, in which the transient fades by 1.5 magnitudes after the peak. Impostors with multiple (observed) outbursts are connected with solid or dashed lines. Possible ILRTs and LRNe, including two debated cases, are shown in red. Blue box shows the typical parameter space of S Dor-type LBV outbursts, whereas the dashed box shows the space of giant eruptions of LBVs. Rough locations of novae and SNe are shown in comparison. Note that, due to selection effects, the left-hand side of the impostor distribution is most likely undersampled. **Right:** a histogram of peak magnitudes of giant LBV-like eruptions compared to H-rich SNe from the KAIT sample (Li et al., 2011a). There is some overlap in between the brightest outbursts and faintest SNe. Adopted from Smith et al. (2011).

ejecta of η Car. N-rich material moving at velocities $3500 - 6000$ km s^{-1}, depending on assumed orientation, was inferred from the optical spectra. Slower N-rich "knots" moving approximately 300 km s^{-1} were also observed. This material was most likely ejected by an outburst about 1000 years earlier and partially further accelerated by a shock wave launched in the 1843 eruption. A shock front propagating in CSM gives rise to X-rays (Chevalier & Fransson, 2016) which are indeed observed in η Car (Seward et al., 2001) further strengthening the shock origin interpretation for this fast-moving material. This would imply that some *inner* explosion mechanism, rather than a wind-type mass loss, would be causing these outbursts.

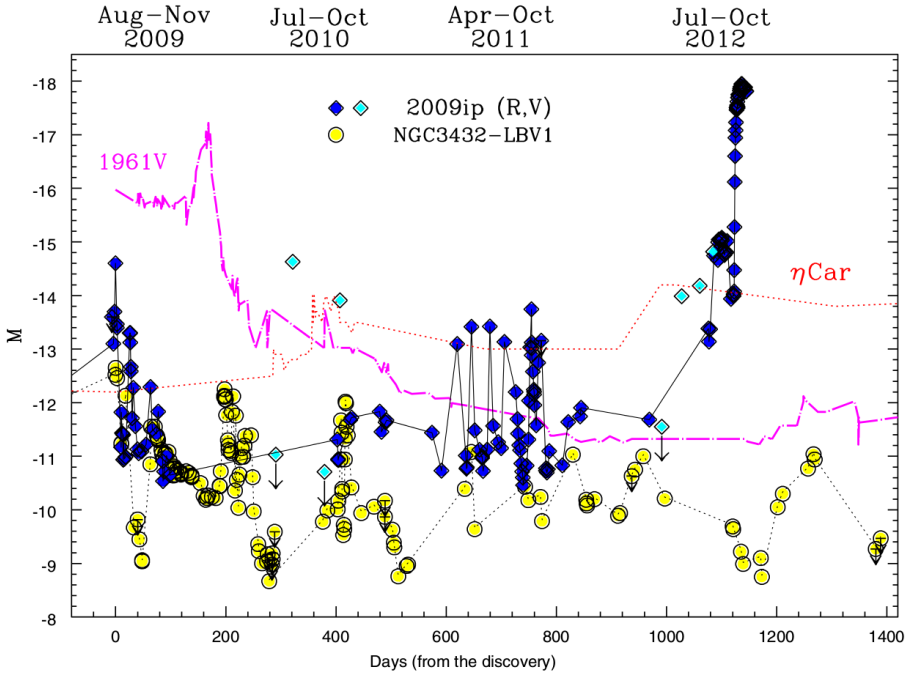

Figure 21. *R*-band light curve of SN 2009ip compared to historical transients η Car and 1961V as well as to a known impostor in NGC3432 (Pastorello et al., 2010). During the time in between 2009 and 2012, SN 2009ip shows remarkable variability. The 2012B brightening (October 2012) displays SN-like peak magnitude and light curve shape around maximum light. Adopted from Pastorello et al. (2013).

3.1.1 SN 2009ip

SN 2009ip (Fraser et al., 2013, 2015; Mauerhan et al., 2013; Margutti et al., 2014; Mauerhan et al., 2014; Ofek et al., 2013; Pastorello et al., 2013; Prieto et al., 2013; Smith et al., 2010, 2013, 2016b) is the best studied impostor to date. The progenitor experienced an LBV-type outburst in August 2009, peaking at $M_R = -14.5$ mag (Smith et al., 2010). During the next three years, SN 2009ip displayed further variability that ended in a double-peaked brightening in September (event A, peaking at $M_R \approx -15$ mag) and October (event B, peaking at $M_R \approx -18$ mag) 2012. Photometric evolution of SN 2009ip is shown in Fig. 21 (see also Fig. 32 in Section 6.2.2 and Fig. 36 in Section 6.2.4 for a better illustration of the difference of peaks A and B).

Additionally, Smith et al. (2010) used archival *Hubble Space Telescope* (*HST*) images to study the properties of the progenitor star. Photometric variability was observed during

several years prior to the 2009 outburst. The brightness of the progenitor in quiescence, $M_V \approx -9.8$ mag ($\log(L/\ \mathrm{L}_\odot) = 5.9$), indicates that the star was a supergiant star further strengthening an LBV interpretation.

Early spectroscopic evolution of SN 2009ip, observed by Fraser et al. (2013), is shown in Fig. 22. There is a clear difference in between events 2012A and 2012B. After the 2012A maximum, the spectra display broad H P Cygni profiles superimposed by narrow lines typical to CCSNe surrounded by CSM. Ca II near-IR triplet lines are also prominent. At the time of 2012B maximum, however, the spectra are dominated by narrow emission lines and a blue continuum indicative to CSM interaction. Ca lines are not present. Later on, broad features as well as [Ca II] doublet (7291,7324 Å) and near-IR triplet begin to emerge. Multi-velocity components in absorption are observed. Additionally, Hα emission line develops a broad component.

It is still debated (Fraser et al., 2013, 2015; Smith et al., 2014; Graham et al., 2017) whether or not the events in 2012 were produced by a genuine SN explosion followed by interaction with previously ejected CSM or, for instance, a collision of CSM produced by separate eruptions (see Section 2.2). Although the evidence points towards a SN explosion, this can be confirmed eventually only by observing the disappearance of the progenitor. Additionally, Soker & Kashi (2013) suggested that SN 2009ip was caused by a post-merger outburst of a binary star but this claim is based only on photometric modelling. Furthermore, as explained later in Section 3.3, binaries typically produce redder transients.

Since SN 2009ip, similar transients, such as SNe 2015bh (Elias-Rosa et al., 2016; Thöne et al., 2017; Boian & Groh, 2018, Section 6.2.2) and 2016bdu (Pastorello et al., 2018, Section 6.2.4) have been discovered.

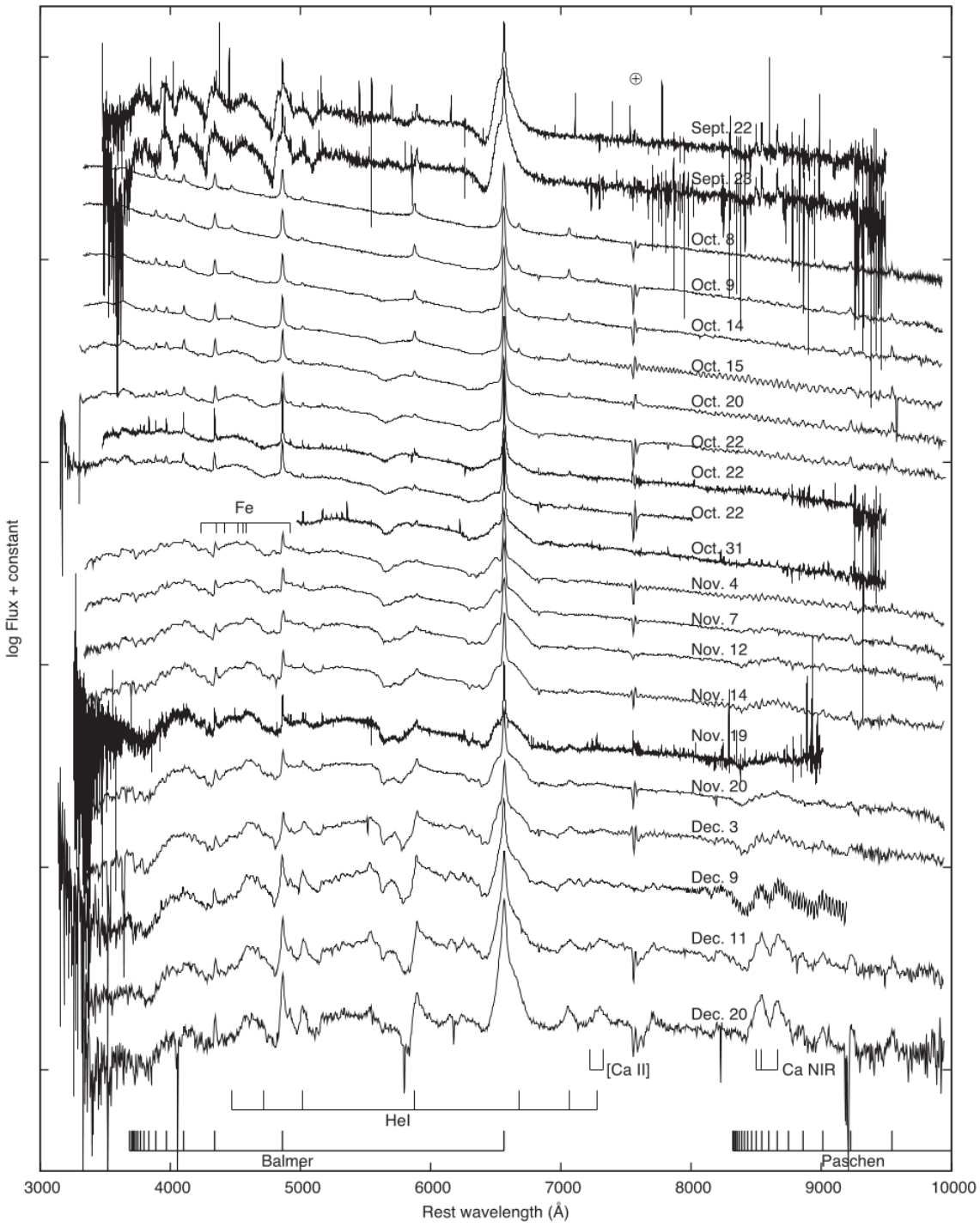

Figure 22. Spectroscopic evolution of SN 2009ip at early times. Spectra observed in September coincide with the end of eruption event 2012A. The next two were observed around the peak of event 2012B. Adopted from Fraser et al. (2013)

3.2 Intermediate luminosity red transients

Originally classified as a subclass of SN impostors, ILRTs are even more recently proposed class of transients[11]. They are also fainter than SNe and show narrow emission lines similar to impostors. There are, however, certain characteristic differences. Progenitors are typically super-asymptotic giant branch stars ($M_{\mathrm{ZAMS}} = 8 - 12\ \mathrm{M}_{\odot}$) surrounded by a cocoon of CSM expelled by the stars at the late stages of their evolution. As explained in Section 1.1.2, these low-mass stars potentially explode as faint EC- or CCSNe. Their maximum brightness and post-plateau decline rate can be affected by the CSM interaction. Fading of ILRTs at the radioactive tail phase can be slower than expected for the decay of ^{56}Co alone if the CSM interaction continues and increases the radiative output. Spectroscopically ILRTs are cooler and redder than impostors at early times. Additionally, the Ca doublet and triplet are already present at the early times and throughout the evolution. (Cai et al. (2018); Moriya et al. (2014) and references therein.)

3.2.1 SN 2008S

One of the most promising dust-enshrouded ECSN candidates is a nearby SN 2008S (e.g. Prieto et al. (2008); Botticella et al. (2009); Smith et al. (2009); Adams et al. (2016)). Even with the close proximity ($D_{\mathrm{L}} \approx 5.6$ Mpc), the progenitor was not detected in the optical wavelengths. Based on mid-IR *Spitzer* archival images, however, the progenitor was detected and estimated to be a $M \sim 10\ \mathrm{M}_{\odot}$ star obscured by a large amount of dust. Photospheric radius $R \approx 150$ au and temperature $T \approx 440$ K were inferred from a blackbody fit. This temperature is typical for thermally radiating dust. In addition to low-mass progenitor, no mid-IR variability was detected during a few years prior to the brightening further strengthening a non-LBV progenitor interpretation. (Prieto et al., 2008)

Photometric and spectroscopic comparison of SN 2008S to selected transients is shown

[11] Again, there are discrepancies in the literature. Some authors count ILRTs as impostors due to their observed similarity to LBV outbursts.

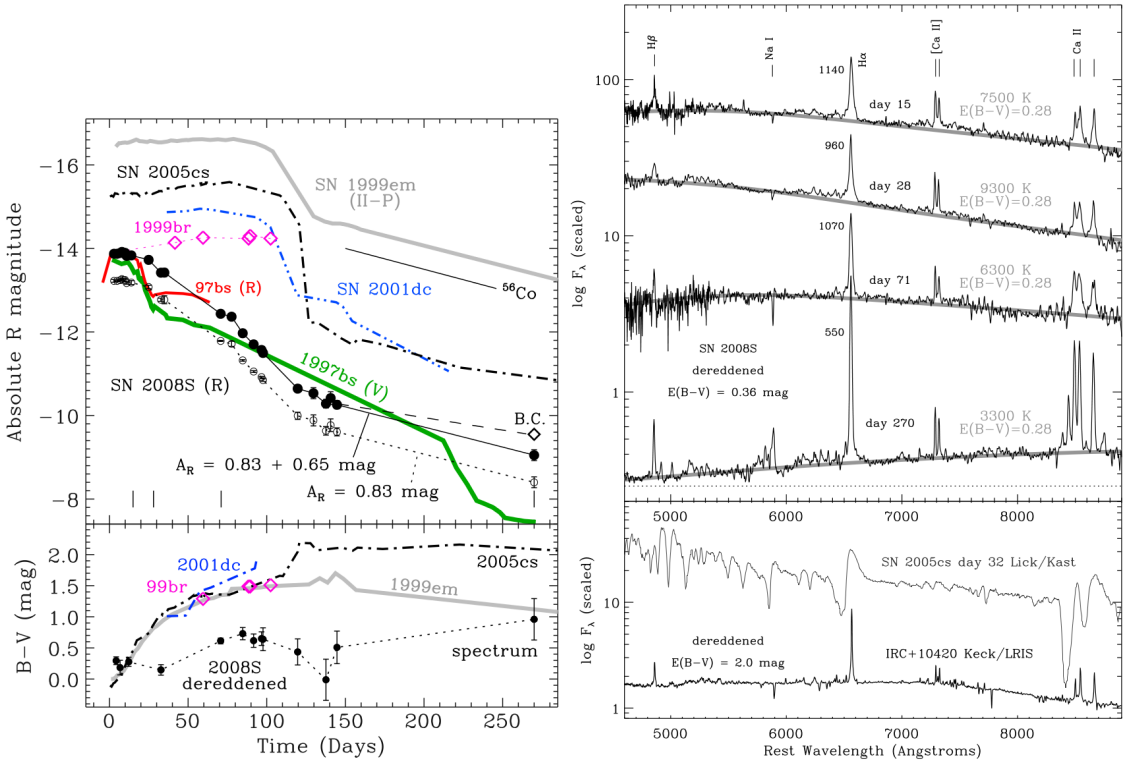

Figure 23. **Left:** *R*-band light curve and colour evolution comparison of SN 2008S to a normal Type IIP SN 1999em (Leonard et al., 2002), low-luminosity Type IIP SNe: SN 1999br, SN 2001dc, SN 2005cs (Pastorello et al., 2004, 2009) and impostor SN 1997bs (Van Dyk et al., 2000). Open circles have Galactic extinction only, filled circles have additional local extinction estimation added. **Right:** spectral evolution of SN 2008S. Spectra of low-luminosity Type IIP SN 2005cs and Galactic yellow hypergiant (YHG) IRC+10420 are shown for comparison. Due to the spectral similarity, it is, in principle, possible that the spectrum of SN 2008S could originate from an opaque and turbulent wind instead of an ejecta–CSM interaction. Adopted from Smith et al. (2009).

in Fig. 23 (see also Fig. 38 in Section 6.2.5). The *R*-band evolution is similar to SN impostors while even low-luminosity Type IIP SNe are still noticeably brighter. Spectra exhibit narrow emission lines of Hα, Hβ, Hδ, [Ca II] doublet, Ca II triplet, [O I] as well as Fe II and Mn II multiplets. Strong Na I D absorption line is indicative of considerable extinction in the line of sight caused by the dusty environment. (Botticella et al. (2009); Smith et al. (2009) and references therein.)

Recently, Adams et al. (2016) concluded that the mid-IR brightness of SN 2008S has faded below the progenitor level. This, in addition to optical and near-IR non-detections, points towards terminal explosion rather than impostor outburst. Newly formed dust could,

in principle, obscure the line of sight towards the transient but the amount required seems to be impractically large. They also argue, based on more recent modeling, that in case SN 2008S was a terminal explosion, it probably was a low-luminosity CCSN rather than ECSN. Nevertheless, future observations are still required to uncover the true fate of SN 2008S.

3.3 Luminous red novae

Similar to ILRTs, LRNe evolve with red colours and continua, but fade faster and have different spectral evolution. Typical spectral features are narrow emission line of Hα (other weak Balmer lines are possible) as well as atomic and molecular absorption lines that strengthen as the transient fades. Increasing absorption accompanied by late-time IR excess could indicate dust formation after the outburst. Unlike ILRTs, however, the progenitors of LRNe do not show IR excess meaning that they are not heavily dust-enshrouded at the time of the outburst. The progenitor systems of LRNe are usually binary stars. (Smith et al. (2016c) and references therein.)

3.3.1 V838 Monocerotis

The Galactic outburst of V838 Mon in 2002 produced a triple-peaked light curve caused by light echoes in previously lost stellar material. Spectroscopic evidence shows that the B3 V-type companion star was most likely engulfed within the outburst ejecta (Tylenda et al., 2011b). Additionally, CSM revealed by the light echoes suggests that the star had experienced prior mass loss as the CSM seems to have more or less spherically symmetric distribution around the progenitor. Large LBV-type variability is ruled out by the archival data. A light curve comparison is shown in Fig. 24, prominent spectral features[12] in Fig. 25 and the evolution of the light echo during the first months is shown in Fig. 26. (Munari et al., 2002; Bond et al., 2003; Munari et al., 2005)

[12] See also Fig. 35 in Section 6.2.3.

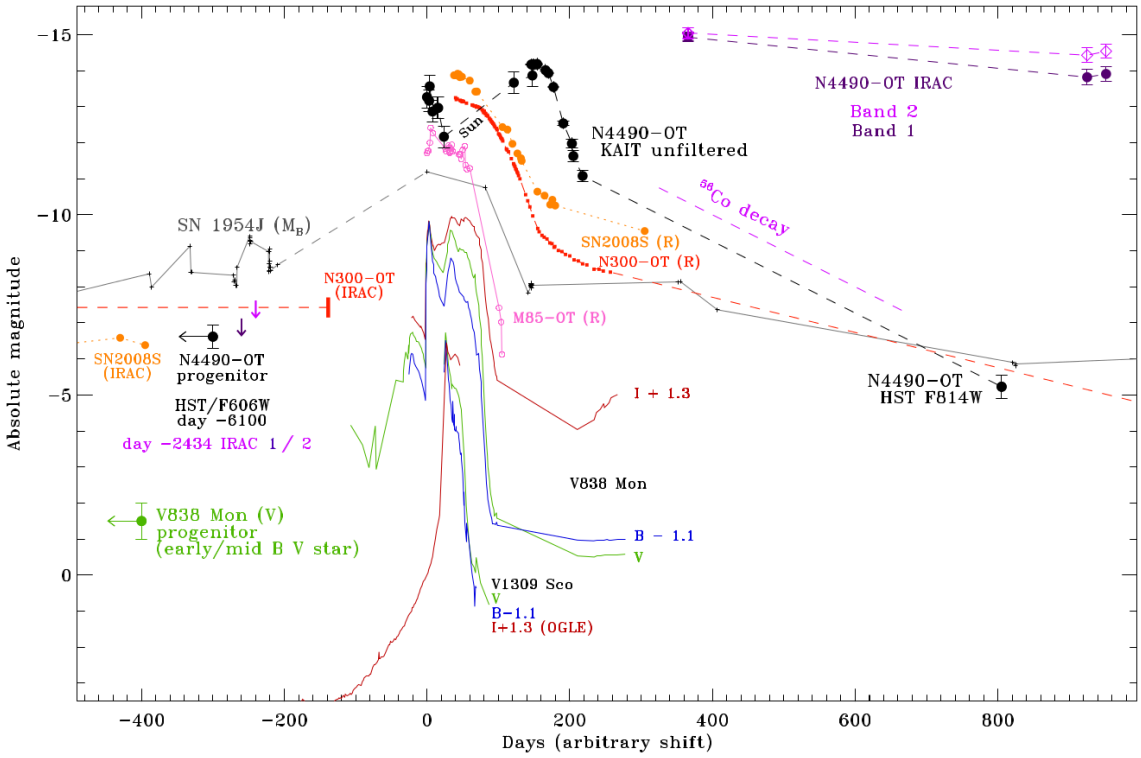

Figure 24. Comparison of LRNe V838 Mon (Bond et al., 2003; Sparks et al., 2008), V1309 Sco (Tylenda et al., 2011a, `www.aavso.org`) and NGC 4990-OT (Smith et al., 2016c); ILRTs SN 2008S (Prieto et al., 2008; Smith et al., 2009), NGC 300-OT (Prieto et al., 2008; Bond et al., 2009; Thompson et al., 2009) and M85-OT (Kulnari et al., 2007); an impostor SN 1954 J (Tammann & Sandage, 1968) and the probable progenitor of V838 Mon (Afşar & Bond, 2007; Rosero-Rueda et al., 2008). Adopted from Smith et al. (2016c).

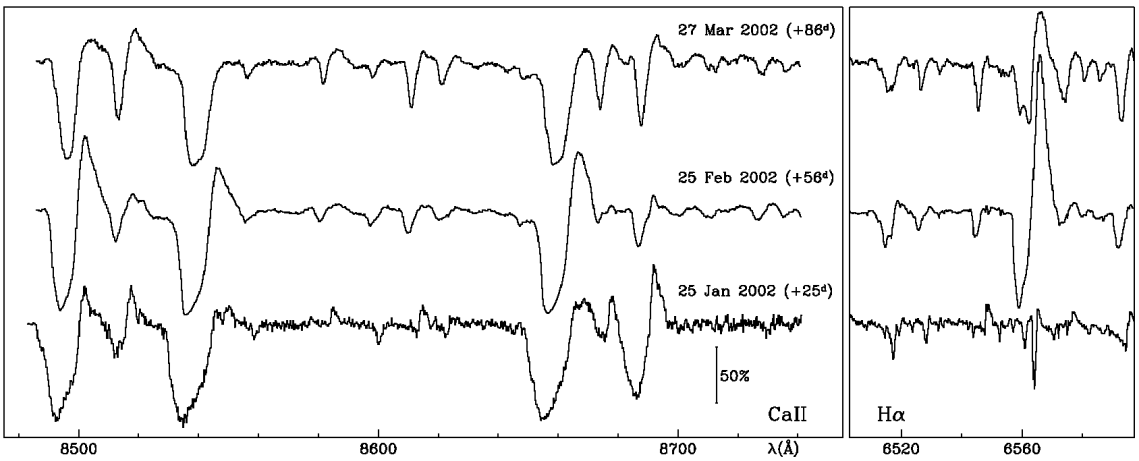

Figure 25. Early spectral evolution around [Ca II] triplet (left) and Hα (right) of V838 Mon. Adopted from Munari et al. (2002).

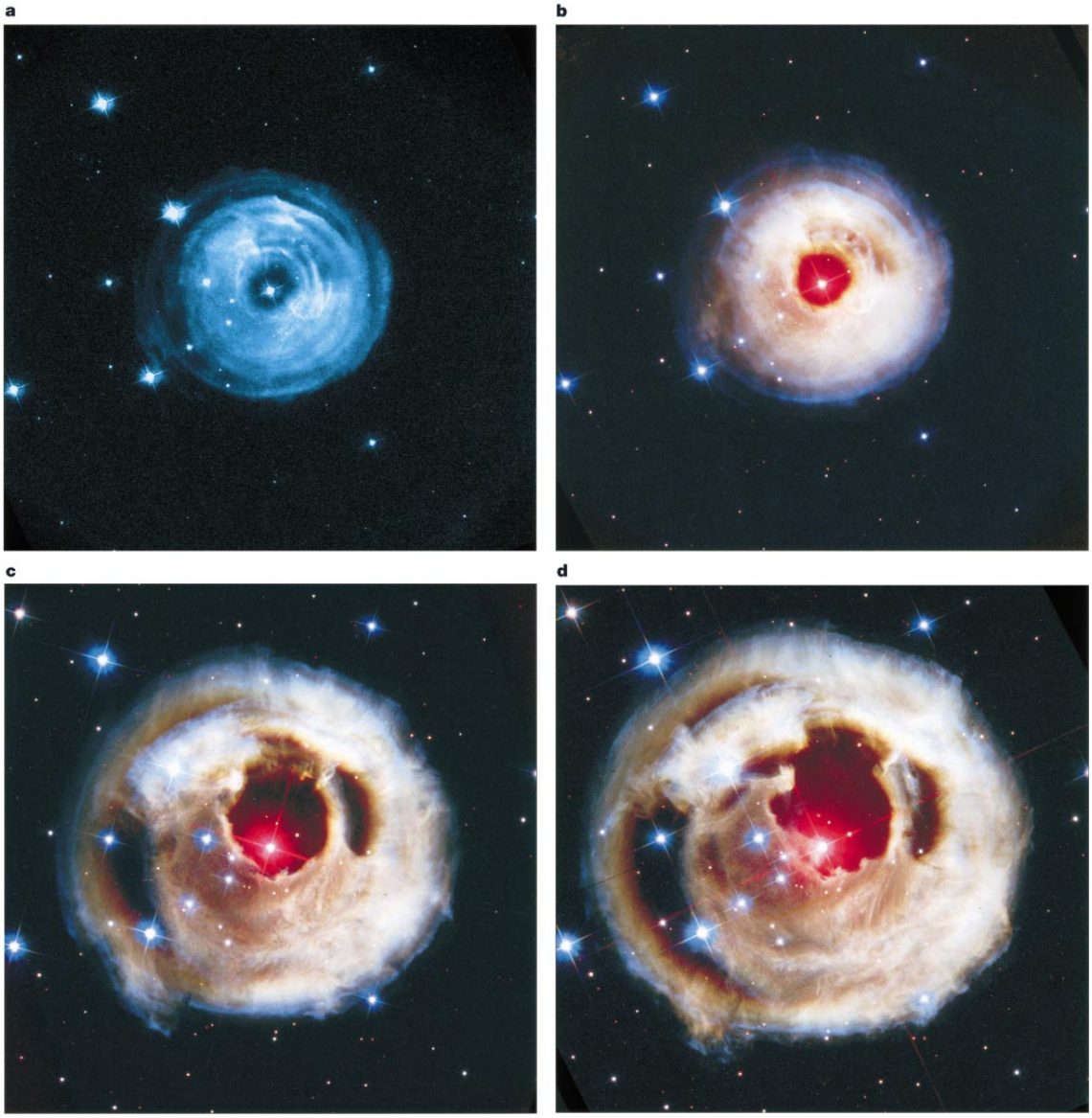

Figure 26. The light from the outburst of V838 Mon is reflected by the previously non-emitting CSM around the progenitor. The *HST* images are stacked BVI frames except **a** which was observed only in B. Frames were obtained in 2002 on 30 Apr (**a**), 20 May (**b**), 2 Sep (**c**) and 28 Oct (**d**). Adopted from Bond et al. (2003).

Due to the low brightness and rarity, the number of observed ILRTs and LRNe is still quite low and limited to a handful of well-sampled objects. More recent discoveries include ILRT AT 2017be (Cai et al., 2018, Section 6.2.5) as well as LRNe M101 OT2015-1 (Blagorodnova et al., 2017, Section 6.2.3) and M31LRN 2015 (MacLeod et al., 2017; Lipunov et al., 2017).

4 Telescopes and instrumentation

The two main telescopes used in the data acquisition of the presented research project were the Nordic Optical Telescope (NOT) and the New Technology Telescope (NTT). Observational transient projects typically involve several telescopes of varying sizes in order to secure the evolution of the objects throughout the different phases of interest. Aforementioned telescopes are considered as mid-sized based on the diameter of the main mirror. They can reach fairly deep limiting magnitudes with reasonable exposure times compared to small telescopes. In the following, the telescopes and key instrumentation available at the time of the observations are discussed.

4.1 The Nordic Optical Telescope

The NOT is a 2.56 m Ritchey-Chretien type telescope located at an elevation of 2382 m on La Palma in the Canary islands, Spain[13]. Various instruments in the optical and near-IR wavelengths are offered[14]. Additionally, the use of visitor instruments is possible. The main instruments used in this work are the Nordic Optical Telescope near-infrared Camera and spectrograph (NOTCam)[15] and the Alhambra Faint Object Spectrograph and Camera (ALFOSC)[16], which are more thoroughly introduced below. (Djupvik & Andersen, 2010)

4.1.1 NOTCam

NOTCam is a Short-Wave InfraRed (SWIR) instrument that provides imaging and spectroscopic observing modes. It has an 1k x 1k HgCdTe "HAWAII" near-IR array that is cooled with liquid nitrogen and helium. A lens wheel allows a quick switch in between Wide Field (WF) and High Resolution (HR) camera modes. The WF mode enables imaging with a 4 x 4 arcmin^2 field and a scale of 0.234 arcsec/pixel or spectroscopy with a

[13] www.not.iac.es/telescope/tti/technical-details.html

[14] www.not.iac.es/instruments/instruments.html

[15] www.not.iac.es/instruments/notcam/

[16] www.not.iac.es/instruments/alfosc/

lower resolution of $R = 2500$ in Y, J, H and K bands. The HR mode, on the other hand, provides a field of 80 x 80 arcsec^2 and a scale of 0.078 arcsec/pixel or a higher spectral resolution of $R = 5500$ in J, H and K bands.

Several broad and narrow band filters are offered in between the Z and K bands ($\lambda \sim 0.8 - 2.4\,\mu$m). NOTCam has two filter wheels with 16 slots each i.e. up to 30 different filters can be mounted at a time.

A grism wheel also has 16 slots although, typically, only one grism and a focus pyramid are mounted. Desired wavelength region is selected with an additional filter. A 12-slotted aperture wheel provides a slit for each camera mode. Furthermore, it also has appropriate masks for each camera mode and pinholes for calibration.

Lastly, a wheel with 16 slots in the pupil plane holds a selection of Lyot stops and Hartmann masks. Due to the cooling requirements, NOTCam is rarely opened. Warm-up, maintenance and cooling back to operational temperature takes several days. This means that any setup of optical elements is fixed for an extended amount of time.

There is no calibration unit in NOTCam. However, halogen, argon and xenon lamps are mounted under the telescope baffle that can be used to obtain spectroscopic calibration frames (halogen for flats, argon and xenon for wavelength) when the mirror covers are closed. Closing and opening the mirror covers during the night obviously introduces some overhead in the required time to execute the observations.

4.1.2 ALFOSC

ALFOSC is an optical instrument that can be used in imaging, spectroscopic and polarimetric observing modes. It operates in between the u and z bands ($\lambda \sim 3000 - 10000$ Å) and has a 2k x 2k charge-coupled device (CCD) detector[17] that is cooled with liquid nitrogen. ALFOSC has a field of 6.4 x 6.4 arcmin^2 with a scale of 0.2138 arcsec/pixel.

A wide selection of narrow and broad band filters are offered. Intrinsically, ALFOSC

[17] CCD14 in the NOT listings.

has an eight-slotted filter wheel that is accompanied by two external Filter And Shutter Units (FASUs). Both of these have seven slots for optical elements. Therefore, a total of up to 19 different filters are available during a given night as one of the slots in each wheel has to be open (i.e. without an optical element). Some of the filters, such broad band Johnson-Cousins and SDSS filters, are mounted permanently for target of opportunity (ToO) observations. Additionally, it is possible to insert grisms to the filter wheel for Echelle mode.

Several grisms of varying wavelength coverage and resolution are offered. Various spectroscopic modes are achieved with a selection of slits with different widths. As with the intrinsic filter wheel, ALFOSC grism and aperture wheels both have eight slots. Not all of these are available, however. The grism wheel also hosts a "Wedged Double Wollaston" (Oliva, 1997) used in one-shot polarimetry and a focus pyramid[18]. The aperture wheel, on the other hand, must have a pinhole mask and a calcite plate mounted. These are used for calibration and polarimetric observations, respectively. Certain setups are also permanently mounted for ToO observations. Multi-object spectroscopy (MOS) masks can also be mounted to the aperture wheel slots.

There is also an external one-slotted unit needed for polarimetry. It holds either a $\lambda/2$ or a $\lambda/4$ plate. Both imaging and spectroscopic polarimetry are supported. Unlike with NOTCam, the optical elements of ALFOSC are easily changeable and, in principle, completely different setups can be used in consecutive nights.

Furthermore, an external calibration unit provides lamps for spectroscopy. Multiple options are available for wavelength calibration: helium, neon and thorium-argon lamps. For full wavelength coverage, helium and neon can be used simultaneously. A halogen lamp is available for flat fields.

[18]A focus pyramid splits the light from a point source into two images both in x and y directions on the CCD. This produces a "cross" shape that can be used to focus the telescope. The separation of the two images is related to the telescope focus.

4.2 The New Technology Telescope

The European Southern Observatory (ESO) NTT is a 3.58 m Ritchey-Chretien type telescope located at an elevation of 2375 m in La Silla, Chile[19]. Two instruments are offered. The ESO Faint Object Spectrograph and Camera v.2 (EFOSC2)[20] is the main instrument used in this work and will be described below. The other instrument available is the Son OF Isaac[21]. It operates in the near-IR wavelengths ($\lambda \sim 0.9 - 2.5\ \mu$m) and provides both imaging and spectroscopic ($R \sim 600 - 2200$) capabilities.

4.2.1 EFOSC2

EFOSC2 (Buzzoni et al., 1984; Snodgrass et al., 2008) is an optical instrument that offers several options: imaging and spectroscopy in normal and polarimetric modes as well as MOS and coronography. It operates in wavelength region of $\lambda \sim 3050 - 11000$ Å covering bands from U to z. EFOSC2 is equipped with a 2k x 2k CCD detector[22] that has a field and scale of 4.1 x 4.1 arcmin^2 and 0.12 arcsec/pixel, respectively.

An 11-slotted filter wheel provides a selection of ten different filters on a given night. Broad-band Bessel and Gunn filters as well as most common narrow-band filters, including rest-wavelength Hα, Hβ and [O III], are offered.

A grism wheel enables the use of seven different grisms on a given night. An aperture wheel has a total of ten slots but, due to calibration elements such as a pinhole mask and certain slits, only five slots are available for desired slits or MOS, coronographic or Wollaston masks. Resolutions achieved with any grism and slit combinations are in the order of $R \sim 10^2 - 10^3$.

Additional unit holds either a $\lambda/2$ or a $\lambda/4$ plate for polarimetry. A Wollaston prism is also needed but the mount place depends on the observing mode. For imaging polarimetry,

[19] `www.eso.org/sci/facilities/lasilla/telescopes/ntt/overview/techdetails.html`

[20] `www.eso.org/sci/facilities/lasilla/instruments/efosc.html`

[21] `www.eso.org/sci/facilities/lasilla/instruments/sofi.html`

[22] CCD40 in the ESO listings.

the grism wheel is used whereas for spectropolarimetry a slot in the filter wheel is required. Two Wollaston prisms with different image separations are offered.

Finally, a few calibration lamps are available. Helium and argon lamps for wavelength calibration and a quartz lamp for flat fields.

5 Observing programmes

In the following, I first describe my position at the NOT as a student support astronomer (SSA, 19 months in P49 – P52: April 2014 – March 2016) and the main observing programmes to which I have effectively contributed. In most cases, I am one of the co-investigators. For two successful NOTCam proposals, I was the Principal Investigator (PI) who takes responsibility in submitting the proposal and organising the observations.

Secondly, normal programmes are listed. These programmes run during one semester (half a year). A new proposal must be submitted if more observing time is desired. Typical amounts of time are a few nights spread out throughout a semester.

Then, an introduction to two large programmes is given. These run during several semesters and are usually awarded with extensive amount of observing time. The large programmes are the NOT Unbiased Transient Survey (NUTS)[23] and the (extended) Public ESO Spectroscopic Survey for Transient Objects ((e)PESSTO)[24]. NUTS is a three-year programme (P53 - P58: April 2016 – March 2019) running at the NOT. PESSTO was originally a five-year programme (P89 – P98: April 2012 – March 2017) that was extended for two more years (P99 – P102: April 2017 – March 2019) as ePESSTO.

Finally, all programmes are summarised in Section 5.4.

5.1 NOT studentship

The NOT offers an opportunity to get hands-on experience at a professional telescope. Up to six students (late MSc or early PhD are preferred) at a time are working with the local staff to run the telescope. Typically, a studentship is awarded for one year. On average, one is expected to support visiting observers or perform service observations during three nights per month. There is a three-month training period where more than average amount of nights are typically spent at the telescope. After the training, a student is expected to be

[23] `http://csp2.lco.cl/not/`

[24] `www.pessto.org`

able to work alone at the telescope. In practice, I primarily carried out service observations of my own with a few exceptions when I provided support for visiting observers. My studentship started in early June 2014 and ended in late December 2015.

The SSA tasks are diverse. Already before driving up to the telescope, observations should be planned. Additionally, at the same time, it is convenient to compile a list of optical elements and calibration frames required by the programmes. Planning includes checking the observing queues of the mounted instrument (ALFOSC or NOTCam) and the always available FIbre-fed Echelle Spectrograph (FIES). If a monitoring or a fast-track programme[25] is allocated for a particular night, it is added to the plan. Monitoring and fast-track programmes are usually scheduled to be observed during so called Nordic Service or Technical nights. These nights are often shared with service programmes that consume part of the time. Occasionally, planning can be somewhat of an optimisation problem as one would prefer observing targets at as high an altitude as possible in order to minimise atmospheric effects. With overlapping targets (in visibility) this is not always possible.

After driving up to the telescope in the afternoon, a check should be made whether or not any ToO observations are triggered. One should always be prepared for these triggers and it requires some flexibility to adjust the plan accordingly, as a trigger may have an override capability. In other words, a ToO programme may have a higher observational priority and gets to be observed instead of some previously allocated programme. In extreme cases, such as certain transient programmes, a hard override can be triggered in the middle of the night instantly interrupting whatever is observed at that moment.

If an instrument change is required, it should be preformed next. This is usually not the case, but requires additional quality monitoring to be done afterwards. In case ALFOSC is used, change of optical elements (filters, grisms or slits) that are demanded by the

[25]Monitoring time is awarded via normal proposals, whereas fast-track proposals can be submitted at any time for a quick review and possible time allocation. Fast-tracks are quick observations (up to four hours) whereas monitoring programmes often have more time spread out throughout a semester.

programmes may be needed. Furthermore, ALFOSC requires refilling of liquid nitrogen before and after the observations whereas NOTCam is refilled only after the observations. After the plan is set and the instrument(s) prepared, it is time for dinner followed by a night of observing as planned. Or, whenever needed, adjusting observations due to weather or technical issues.

5.2 Normal programmes

Two main programmes at the NOT, in which I was a co-investigator, are the monitoring programme *Studies of peculiar supernovae with NOT and TNG* and the ToO programme *Survey of nuclear transient in galaxies with Gaia*.

5.2.1 Studies of peculiar supernovae with NOT and TNG

This joint Nordic-Italian observing programme was already running at the time I started as a NOT SSA in period P49 (April 2014 – September 2014). The purpose of the programme was to classify and follow-up interesting SNe in optical and near-IR wavelengths. Infrared observations were obtained with the NOTCam (PI: Erkki Kankare) and optical with both the ALFOSC and with the DOLORES[26] instrument at the Telescopio Nazionale Galileo (TNG, PI: Nancy Elias-Rosa).

After my SSA training, I carried out observations of almost all of the NOTCam nights and most of the ALFOSC nights. In both cases, these programmes had half a night once every 3-4 weeks allocated to them. Therefore, even though I was provided a target list by the PI, I had to plan how to include also possible monitoring, fast-track and ToO observations among them.

Starting in P51 (April 2015 – September 2015) I became the PI of the NOTCam programme. In addition to observing, I also compiled the target lists from the active objects, reduced the data and distributed processed frames to collaborators. The reduction were

[26]Device Optimized for the LOw RESolution, 2k x 2k optical camera and spectrograph.

carried out using a slightly modified version of a dedicated IRAF[27] package[28] provided by the NOT.

Eventually, both programmes were merged as a part of the large NUTS programme in P53 (April 2016 – September 2016). I remained as the PI of the NOTCam programme until that. After my studentship at the NOT, I was still responsible for providing the NOTCam target lists to the observers and reducing those data for the collaboration until May 2017 (P55).

5.2.2 Survey of nuclear transient in galaxies with Gaia

This ToO programme (PI: Seppo Mattila) run during periods P51 - P52: April 2015 – March 2016. The main purpose of this programme was to classify transients detected by the *Gaia* satellite in the nuclear regions of galaxies. My main responsibility, as a NOT SSA at the time, was to write the observing scripts that were used by whoever happened to be observing when a trigger was sent. The use of scripts made the observations consistent, easy to execute and less prone to human error. This programme was also merged into the NUTS large programme.

5.3 Large programmes

Although similar in their goal to classify and monitor transient events, NUTS and (e)PESSTO have quite different observing strategies. NUTS time is divided partially into ToO time and partially into pre-allocated monitoring half-nights. Local staff at the NOT perform all of the observations in service mode. (e)PESSTO, on the other hand, sends observers to the NTT for a month at a time. All observing time is, therefore, in visitor mode.

[27] Image Reduction and Analysis Facility, `http://ast.noao.edu/data/software`

[28] v.2.5, `www.not.iac.es/instruments/notcam/guide/observe.html#reductions`

5.3.1 NUTS

The NUTS collaboration (PIs: Seppo Mattila, Maximilian Stritzinger, Peter Lundqvist, Nancy Elias-Rosa) is the result of merging several transient-related programmes running in parallel at the NOT. The main institutes involved are University of Turku, Aarhus University, Stockholm University and the Astronomical Observatory of Padova. Additionally, collaborators from UK, Ireland, Poland, US, China and Chile are participating. The collaboration has increased in numbers throughout the years.

As I was a beta-tester of so-called Observing Block (OB) system at the NOT[29], my first duty in NUTS was to prepare template OBs and write an instructional manual how to use the system for the collaboration. Essentially, an OB is a self-consistent set of observations that holds target (coordinates, finding chart etc.), observing (imaging or spectroscopy; filters, grisms, slits, exposure times etc.) and technical (CCD windowing, spectral calibrations etc.) information.

Templates are used in order to produce consistent observations from epoch to epoch. In practice, this means that it is enough to provide target and observing information while technical details are left as they are. The NOT OB system is a web-based system that can be accessed anywhere. A number of sanity checks are performed while filling the information and upon submission. If the OBs make sense, they can be used to generate observing scripts at the telescope. If not, mistakes must be corrected by the user.

In addition to the NOTCam data reductions, I was a part of the so-called NUTS ToO rota. The active rota member is responsible for collecting targets and sending ToO triggers of ALFOSC observations to the NOT for one week at a time. In case transient classification spectra were observed, the volunteer is also expected to reduce and classify the spectra using a dedicated pipeline[30] and the expertise of the collaboration. Finally, the volunteer

[29] `www.not.iac.es/observing/forms/ob/`

[30] Foscgui is a graphic user interface aimed at extracting SN spectroscopy and photometry obtained with FOSC-like instruments. It was developed by E. Cappellaro. A package description can be found at http://sngroup.oapd.inaf.it/foscgui.html.

submits an Astronomer's Telegram (ATel)[31] and provides the spectra available for the community via the Transient Name Server (TNS)[32]. In reality, it is not possible to send triggers every night but, typically, one to three nights a week. This is due to time allocation rules. For instance, Spanish time (as the telescope is located in a Spanish observatory) cannot be overridden by Nordic ToO triggers.

5.3.2 PESSTO and ePESSTO

The (e)PESSTO (PI: Stephen Smartt) was a large programme running at the ESO NTT. As an ESO programme, several European institutes are involved in running the programme. Additionally, many non-European institutes around the world are participating.

I was included as a member in October 2014 (P94) and therefore I could lead follow-up campaigns of targets within (e)PESSTO. In November 2015 (P96) I travelled to Chile as an observer for ten nights that where distributed to three subruns throughout the month. During the first two subruns I was a second observer and during the last subrun the primary one. The observers are responsible for selecting active objects with different priorities from a list of requests sent by the collaborators. This is done during the day time while simultaneously preparing OBs for the night. During a night, a telescope operator is asked to execute these OBs in the order the observers require.

Later, in October 2018 (P102), I was a part of the support group whose duty is to reduce the data right after the observers at the NTT have finished their ePESSTO night. This is done with the PESSTO pipeline[33]. Reduced spectra are then sent to the Weizmann Interactive Supernova Data Repository (Yaron & Gal-Yam, 2012)[34] where they are easily accessible. Additionally, if any classification spectra were obtained, these objects are classified by the support team and confirmed by the collaboration. Finally, an ATel is submitted as well.

[31] `http://www.astronomerstelegram.org/`

[32] `https://wis-tns.weizmann.ac.il/`

[33] http://wiki.pessto.org/pessto-operation-groups/data-reduction-and-quality-control-team

[34] `https://wiserep.weizmann.ac.il/`

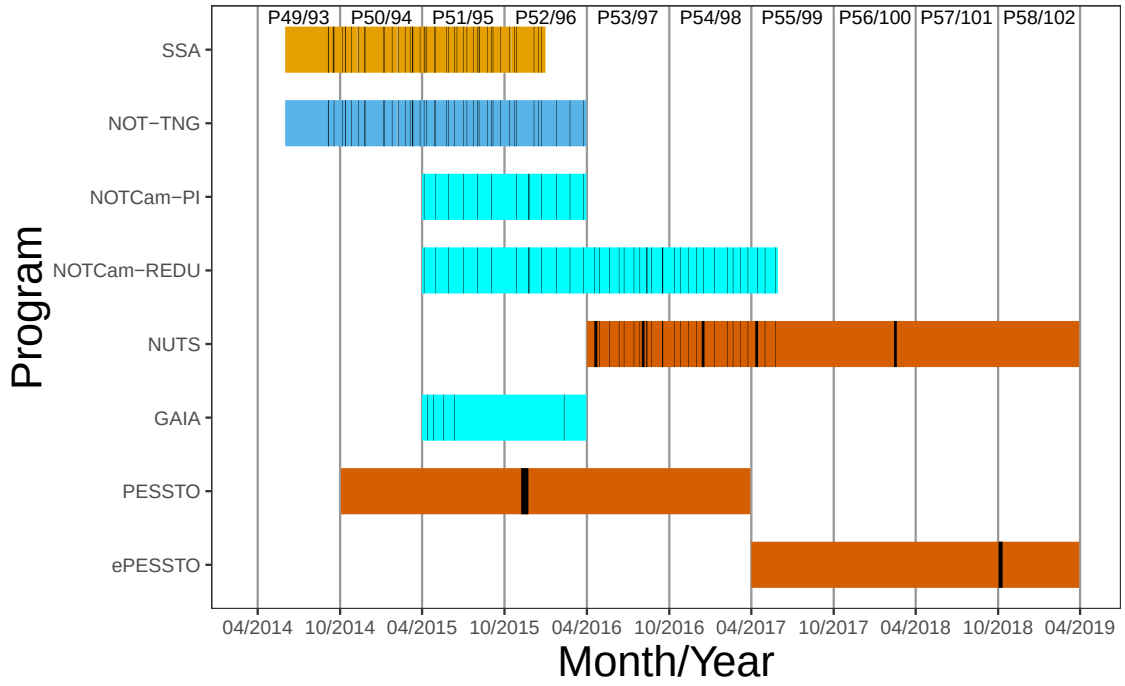

Figure 27. Time lines of different programmes. Period numbers are indicated on the top. NOT-related normal programmes are marked in different shades of blue, large programmes in red and my time as a NOT SSA in orange. Vertical bars depend on the programme in question. In SSA black lines are my nights as an observer (including nights that were partially observed by a visitor) and grey lines when I was supporting a visitor run. Thicker lines indicate consecutive nights. In NOT-TNG programme black lines indicate nights when I was observing with ALFOSC or NOTCam. A gray line indicates a support night as well. NOTCam-PI shows the nights when I did the planning and observations for the programme. NOTCam-REDU indicates the times I reduced the near-IR data for the collaboration. In NUTS, thicker lines indicate the weeks when I was on ToO duty and the other lines indicate the times I planned the NOTCam nights. In GAIA vertical lines indicate the times we classified objects and submitted ATels. In PESSTO and ePESSTO the thick bars indicate the time I was observing and supporting, respectively, for the collaboration. Note that *my* time in PESSTO is illustrated here, the programme had been running since 2012.

5.4 Summary

All of the aforementioned programmes are summarised in Fig. 27.

6 Results

Because of my active participation in collecting and processing data, I have been a co-author of several refereed articles. I have, of course, participated also in the writing of these articles and provided comments. Additionally, I am the first author of a number of ATels as well as a co-author in many. Selected papers and all transient classification ATels are reviewed below.

6.1 Astronomer's Telegrams

In between March 2015 and November 2018 I have (co-)authored 59 ATels. Out of these, 56 include classifications[35] of transients and are included in the following considerations. In seven occasions I was the first author. A full list of 111 objects classified is shown in Appendix A.

It should be emphasised that there is no clear selection criteria for this sample. Targets observed were part of various programs with somewhat different goals and policies. Generally, these programs are focused on SNe, ILOTs and more exotic transient events, such as tidal disruption events, TDEs (e.g. Mattila et al. (2018) and references therein) and electromagnetic counterparts to gravitational wave events (e.g. Smartt et al. (2017) and references therein). A rough criterion could be defined as follows: a transient to be classified should be $M = -10$ mag or brighter at maximum light and belong to the aforementioned classes of transients.

However, with no light curve information or distance estimate, a new Galactic Cataclysmic Variable (CV), for instance, projected on a background galaxy could *look* like a SN before a spectral classification is available. Additionally, in a previously quiescent galaxy, it can be difficult to distinguish in between an outburst of an Active Galactic Nucleus (AGN) and a TDE without spectral information. Both of these can be caused by the activity of a central supermassive BH of a galaxy. Due to these uncertainties, classifica-

[35] See Sections 1.2 and 3.

tions of AGNs, CVs etc. are inevitable although not desired.

A pie chart of the fractions of different objects classified as well as their redshift distribution is shown in Fig. 28. Five of these did not have a reported redshift estimate. The relative fractions of transients are as expected (comparison is also shown in Fig. 28) for a *magnitude-limited* sample : SNe Ia are, by far, the most frequently observed class. Among CCSNe, Type II are more common than Type Ib/c.

The redshift distribution is also easy to understand. It peaks around $z \sim 0.01 - 0.03$ where the objects are still relatively bright due to close proximity but far enough to fill an adequate observable volume to counter the low event rates. *Other* objects are located either nearby $z < 0.01$ or far away $z > 0.18$. This was partially explained already. Faint nearby transients, such CVs, are located in our Galaxy. Poor detections (Unknown) and distant but bright AGNs are causing the tail in the distribution.

Due to low sample size, there seem to be peculiarities in certain bins. For instance, there seems to be no SNe Ia in the local universe whereas in $z \sim 0.04 - 0.05$ there are no other classes than SNe Ia observed. This is not a real effect, but just a coincidence due to low sample size.

Figure 29 shows the location distribution of objects in the equatorial coordinate system. Immediately obvious difference is the location of the observatories. The NOT is located in the northern hemisphere (observatory latitude $l_{obs} = +28° 45' 26.2''$ N) whereas the NTT is in the southern hemisphere ($l_{obs} = -29° 15' 32.1''$ S). For both telescopes, the majority of the observed targets are located roughly $l_{obs} \pm 40°$ in declination, which means there is some overlap around the Equator.

Different observing strategies are also evident. As mentioned before, (e)PESSTO observers and support teams are working for a month at a time. In my case, the two runs happened to take place around the same time of the year. An observing run in November 2015 and a support run in October 2018. This lead to a gap in right ascension ($\sim 11-19$ h). The ToO programs at the NOT, on the other hand, made active participation throughout

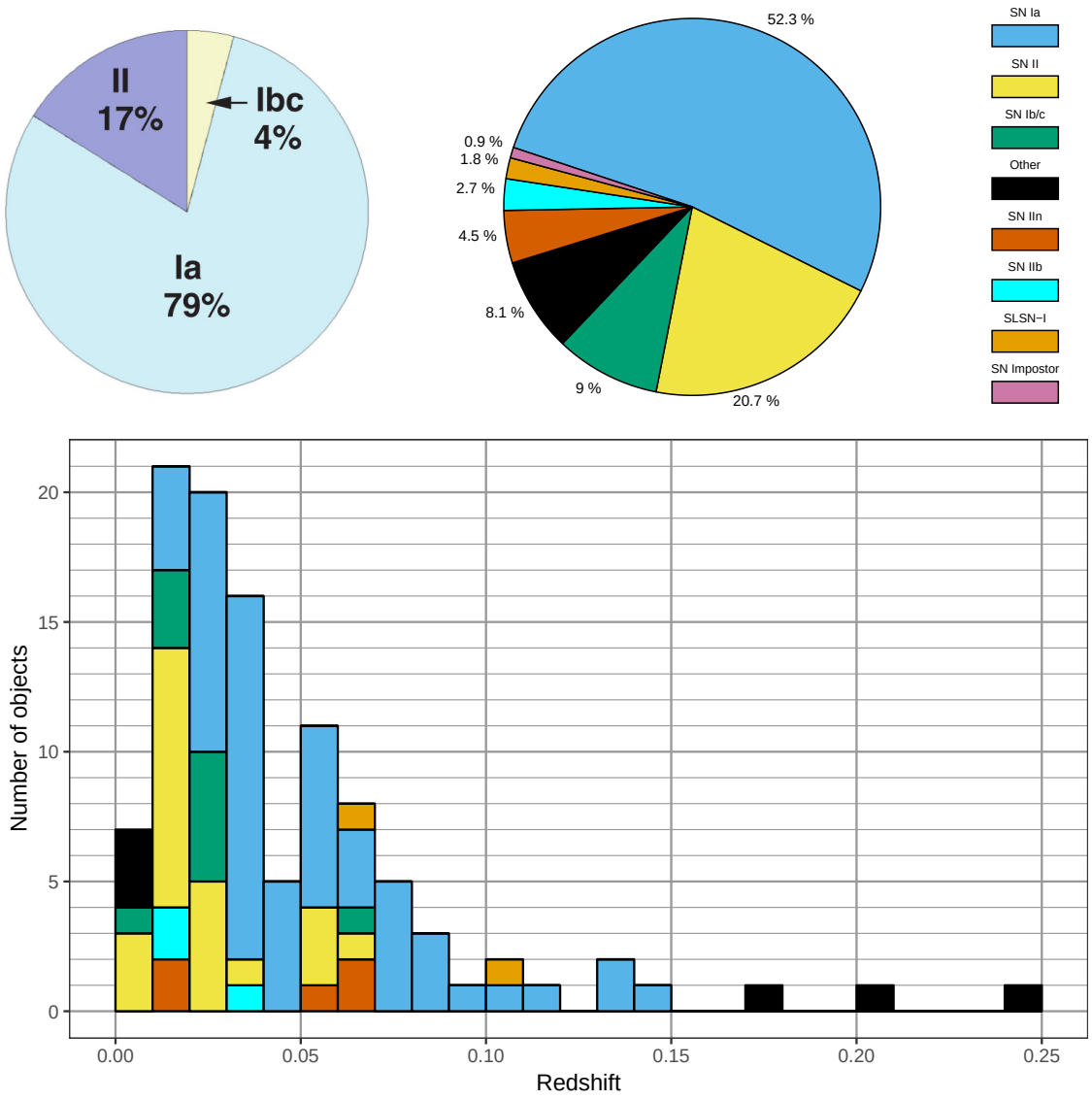

Figure 28. Relative fractions (top) and redshift distribution (bottom) of classified objects. Colour coding is the same in both figures. Bin width in the redshift plot is $\Delta z = 0.01$. The only SN Impostor classified is missing redshift information and, therefore, not shown in the bottom plot. Various subclasses are merged together in order to improve the readability of the plots. For instace, SNe Ib and Ic are shown as SN Ib/c. Observed AGN, stellar variabilities, CVs and Unknown objects are grouped as *Other*. Additionally, a similar pie chart adopted from Li et al. (2011a) is shown on the left for comparison. Note that in their chart only the main classes are shown. See Fig. 11 in Li et al. (2011a) for plots of more thorough subclassification.

the year possible and, therefore, such a gap is not formed.

Additional effect of the different observing strategies is the amount of objects classified per ATel. A total of 62 classifications were reported in 42 ATels with the NOT, whereas

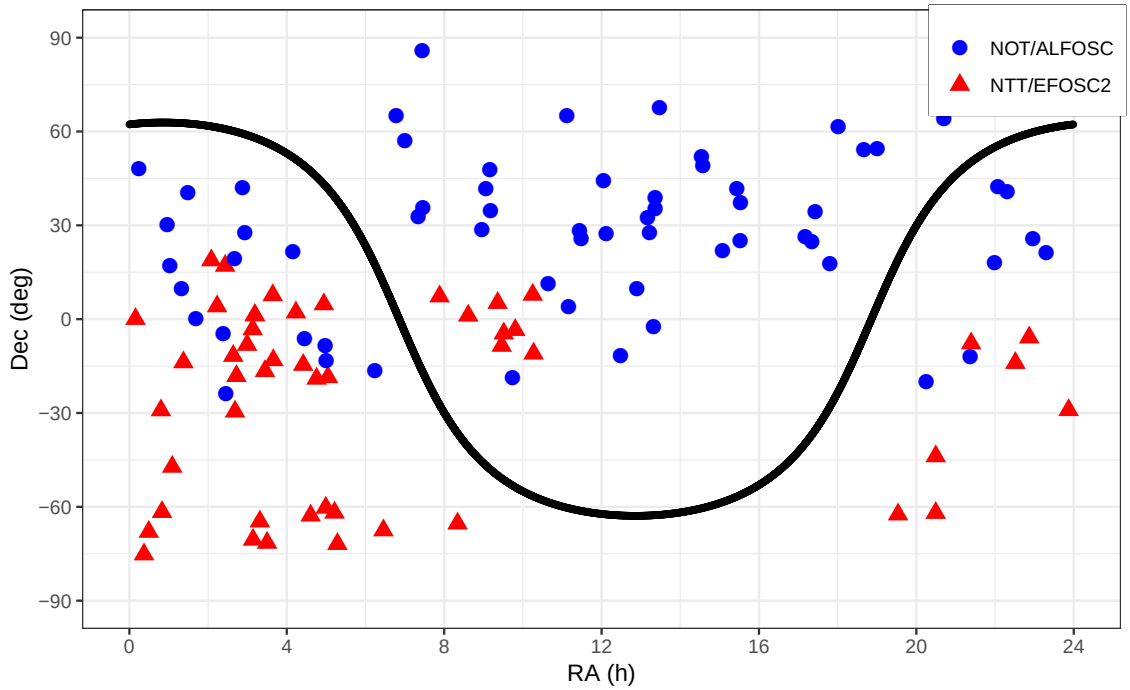

Figure 29. Right ascension (RA) – declination (Dec) distribution of classified objects. The approximate location of the galactic plane[37] is drawn in black.

49 objects were reported in only 14 ATels with the NTT. The average number of classified objects per ATel is roughly 1.5 and 3.5 for the NOT and the NTT, respectively.

One interesting feature seen in Fig. 29 is the fact that, generally, the target selection seems to avoid the galactic plane. This is can be understood as an attempt to avoid Galactic objects that may appear like extragalactic transients. Of course, the line-of-sight extinction is larger in the plane, especially towards the centre of the Galaxy.

6.2 Journal Articles

In between September 2015 and November 2018 I had co-authored 26 refereed journal articles. Almost all of them are based on observations of transient events, including SNe, ILOTs, TDEs and a kilonova. In the following, I will review five of them in a chronological order. They discuss the observations and interpretation of transients showing narrow emission lines. Candidates of both SNe IIn and ILOTs are represented. I will also describe

[37]Data from `https://gist.github.com/barentsen/6c100b27d26f361ce63ad747366cfa83`

my observational and data processing contributions to these results. Full list of articles I have co-authored is included in Appendix B.

6.2.1 SNhunt248

The results of SN impostor SNhunt248 were published by Kankare et al. (2015). The transient was originally discovered in 21 May 2014 and, therefore, the follow-up campaign was already on-going when I started as a NOT SSA. SNhunt248 was monitored throughout roughly one year. I contributed in all of the near-IR observations with NOTCam, first as a trainee and afterwards as the main observer for most of the epochs. Several epochs of complementary optical photometry were obtained during these nights using StanCam. Additionally, I observed one spectrum with ALFOSC.

The light curves and colour evolution fits of SNhunt248 are shown in Fig. 30. Historical data show ± 1 mag variations during the past 15 years before the outburst. The observed light curve is characterised by three distinct peaks. The first peak has a maximum of $M_R \approx -11.4$ mag, the second $M_R \approx -15.0$ mag and the last $M_R \approx -14.4$ mag. Photometric evolution is similar to SN 2009ip, but fainter by several magnitudes (see also Fig. 32).

Spectral evolution of SNhunt248 is shown in Fig. 31. Early spectra exhibit narrow Balmer and metal lines with strong absorption components. There is not much evolution except for the absorption components of the Balmer lines. Absorption is observed in the first spectrum, but vanishes before the second peak is reached. Before the third peak is reached, the absorption components reappear showing the same velocity as before.

Blackbody fits (Fig. 30) to archival data obtained roughy 2 years before the outburst suggest that the progenitor was not an LBV but a yellow hypergiant (YHG) instead. They are also unstable stars prone to variability and eruptions. The first peak in the light curve was probably produced by such an outburst and, based on the spectral evolution, it is likely that the later peaks were a consequence of interaction with previously ejected shells. In

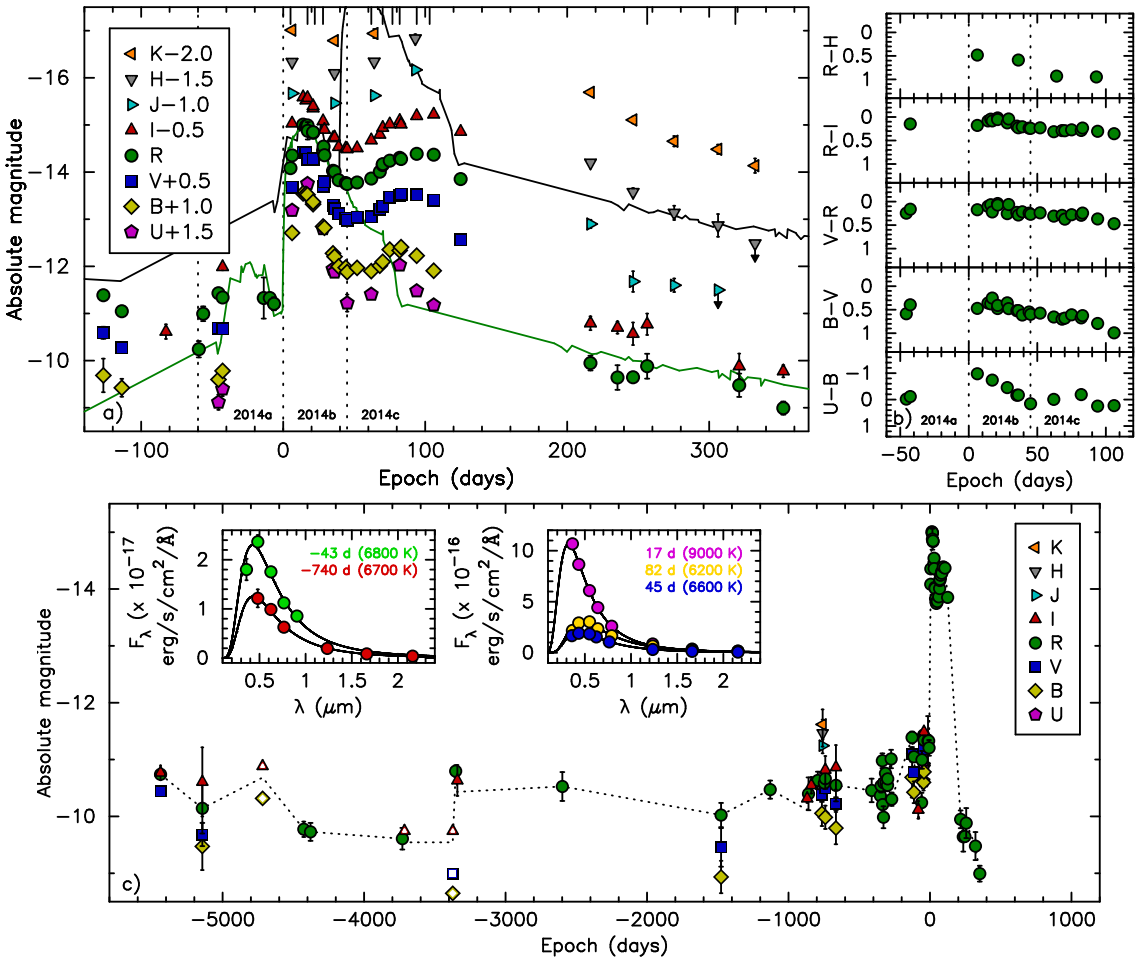

Figure 30. Light curves (top, left), colour evolution (top, right) and historical light curve (bottom) of SNhunt248. Solid lines on in the light curve plot are the *R*-band light curves of SN 2009ip. Black curve is the observed one and green is shifted by +3.0 mag and −40 days to emphasise similarities in evolution. Blackbody fits of selected epochs are shown in the inserted figures in the bottom panel. Adopted from Kankare et al. (2015)

other words, SNhunt248 was most likely not a terminal explosion.

Recently, Pastorello et al. (2019b) presented additional data and interpreted SNhunt248 as a LRN i.e. a probable stellar merger. This would also support a non-terminal scenario for this event, although the event itself would be completely different.

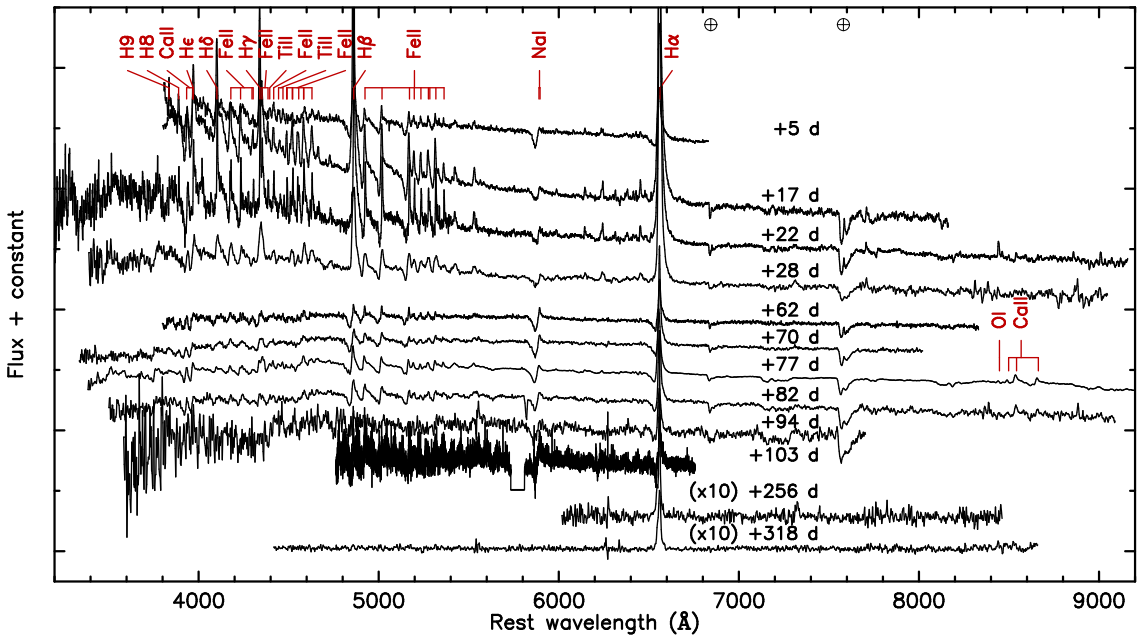

Figure 31. Spectral evolution and line identification of SNhunt248. Adopted from Kankare et al. (2015)

6.2.2 SN 2015bh

The results of SN 2009ip[38] -like transient SN 2015bh were published by Elias-Rosa et al. (2016). The object was discovered on 7 February 2015 and was monitored during a period of roughly 14 months. Most of this time I was a NOT SSA. I contributed in most of the NOTCam near-IR epochs (observations and data reductions) as well as in several optical ALFOSC epochs (observations), including both imaging and spectroscopy.

Pseudo-bolometric light curve comparison is shown in Fig. 32 (see also Fig. 36 in Section 6.2.4). SN 2015bh is characterised by a slow rise of $\sim$ 1.5 mag during the first 100 d after the discovery followed by a quick brightening of $\sim$ 3 mag in about a week to a peak of $M_r \approx -17.81$ mag. After this the light curve slowly declines. The historical light curve of SN 2015bh exhibits variability during several years prior to the brightening in 2015.

Selected spectral epochs of SN 2015bh and their comparison to other events is shown in Fig. 33. See also Fig. 6 in Elias-Rosa et al. (2016). The early spectra (before the onset

[38] See Section 3.1.1.

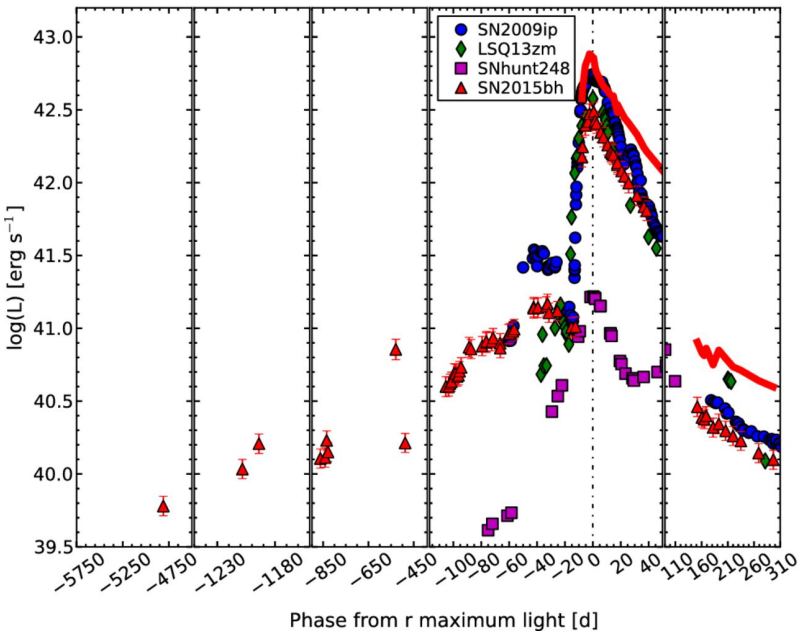

Figure 32. Pseudo-bolometric light curve comparison. SN 2015 is shown as red triangles (optical) and in a red thick line (UV-optical-IR). Origin is set to the brightest peaks. Comparison is made to SN 2009ip, LSQ13zm and SNhunt248. The latter is clearly less luminous than SN 2009ip -like events. Adopted form Elias-Rosa et al. (2016).

of the second brightening) are dominated by Balmer lines showing multiple components and a forest of Fe II lines. The photospheric temperature peaks at $T_{BB} \approx 8500$ K and declines down to $T_{BB} \approx 7100$ K before the re-brightening.

During the second peak the photospheric temperature rises to $T_{BB} \approx 20\,000$ K and the Fe II lines disappear while He I lines emerge. After about two weeks post-maximum, the Fe II lines begin to reappear. Unfortunately, the follow-up is interrupted by the seasonal gap for over three months.

After this time, the spectral features have completely changed. For instance, early Hα emission profile is well-fit with a broad and a narrow component. At late times, however, the emission profile exhibits three broad components out of which one is clearly separate (blueshifted) from the others (see Fig. 33 insert c)). In all cases, an additional P Cygni absorption component is included whenever appropriate. Additionally, lines of Ca II and O I are detected in the late time spectra.

Similar to SN 2009ip, the evidence points towards a terminal SN explosion of the pro-

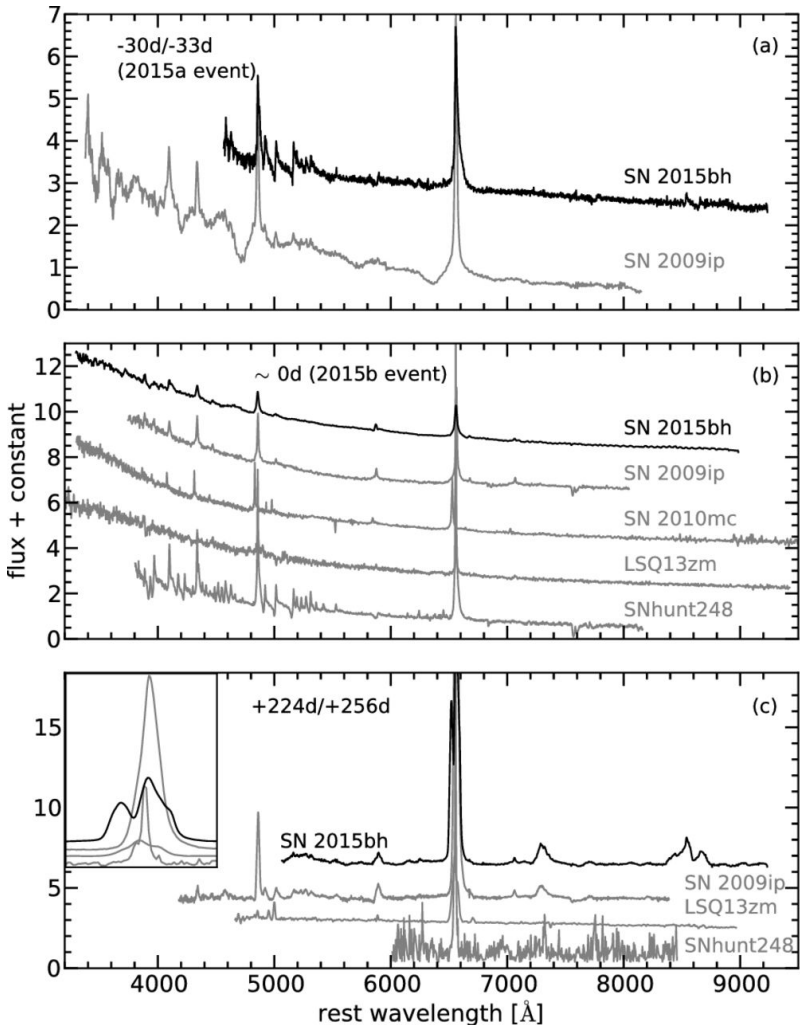

Figure 33. Three spectra of SN 2015bh compared to other events during similar phases: SNe 2009ip and 2010mc, LSQ13zm and SNhunt248. Events 2015a and 2015b refer to first and second peak, respectively, of SN 2015bh in 2015 similarly to the peaks of SN 2009ip in 2012. Zoom-in of Hα profiles is also shown in panel c). Adopted form Elias-Rosa et al. (2016).

genitor of SN 2015bh causing the first peak in 2015. The second peak would be caused by the interaction between the SN ejecta and a dense CSM produced by an earlier progenitor outburst. Disappearance of the other lines than H and He supports this interpretation. Spectral features observed at late times suggests that the CSM is asymmetrical and, therefore, emission from different environments is seen. In certain areas the interaction is still on-going while also nebular SN lines are tentatively detected.

6.2.3 M101 OT2015-1

The results of a LRN M101 OT2015-1 (M101-OT henceforth) were published by Blagorodnova et al. (2017). The discovery of the transient was announced on the 10th of February 2015. Additionally, the iPTF survey had internally classified the progenitor as a slowly rising object already in 2013 – 2014. My contributions ranged from the SSA period all the way to the early months of the NUTS collaboration. I contributed in all NOTCam near-IR observations and reduced almost all of the data. Additionally, I observed several epochs of optical imaging and spectroscopy.

Light curves of M101-OT are shown in Fig. 34. The evolution is characterised by two brightening episodes on 11 November 2014 and 17 February 2015 with peak magnitudes of $M_r \leq -12.4$ mag and $M_r \leq -12.0$ mag, respectively. After the second peak there is a phase of fast decline for about 40 days followed by a plateau for roughly 60 days. After this the rapid decline resumes.

Due to the close proximity of M101, there is plenty of archival data available. The historical light curve, spanning 15 years before the discovery, shows no major variability up to approximately 6 years before the outbursts. The progenitor slowly brightened by 1.5 mags during the final years.

Blagorodnova et al. (2017) identified the progenitor star as an F-type giant with initial mass $M_{\mathrm{ZAMS}} = 18 \pm 1$ M$_\odot$, temperature $T = 6600 \pm 300$ K, radius $R = 220 \pm 13$ R$_\odot$ and luminosity $L = 8.8 \pm 0.8 \cdot 10^4$ L$_\odot$. It had cooled down to $T = 5800 \pm 120$ K and expanded to $R = 620 \pm 25$ R$_\odot$ 250 days before reaching the second peak brightness.

At the time of the second peak the temperature had dropped to 3300 K and the photosphere had expanded rapidly to $R = 6500 \pm 400$ R$_\odot$. After this the photospheric radius showed peculiar evolution. At the beginning of the first decline episode, the radius had diminished to $R = 4300$ R$_\odot$ after which it had expanded to $R = 5800$ R$_\odot$ at the beginning of the light curve plateau.

Spectral evolution of M101-OT is shown in Fig. 35. Several spectra, characterised

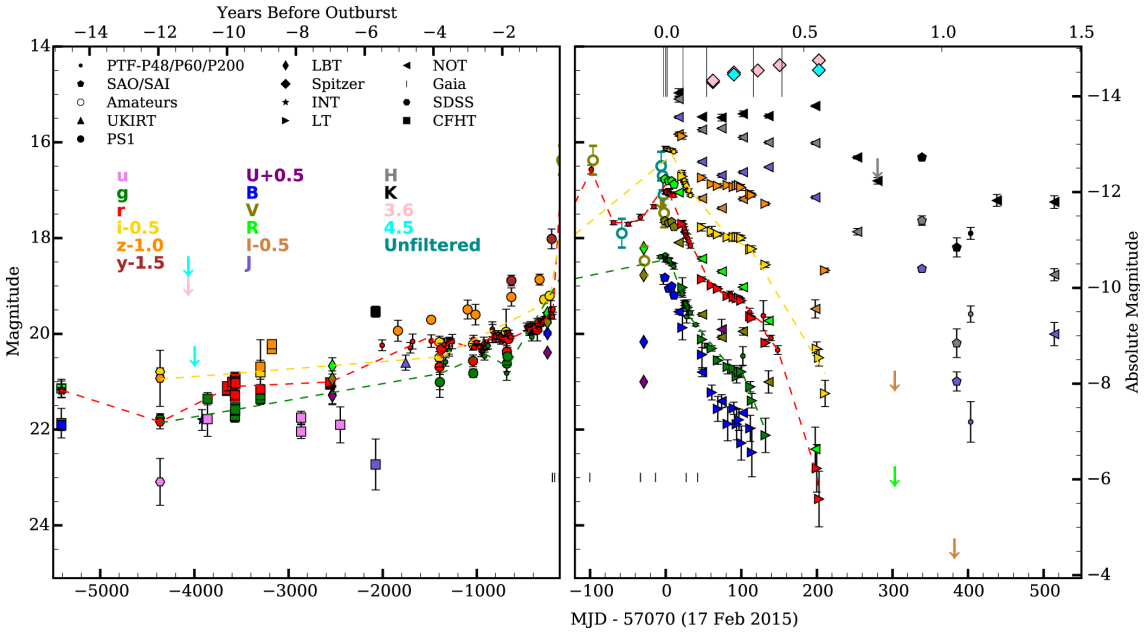

Figure 34. Light curves of M101-OT. Dashed lines are for guiding the eye. The origin is defined as the peak of the second brightening event. Note the different time scales. Adopted from Blagorodnova et al. (2017)

by red continua and narrow lines, were obtained. Observations spanned from around the second peak up until 153 days afterwards. At first, the Hα line shows prominent P Cygni absorption feature that, as time passes, vanishes and turns into a blueshifted emission component. Double-peaked Hα emission has been observed also in other LRNe and it can be interpreted as a sign of bipolar ejecta structure. Otherwise, the spectra are characterised by absorption forests of Fe II, Ti II and Sc II as well as lines of Ca II, Ba II, Mg I, Na I and K I with various strengths of P Cygni absorption. The latter lines implicate low expansion velocities of $v \approx 300$ km s^{-1}. Late-time spectra display molecular lines (typical for cool M-type stars) that point towards rapid dust formation.

One possible scenario to explain these observations is the ejection of a common envelope (CE) of a close binary star. The historical light curve suggests that the progenitor has not experienced any major mass loss episodes. Additionally, the possible binary companion is most likely far fainter in comparison. Slow cooling and expansion of the photosphere (which was observed during the final years before the outbursts) is normal for stars in transition from core H burning to He burning. A close companion would cause RLOF from

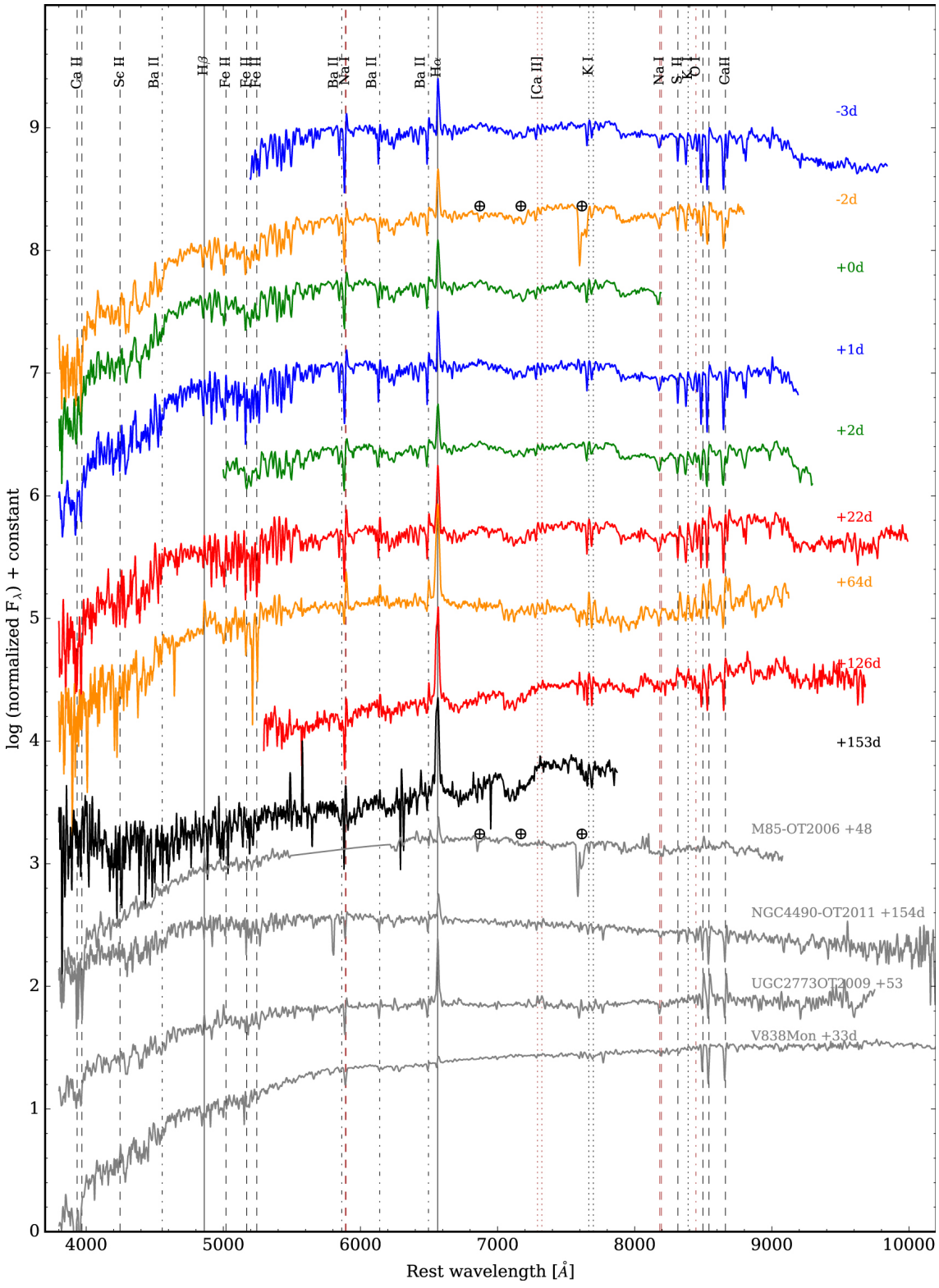

Figure 35. Spectral evolution of M101-OT compared to several other transients from the literature: LRNe NGC 4490-OT2011-1 and V838 Mon, SN 2008S-like M85-OT2006-1 and a dust-enshrouded LBV UGC2773-OT2009-1. Different colours indicate different telescope and instrument setups. Adopted from Blagorodnova et al. (2017)

the primary star and a CE is formed. Eventually, the CE is ejected (as suggested by the rapid expansion of the photoshpere) and a close binary or even stellar merger ensues. Unlike in the case of V838 Mon (see Section 3.3.1), the proposed companion star was not observable to begin with and, therefore, the outcome of M101-OT remains uncertain.

6.2.4 SN 2016bdu

The results of a SN 2009ip[39] -like object SN 2016bdu were published by Pastorello et al. (2018). The transient was discovered on 24 May 2016 and classified by the NUTS collaboration a few days later. As a part of the NUTS, my contribution was reducing all the near-IR data and triggering one epoch of optical ToO imaging.

The light curve comparison of SN 2016bdu to other SN 2009ip -like events is shown in Fig. 36. Similar to other transients of this class, the historical light curve of SN 2016bdu displays variability peaking in between $-14 < M_R\,[\mathrm{mag}] < -13$ throughout several years before the major Events A ($M_r \approx -15.3$ mag) and B ($M_r \approx -18.0$ mag). The evolution through Event A seems to vary from weeks to months from object to object. However, a fast rise to Event B maximum is observed in all objects. Additionally, SN 2016bdu displays similar post-maximum undulations during the Event B fading as was observed in SN 2009ip. This is likely due to CSM interaction. Furthermore, the late-time decline rate (see Fig. 5 in Pastorello et al. (2018)) suggests that the CSM interaction is still on-going during the late phases.

Spectral comparison of SN 2016bdu to other transients is shown in Fig. 37 (see also Fig. 6 in Pastorello et al. (2018)). The evolution of SN 2016bdu is reminiscent to SN 2009ip. Spectra observed shortly after the Event B maximum show SN IIn-like features: narrow emission lines of H (and He) on a hot continuum with a blackbody temperature of $T \approx 17000 \pm 1000$ K. As time passes, the narrow lines diminish in comparison to the emerging broader P Cygni components. Eventually, the P Cygni absorption components

[39] See Section 3.1.1.

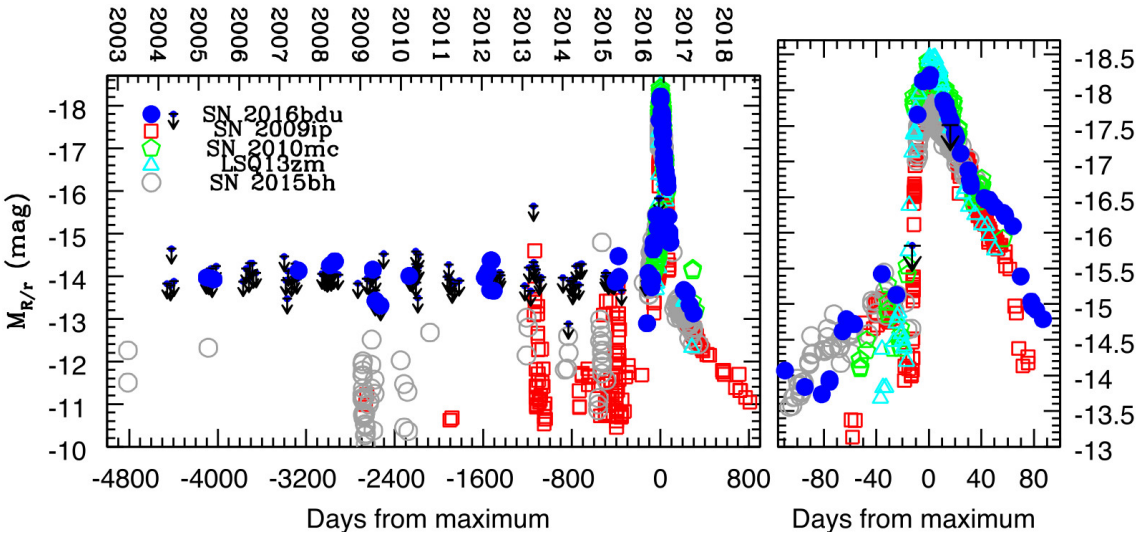

Figure 36. Light curve comparison of SN 2016bdu to other SN 2009ip -like transients. The years on top axis are for SN 2016bdu. The origin is at the event B maximum. There is no detections of progenitor variability for SN 2010mc and LSQ13zm prior to Event A. This is likely to be mostly due to the larger distance to their hosts. Adopted form Pastorello et al. (2018).

also vanish.

At first, the Hβ absorption minimum is blueshifted by $v \approx 3400$ km s^{-1}. In less than two weeks the minimum has moved to $v \approx 1900$ km s^{-1}. This can be explained as follows: a shell of CSM produced by the progenitor wind is swept-up by a fast-moving ejecta. The interaction shell slows down as time passes.

Pastorello et al. (2018) lists four plausible scenarios for SN 2016bdu and other SN 2009ip -like events.

1) A massive outburst (Event A) that collides with a previously ejected CSM shell (Event B).

2) A faint CCSN (A) whose ejecta interacts with the CSM (B).

3) An outburst (A) and a SN IIn explosion (B).

4) Binary interaction (A) and a merger (B).

The lack of nebular SN lines in the late-time spectra supports scenario 1) for SN 2016bdu. On the other hand, late-time decline in brightness shows no variability. This

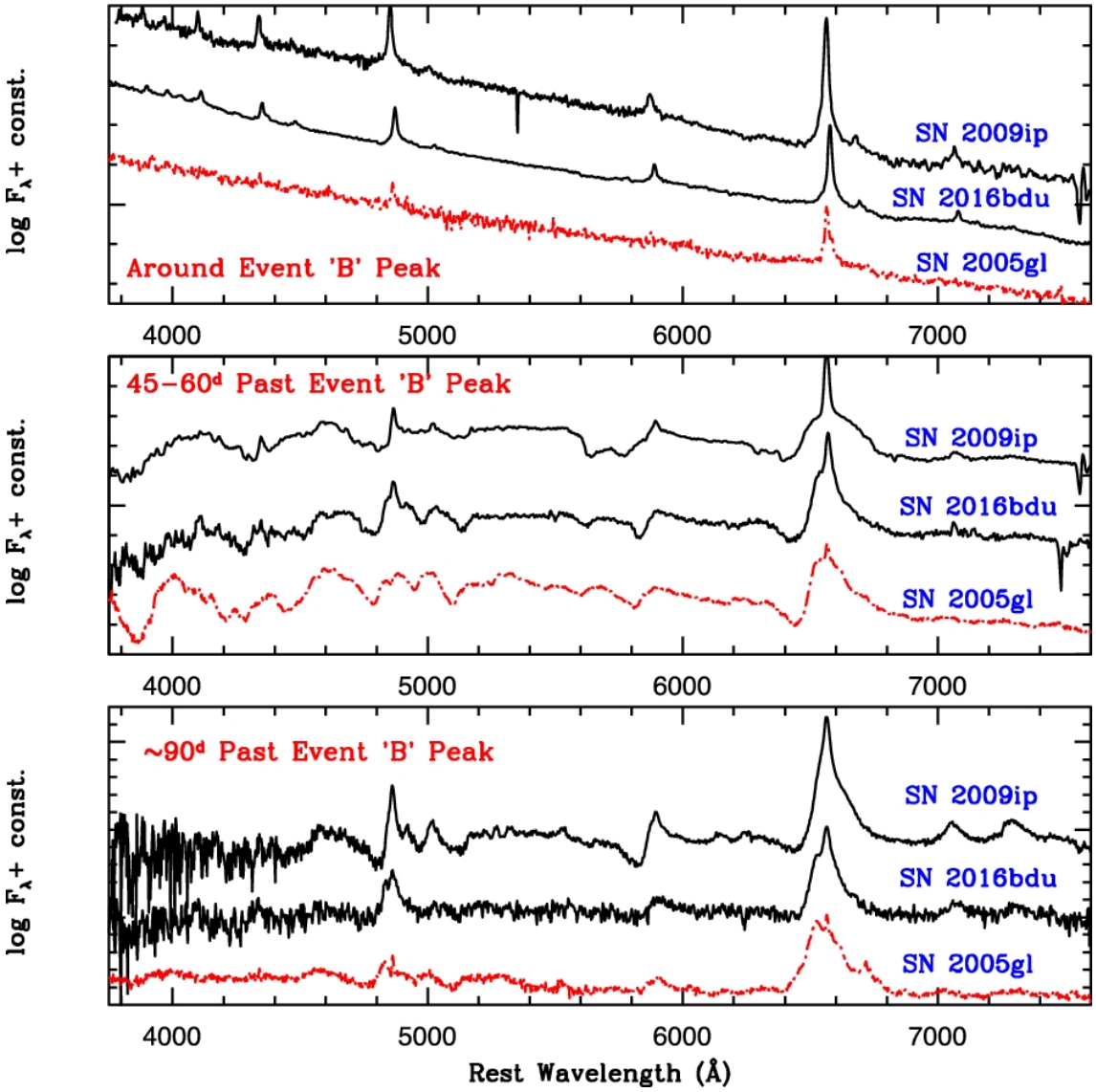

Figure 37. Spectral comparison of SN 2016bdu to SNe 2009ip and 2005gl at similar epochs. Adopted form Pastorello et al. (2018)

could imply that the progenitor star exploded as a genuine SN but it is also possible that the star just returned to a quiescent state. The brightness evolution of SN 2016bdu during the Event A is consistent with the light curves of sub-energetic CCSNe, such as SN 1987A. This points towards scenario 2). Because of the SN IIn-like features at around the maximum of Event B, scenario 3) is also plausible.

Scenario 4) could explain the historical variability of SN 2009ip -like events. A secondary star in a highly eccentric orbit can lead to mass ejections from a more massive

primary star during periastron passage interactions. However, stellar mergers tend to be less luminous (for the inferred primary mass) and spectroscopically evolve towards redder M-star-like objects or, in other words, LRNe than SN 2009ip -like transients.

6.2.5 AT 2017be

The results of an ILRT AT 2017be were published by Cai et al. (2018). The transient was discovered on 6 January 2017 and originally classified as an LBV outburst. I contributed by reducing four epochs of near-IR data.

The pseudo-bolometric light curve comparison of AT 2017be to other ILRTs is shown in Fig. 38. AT 2017be displays similar evolution to other ILRTs: a fast rise to brightness maximum ($M_r \approx -12$ mag) followed by sub-luminous SN II-like fading. A near-IR excess consistent with dusty environment typical for these type of transients is observed. The spectral energy distribution is well-fit (see Fig. 6 in Cai et al. (2018)) with two blackbody components: a hot one (transient) and a warm one (CSM dust). There is negligible temperature evolution in the warm component which further strengthens the interpretation of a dusty environment for AT 2017be.

The spectral evolution of AT 2017be is shown in Fig. 39. There is little evolution throughout the observed period. The spectra are characterised by a red continuum and narrow Balmer emission lines as well as lines of Ca II – emission of near-IR doublet and triplet and absorption of H & K lines. The Hα profiles (see Figures 12 and 13 in Cai et al. (2018)) are well-fit by a single component that suggests the interaction region is fairly uniform. A narrow P Cygni absorption feature ($v \lesssim 70$ km s^{-1}) is observed in the highest-resolution spectrum at epoch +30.2 d that implies slowly moving CSM.

The observed properties favour ECSN origin for AT 2017be. The light curves show an evolution that is similar to regular Type II SNe but at a lower luminosity. Unfortunately, the only constraint for the progenitor from archival data is an upper limit of $H = -10.1$ mag.

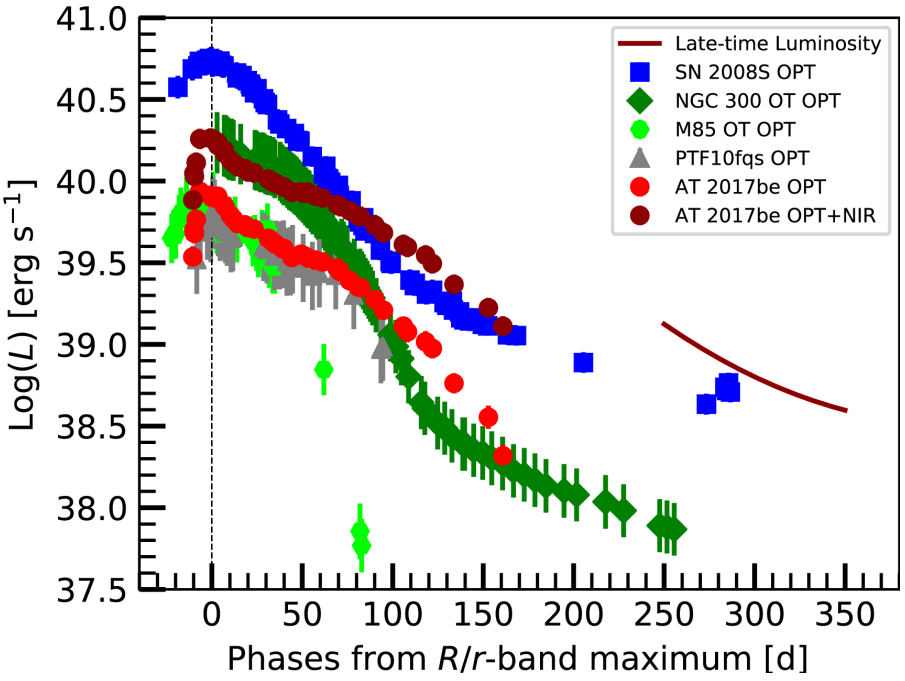

Figure 38. Pseudo-bolometric light curve comparison of ILRTs. The near-IR excess in AT 2017be is clearly visible. Adopted form Cai et al. (2018)

Although the evidence for ECSN scenario is scarce, the other ILOTs can be fairly confidently ruled out. If AT 2017be was a LRN, Ca II near-IR triplet absorption would have been observed. Additionally, no molecular bands were observed at the late times.

An impostor outburst is also an unlikely explanation as a bright progenitor star was not detected. Furthermore, the velocity of the CSM inferred from the P Cygni absorption fits slow stellar winds better than erratic eruptions of massive stars. This is further backed up by the lack of light curve undulations and symmetric line profiles: the CSM was probably uniform and, therefore, unlikely produced by outbursts.

6.3 Discussion

The spectral evolution of SNe 2015bh and 2016bdu could probably be reproduced with tweaked models of Dessart et al. (2016) (see Section 2.2). Model C/D with a less massive outer shell and/or asymmetries in the CSM could probably be used to model SN 2015bh whereas model A would suit SN 2016bdu better. Still, there is a need for more numeri-

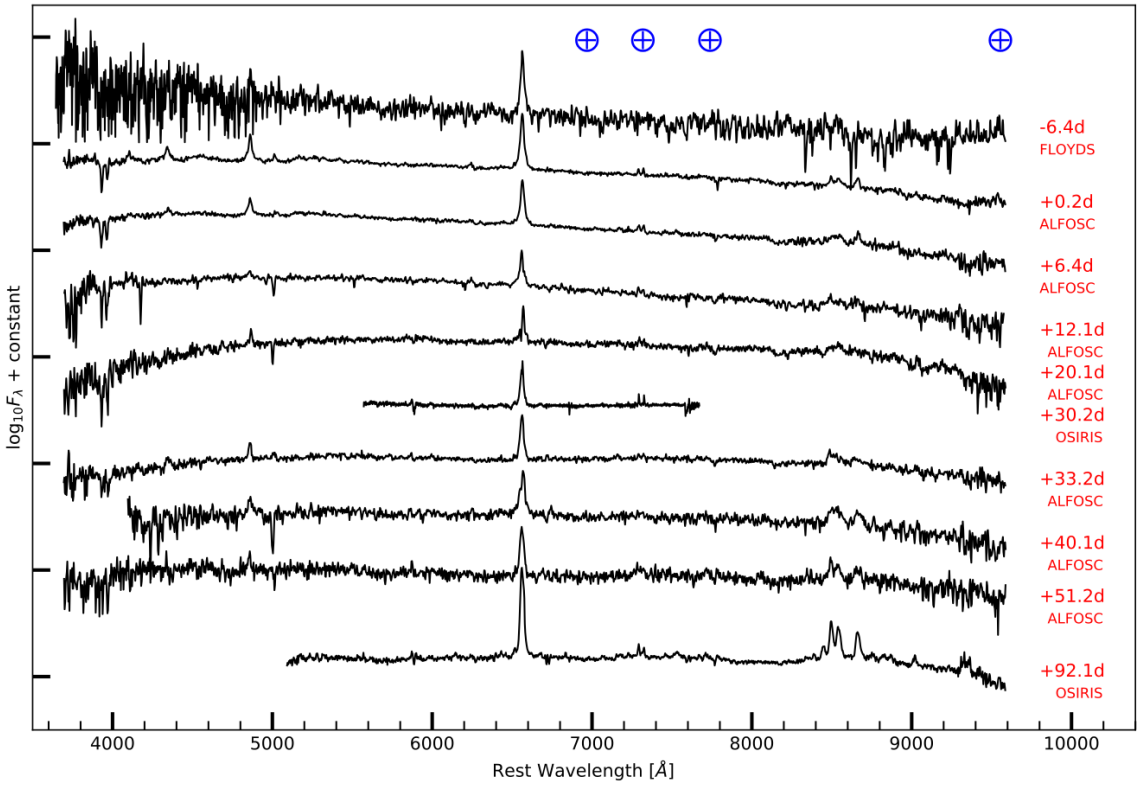

Figure 39. Spectral evolution of AT 2017be. Instrument used is shown below the epoch number. The blue symbols indicate the regions of the telluric spectral features. Adopted form Cai et al. (2018)

cal simulations for CSM interaction. Especially in case of non-spherical CSM structures observed in nature.

The number of SN 2009ip -like events discovered has increased during the recent years. Nevertheless, it is unclear whether or not they are produced by a terminal explosion of the progenitor star (SN IIn) or some other mechanism, such as shell-shell collisions of LBV outbursts (impostor outbursts). Or even combination of both.

As demonstrated by SNhunt248, not only LBVs but also other stars, namely YHGs, are able to produce SN impostor outbursts. Discovery and monitoring of these stars is essential to understand the late stages of stellar evolution of massive stars.

Transients AT 2017be and M101-OT were produced by completely different progenitor systems even though they were similarly red objects. Although the progenitor star of AT 2017be was not recovered from archival data, the observed properties favour terminal

Table II. Characteristic observables for each subclass of ILOTs.

Class	Progenitor	Characteristic features
SN impostor	Massive star (e.g. LBV, YHG)	Erratic variability prior to outburst
		Progenitor survives
ILRT	Sub-energetic SN + dusty CSM	IR excess of the progenitor system
		Ca doublet and triplet emission lines
		Terminal for the progenitor
LRN	Binary interaction	Ca triplet absorption lines
		Develops molecular lines
		Progenitors survive or merge

explosion of a single star in this case. On the other hand, the historical light curve and spectral evolution favour binary interaction model for M101-OT even when the probable secondary star was not observable.

Albeit the spectral features (such as narrow emission lines) and brightness evolution ($-15 \lesssim M_{peak}$ [mag] $\lesssim -10$) of ILOTs are similar, there are certain unique characteristics to each subclass as summarised in Table II. Additionally, archival data have a very important part also in ILOT research. Due to the fairly close proximity of these transients, the historical light curves and progenitor systems can sometimes be recovered. These are very important aspects when attempting to differentiate and understand these kinds of objects. Furthermore, due to the rarity of ILOTs, an increased effort should be placed on discovering and classifying as many nearby transients as possible. Even in my fairly targeted sample of 111 objects, only one ILOT (SN impostor) was classified.

7 Conclusions

Although more SN 2009ip -like transients have been discovered, it is still unclear whether or not these objects are produced by a terminal SN explosion or not. Additionally, there is a need for non-spherical numerical simulations for CSM interaction models.

Even though similar in many observables, ILOTs can be sub-classified based on their light curve and spectral evolution. For instance: SN impostors display erratic variability prior to outburst, ILRTs are surrounded by dusty environments and LRNe develop molecular lines in their late-time spectra. In many cases, archival data is essential in separating in between nearby transient types, especially if the progenitor properties can be recovered.

Generally, an observational effort should be made to classify more transients in order to gain better understanding of these astrophysical events.

References

Adams, S. M. et al., 2016, *MNRAS*, **460**, 1645

Afşar, M. & Bond, H. E., 2007, *AJ*, **133**, 387

Anderson, J. P., 2014, *ApJ*, **786**, 67

Arcavi, I. et al., 2012, *ApJL*, **756**, 30

Arcavi, I., 2017, *Handbook of Supernovae:* Hydrogen-rich Core Collapse Supernovae, arXiv:1710.03759 (Final draft)

Barbon, R. et al., 1979, *A&A*, **72**, 287

Blagorodnova, N. et al., 2017, *ApJ*, **834**, 107

Boian, I. & Groh, J. H., 2018, *A&A*, **617**, 115

Bond, H. E. et al., 2003, *Nature*, **422**, 405

Bond, H. et al., 2009, *ApJL*, **695**, L154

Bose, S. et al., 2015, *MNRAS*, **450**, 2373

Botticella, M. T. et al., 2009, *MNRAS*, **398**, 1041

Burrows, A., 2013, *Rev. Mod. Phys.*, **85**, 245

Buzzoni, B. et al., 1984, *The Messenger*, **38**, 9

Cai, Y-Z. et al., 2018, *MNRAS*, **480**, 3424

Cao, Y. et al., 2013, *ApJ*, **775**, L7

Chevalier, R. A. & Fransson C., 1985, *Lecture Notes in Physics*, **224**, *Berlin Springer Verlag*, in Supernovae as distance indicators: Supernova interaction with a circumstellar wind and the distance to SN 1979c

Chevalier, R. A., 1990, *Supernovae*, **91**, in Interaction of supernovae with circumstellar matter

Chevalier R. A. & Fransson, C., 2008, *ApJ*, **683**, L135

Chevalier, R. A. & Fransson C., 2016, *Handbook of Supernovae:* Thermal and non-thermal emission from circumstellar interaction, arXiv:1612.07459 (Final draft)

Chugai, N. N., 2001, *MNRAS*, **326**, 1448

Chugai, N. N. et al., 2004, *MNRAS*, **352**, 1213

Conti, P. S., 1984, *IAUS*, **105**, 233

Colgate, S. A. & McKee, C., 1969, *ApJ*, **157**, 623

de Jaeger, T et al., 2018, *MNRAS*, **476**, 4592

Dessart, L. et al., 2009, *MNRAS*, **394**, 21

Dessart, L. et al., 2016, *MNRAS*, **458**, 2094

Dhawan, S. et al., 2015, *MNRAS*, **448**, 1345

Djupvik A. A. & Andersen J., 2010, *ASSP*, **14**, 211

Duncan, R.C. & Thompson C., 1992, *ApJ*, **392**, L9

Elias-Rosa, N. et al., 2016, *MNRAS*, **463**, 3894

Faran, T. et al., 2014, *MNRAS*, **445**, 554

Fassia, A. et al., 2000, *MNRAS*, **318**, 1093

Fassia, A. et al., 2001, *MNRAS*, **325**, 907

Filippenko, A. V. et al., 1992a, *ApJ*, **384**, L37

Filippenko, A. V. et al., 1992b, *AJ*, **104**, 1543

Filippenko, A. V., 1997, *ARA&A*, **35**, 309

Fowler, W. A. & Hoyle, F., 1964, *ApJS*, **9**, 201

Fraser, M. et al., 2013, *MNRAS*, **433**, 1312

Fraser, M. et al., 2015, *MNRAS*, **453**, 3886

Galbany, L. et al., 2016, *AJ*, **151**, 33

Gal-Yam, A. et al., 2002, *MNRAS*, **332**, L73

Gal-Yam, A. et al., 2007, *ApJ*, **656**, 372

Gal-Yam, A. et al., 2011, *ApJ*, **736**, 159

Gal-Yam, A. et al., 2012, *Science*, **337**, 927

Gal-Yam, A., 2016, *Handbook of Supernovae:* Observational and Physical Classification of Supernovae, arXiv:1611.09353 (Final draft)

Gezari, S. et al., 2009, *ApJ*, **690**, 1313

Gezari, S. et al., 2015, *ApJ*, **804**, 28

Graham, M. L. et al., 2014, *ApJ*, **787**, 163

Graham, M. L. et al., 2017, *MNRAS*, **469**, 1559

Hamuy, M. et al., 2001, *ApJ*, **558**, 615

Heger, A. & Woosley, S. E., 2002, *ApJ*, **567**, 532

Herwig, F., 2002, *ARA&A*, **43**, 435

Hicken, M. et al., 2009, *ApJ*, **700**, 331

Hillebrandt, W. & Niemeyer, J. C., 2000, *ARA&A*, **38**, 191

Hirata, K., 1987, *Phys. Rev. Lett.*, **58**, 1490

Ho, W. C. G. et al., 2001, *PASP*, **113**, 1349

Ivanov, M. A. & Shulman, G. A., 1990, *SvA*, **34**, 163

Humphreys, R. M. & Davidson, K., 1994, *PASP*, **106**, 1025

Humphreys, R. M. et al., 1999, *PASP*, **111**, 1124

Janka, H.-Th., 2017, *Handbook of Supernovae:* Neutrino-driven Explosions, arXiv:1702.08825 (Final draft)

Kangas, T. et al., 2016, *MNRAS*, **456**, 323

Kankare, E. et al., 2012, *MNRAS*, **424**, 855

Kankare, E. et al., 2015, *A&A*, **581**, L4

Kasen, D. & Bildsten, L., 2010, *ApJ*, **717**, 245

Kasliwal, M. M., 2012, *PASA*, **29**, 482

Kiewe, M. et al., 2012, *ApJ*, **744**, 10

Koenigsberger, G. et al., 1998, *ApJ*, **499**, 889

Kulnari, S. R. et al., 2007, *Nature*, **447**, 458

Langer, N., 2012, *ARA&A*, **50**, 107

Laughlin, G. et al., 1997, *ApJ*, **482**, 420

Leonard, D. C. et al., 2000, *ApJ*, **536**, 239

Leonard, D. C. et al., 2002, *PASP*, **114**, 35

Li, W. et al., 2011a, *MNRAS*, **412**, 1441

Li, W. et al., 2011b, *MNRAS*, **412**, 1473

Lipunov, V. M. et al., 2017, *MNRAS*, **470**, 2339

Liu, Q.-Z. et al., 2000, *A&AS*, **144**, 219

MacLeod, M. et al., 2017, *ApJ*, **835**, 282

Maoz, D. et al., 2014, *ARA&A*, **52**, 107

Margutti, R., 2014, *ApJ*, **780**, 21

Mattila, S. et al., 2018, *Science*, **361**, 482

Mauerhan, J. C. et al., 2013, *MNRAS*, **430**, 1801

Mauerhan, J. C. et al., 2014, *MNRAS*, **442**, 1166

Mauerhan, J. C. et al., 2015, *MNRAS*, **447**, 1922

Mauerhan, J. C. et al., 2018, *MNRAS*, **473**, 3765

Mazzali, P.A. et al., 2014, *MNRAS*, **439**, 1959

Minkowski, R., 1941, *PASP*, **53**, 224

Modjaz, M. et al., 2009, *ApJ*, **702**, 226

Moriya, T. J. et al., 2014, *A&A*, **569**, 57

Munari, U. et al., 2002, *A&A*, **389**, L51

Munari, U. et al., 2005, *A&A*, **434**, 1107

Nomoto, K., 1987, *ApJ*, **322**, 206

Ofek, E. O. et al., 2013, *ApJ*, **768**, 47

Oliva, E., 1997, *A&AS*, **123**, 589

Pastorello, A. et al., 2004, *MNRAS*, **347**, 74

Pastorello, A. et al., 2009, *MNRAS*, **394**, 2266

Pastorello, A. et al., 2010, *MNRAS*, **408**, 181

Pastorello, A. et al., 2013, *ApJ*, **767**, 1

Pastorello, A. et al., 2016, *MNRAS*, **456**, 853

Pastorello, A. et al., 2018, *MNRAS*, **474**, 197

Pastorello, A. & Fraser, M., 2019a, *NatAs*, **3**, 676

Pastorello, A. et al., 2019b, *A&A*, **630**, 75

Patat, F. et al., 2001, *ApJ*, **555**, 900

Perlmutter, S et al., 1999, *ApJ*, **517**, 565

Pian, E. et al., 2006, *Nature*, **442**, 1011

Prieto, J. et al., 2008, *ApJ*, **681**, L9

Prieto, J. et al., 2013, *ApJ*, **763**, L27

Pun, J. et al., 1995, *ApJS*, **99**, 223

Quimby, R. M. et al., 2011, *Nature*, **474**, 487

Richmond, M. W. et al., 1994, *AJ*, **107**, 1022

Riess, A. G. et al., 1998, *AJ*, **116**, 1009

Rosero-Rueda, V. A. et al., 2008, *Rev. Mex. Astron. Astrofis.*, **34**, 135

Rubin, A. et al., 2016, *ApJ*, **820**, 33

Sanders, N. E. et al., 2015, *ApJ*, **799**, 208

Schlegel, E. M., 1990, *MNRAS*, **244**, 269

Schlegel, E. M. et al., 1996, *AJ*, **111**, 2038

Seward, F. D., 2001, *ApJ*, **553**, 832

Smartt, S. J., 2009, *ARA&A*, **47**, 63

Smartt, S. et al., 2017, *Nature*, **551**, 75

Smith, N. et al., 2003, *AJ*, **125**, 1458

Smith, N., 2008, *Nature*, **455**, 201

Smith, N. et al., 2009, *ApJ*, **697**, L49

Smith, N. et al., 2010, *AJ*, **139**, 1451

Smith, N. et al., 2011, *MNRAS*, **415**, 773

Smith, N. et al., 2013, *MNRAS*, **434**, 2721

Smith, N. et al., 2014, *MNRAS*, **438**, 1191

Smith, N., 2016a, *Handbook of Supernovae:* Interacting Supernovae: Types IIn and Ibn, arXiv:1612.02006 (Final draft)

Smith, N. et al., 2016b, *MNRAS*, **463**, 2904

Smith, N. et al., 2016c, *MNRAS*, **458**, 950

Soker, N., 2010, *MNRAS*, **401**, 2793

Snodgrass, C. et al., 2008, *The Messenger*, **132**, 18

Soker, N. & Kashi, A., 2013, *ApJ*, **764**, L6

Sollerman, J. et al., 1998, *ApJ*, **493**, 933

Sparks, W. B. et al., 2008, *ApJ*, **135**, 605

Taddia, F. et al., 2016, *A&A*, **558**, A5

Tammann, G. A. & Sandage, A., 1968, *ApJ*, **151**, 825

Taubenberger, S. et al., 2006, *MNRAS*, **371**, 1459

Thompson, T. A. et al., 2009, *ApJ*, **705**, 1364

Thöne, C. C. et al., 2017, *A&A*, **599**, 129

Turatto, M. et al., 1993, *MNRAS*, **262**, 128

Tylenda, R. et al., 2011a, *A&A*, **528**, 114

Tylenda, R. et al., 2011b, *A&A*, **532**, 138

Valenti, S. et al., 2008, *ApJL*, **673**, L155

Valenti, S. et al., 2016, *MNRAS*, **459**, 3939

Van Dyk, S. D. et al., 2000, *PASP*, **112**, 1532

Van Dyk, S. D. et al., 2006, arxiv:astro-ph/0603025

Vreeswijk, P. M. et al., 2014, *ApJ*, **797**, 24

Yaron, O. & Gal-Yam, A., 2012, *PASP*, **124**, 668

Zhang, T. et al., 2012, *AJ*, **144**, 131

Appendices

A Transient classifications

All classifications I contributed for are listed in Table III. First author ATel numbers are written in boldface. Lines missing an ATel number belong to the same ATel(s) as the above one(s). Object names are from the first discovery (in other words, survey or similar names). Certain long names marked with an asterisk are truncated and fully given at the end of the table. Type *Unknown* usually means poor signal-to-noise meaning that secure classification was not possible. Type *Stellar* is a Milky Way object, such as a cataclysmic variable or a variable star.

Table III: List of classifications in chronological order.

ATel #	Object	RA	DEC	Type	z	Programme
7233	PSN J13215756*	13:21:57.56	+38:43:22.9	SN Impostor	–	NOT-TNG
7378	Gaia15acz	09:11:01.62	+34:44:27.2	SN II	0.018	NOT-GAIA
	Gaia15aek	06:47:02.70	+64:56:03.7	SN II	0.012	NOT-GAIA
7448	Gaia15aem	15:04:30.75	+21:59:16.7	SN Ia	0.050	NOT-GAIA
7530	Gaia15aev	13:21:55.23	+35:21:32.0	SN IIn	0.020	NOT-GAIA
7628	Gaia15afx	11:09:31.15	+04:09:47.4	SN Ia	0.052	NOT-GAIA
	Gaia15agd	11:26:17.38	+28:22:02.0	SN II	0.030	NOT-GAIA
7913	ASASSN-15od	02:23:13.21	-04:31:02.1	SN Ia	0.018	OTHER
7951	PSN J20150317*	20:15:03.17	-19:59:46.2	SN IIP	0.016	NOT-TNG
8255	PS15crs	21:23:30.80	-07:44:47.8	SN II	0.028	PESSTO
	PS15crp	01:22:24.74	-13:47:35.0	SN Ia	0.047	PESSTO
	PS15coo	02:59:30.75	-08:13:10.5	SN Ia	0.030	PESSTO
	OGLE15om	03:19:00.00	-64:40:40.2	SN Ia	0.100	PESSTO
8264	PS15csd	02:04:55.53	+18:48:15.0	SN Ia	0.044	PESSTO
	PS15csf	02:26:02.24	+17:03:40.4	SN II	0.021	PESSTO
8268	ASASSN-15sh	19:32:06.94	-62:26:31.5	SN Ia	0.033	PESSTO

Continues in the next page

Table III – continued

ATel #	Object	RA	DEC	Type	z	Programme
	CSS151109-03*	03:26:47.31	-16:35:37.9	SN Ia	0.134	PESSTO
	CSS151109-10*	10:15:02.42	+07:48:30.1	SN Ia	0.027	PESSTO
	OGLE15ng	00:22:19.88	-75:12:26.3	SN Ia	0.079	PESSTO
	OGLE15oa	04:36:25.63	-62:47:51.7	SN Ia	0.059	PESSTO
	OGLE15pf	05:17:12.37	-71:52:39.6	SN II	0.018	PESSTO
	PS15cox	03:08:04.79	-03:14:54.2	SN Ia	0.031	PESSTO
	PS15ctg	04:13:58.45	+02:08:43.0	SN Ia	0.078	PESSTO
	PS15ctw	22:52:05.94	-05:50:50.0	SN Ia	0.089	PESSTO
8292	OGLE15rc	04:59:27.51	-60:16:46.5	SN Ia	0.072	PESSTO
8296	LSQ15bon	00:48:08.67	-29:08:22.9	SN Ia	0.060	PESSTO
	OGLE15qk	03:30:00.33	-71:30:08.6	SN Ia	0.065	PESSTO
	OGLE15qz	03:08:35.88	-70:30:41.6	SLSN Ic	0.063	PESSTO
	OGLE15rb	05:12:52.03	-61:52:00.3	SN Ic	0.028	PESSTO
	PS15cmq	09:48:22.98	-03:27:41.2	SN II	0.065	PESSTO
	PS15cvn	00:09:21.67	-00:04:06.5	SN Ic	0.065	PESSTO
	PS15cwj	09:27:44.88	-08:31:32.1	SN Ia	0.135	PESSTO
	PS15cwo	03:11:16.73	+01:11:34.5	SN II	0.020	PESSTO
8306	LSQ15bor	02:43:16.08	-18:10:52.5	SN II	0.055	PESSTO
	LSQ15bpd	05:02:46.69	-18:32:11.1	SN Ia	0.081	PESSTO
	PSN J22305942*	22:30:59.41	-13:59:56.1	SN IIb	0.016	PESSTO
	OGLE15rd	00:29:34.51	-67:59:52.2	Unknown	–	PESSTO
	PS15cwi	09:21:31.27	+05:10:26.7	SN II	0.058	PESSTO
	PS15cwz	23:52:09.61	-29:04:44.6	SN Ia	0.039	PESSTO
8320	PS15cwb	10:16:21.57	-11:00:10.5	SN Ia	0.145	PESSTO
	OGLE15rw	06:27:24.94	-67:31:50.0	SN Ia	0.071	PESSTO
	CSS151120*	04:45:25.70	-19:01:57.5	SN Ia	0.073	PESSTO
8325	ASASSN-15ta	20:29:33.02	-61:57:03.4	SN Ib	0.015	PESSTO
	LSQ15bpg	02:41:06.90	-29:32:34.1	Unknown	–	PESSTO
	PS15cww	04:56:33.69	+04:45:26.2	SN IIn	0.063	PESSTO
	PSN J20293645*	20:29:36.44	-43:50:27.7	SN Ic	0.023	PESSTO

Continues in the next page

Table III – continued

ATel #	Object	RA	DEC	Type	z	Programme
8419	ASASSN-15ub	11:07:13.07	+65:05:58.2	SN Ia	0.032	OTHER
8669	Gaia16aax	14:34:18.47	+49:12:36.5	AGN	0.249	NOT-GAIA
8992	Gaia16akk	09:09:51.10	+47:53:48.0	SN Ia	0.115	NUTS
	ASASSN-16ek	07:20:24.30	+32:51:01.2	SN IIb	0.014	NUTS
	ASASSN-16eq	22:04:35.56	+42:19:32.7	SN Ia	0.026	NUTS
9024	ASASSN-16ex	17:10:23.92	+26:23:47.9	SN Ia-pec	0.030	NUTS
9060	ASASSN-16fc	15:31:51.24	+37:24:47.9	SN Ia	0.030	NUTS
	Gaia16aou	11:28:55.70	+25:51:40.8	SN Ia	0.033	NUTS
9071	Gaia16apd	12:02:51.70	+44:15:27.4	SLSN-I	0.102	NUTS
9090	ASASSN-16fp	21:59:04.14	+18:11:10.5	SN Ic-BL	0.004	NUTS
9111	SN2016bdu	13:10:13.95	+32:31:14.1	SN IIn	0.017	NUTS
9208	ASASSN-16gn	12:06:57.59	+27:18:04.9	SN IIn	0.056	NUTS
9326	ASASSN-16hy	15:26:29.54	+41:44:03.9	SN II	0.008	NUTS
9368	ASASSN-16io	18:40:00.93	+54:13:04.9	SN Ia	0.037	NUTS
	ASASSN-16ip	02:27:21.70	-23:55:45.3	SN Ia	0.017	NUTS
9421	Gaia16bba	01:01:35.50	+17:06:04.3	SN Ia	0.034	NUTS
	Gaia16bbk	01:19:45.40	+09:53:42.6	SN Ia	0.027	NUTS
9454	SN2016fqr	02:52:51.03	+42:12:25.7	SN II	0.012	NUTS
9498	SN2016gfy	07:26:43.67	+85:45:51.7	SN II	0.008	NUTS
9580	Gaia16bjx	14:32:41.46	+52:04:50.8	SN Ia	0.086	NUTS
9585	Gaia16bji	17:20:57.55	+24:54:35.3	SN Ia	0.060	NUTS
9610	ASASSN-16lg	17:48:12.38	+17:37:31.6	SN Ia	0.021	NUTS
	ASASSN-16ll	19:00:32.43	+54:34:09.7	SN II	0.026	NUTS
	SN2016gsd	02:40:34.44	+19:16:59.9	SN II	0.060	NUTS
	Gaia16bhj	04:27:03.26	-06:10:24.2	SN Ia	0.031	NUTS
9630	ASASSN-16lm	09:03:34.50	+41:42:45.5	SN Ia	0.040	NUTS
	SN2016hbd	02:56:06.20	+27:42:05.6	SN IIP	0.022	NUTS
9645	CSS161010*	04:58:34.00	-08:18:03.0	Unknown	–	NUTS
	SN2016gxp	00:14:34.65	+48:15:08.1	SN Ia-pec	0.018	NUTS
9734	ASASSN-16na	04:09:10.24	+21:26:25.5	SN Ia	–	OTHER

Continues in the next page

Table III – continued

ATel #	Object	RA	DEC	Type	z	Programme
9834	Gaia16byj	12:28:52.64	-11:38:59.7	SN II	0.017	NUTS
9836	Gaia16buy	21:22:25.19	-11:56:54.8	SN IIn	0.066	NUTS
	ASASSN-16oo	01:41:18.54	-00:12:37.5	SN Ia	0.055	NUTS
9844	Gaia16car	01:29:04.62	+40:21:49.4	SN Ia	0.053	NUTS
	Gaia16cay	13:13:26.59	+27:48:24.6	SN Ia	0.021	NUTS
9933	ATLAS16dzn	07:00:00.59	+57:05:35.0	Stellar	0.00	NUTS
	ATLAS16ebo	22:18:36.62	+40:49:20.3	Stellar	0.00	NUTS
9985	Gaia17abx	15:31:36.79	+25:14:32.9	SN Ia	0.033	NUTS
9990	Gaia17acy	05:00:06.77	-13:08:31.6	Unknown	0.175	NUTS
	Gaia17aea	09:44:25.70	-18:32:54.0	SN Ia	0.050	NUTS
	Gaia16aej	06:14:12.95	-16:33:45.7	CV	0.00	NUTS
	ATLAS17air	00:57:31.90	+30:11:06.8	SN Ia	0.020	NUTS
10202	SN2017cjb	12:53:50.45	+09:42:17.7	SN II	0.009	NUTS
10213	Gaia17aqn	10:38:46.17	+11:23:50.5	SN Ia	0.062	NUTS
10594	ATLAS17hpc	13:19:03.90	-02:30:45.8	SN II	0.018	NUTS
10823	ASASSN-17nb	07:27:37.32	+35:36:28.4	SN II	0.016	NUTS
	CSS170922*	17:25:46.00	+34:22:49.0	SN Ia	0.065	NUTS
11021	ASASSN-17pi	08:57:28.63	+28:36:59.9	SN Ia	0.048	NUTS
11153	PS18ao	23:18:09.75	+21:25:54.5	SN Ia	0.102	NUTS
11164	Gaia18ack	13:28:24.43	+67:43:03.8	SN Ia	0.055	NUTS
	ATLAS18abb	22:57:46.61	+25:38:33.6	SN Ic	0.025	NUTS
11305	ASASSN-18bq	18:01:01.06	+61:41:45.0	SN IIb	0.035	NUTS
11891	ATLAS18sld	20:41:54.99	+64:12:52.7	SN Ic-BL	0.025	NUTS
12075	Gaia18cug	03:11:18.72	+01:19:00.8	SN II	0.032	ePESSTO
	ASASSN-18wf	00:49:47.24	-61:39:12.9	SN Ia	0.035	ePESSTO
12096	Gaia18cwt	01:05:20.52	-47:11:34.6	SN Ib/c	0.022	ePESSTO
	ASASSN-18xg	02:13:45.05	+04:06:08.3	SN Ic	0.011	ePESSTO
12107	Gaia18cqs	04:25:03.01	-14:36:47.9	SN Ic	0.018	ePESSTO
	ATLAS18wcg	03:38:40.32	+07:39:49.4	SN Ia	0.034	ePESSTO
	ASASSN-18xn	09:30:55.10	-04:34:16.3	SN Ia-91T	0.023	ePESSTO

Continues in the next page

Table III – continued

ATel #	Object	RA	DEC	Type	z	Programme
12130	Gaia18dbj	08:36:39.72	+01:07:06.4	AGN	0.201	ePESSTO
	ASASSN-18yb	02:38:22.78	-11:44:21.0	SN Ia-91bg	0.027	ePESSTO
12132	ASASSN-18xy	07:53:02.17	+07:16:31.5	SN Ia-91T	0.038	ePESSTO
	KAIT-18av	03:39:28.10	-13:07:01.9	SN II	0.014	ePESSTO
12134	ASASSN-18xb	08:20:25.90	-65:20:31.7	SN Ia-91T	0.035	ePESSTO

PSNJ 13215756: PSN J13215756+3843229

PSN J20150317: PSN J20150317-1959462

CSS151109-03: CSS151109-032647-163538

CSS151109-10: CSS151109-101502+074830

PSN J22305942: PSN J22305942-1359561

CSS151120: CSS151120-044526-190158

PSN J20293645: PSN J20293645-4350277

CSS161010: CSS161010:045834-081803

CSS170922: CSS170922:172546+342249

B Journal articles

All articles (published or submitted in between 2015 and 2019) I have contributed to are listed below in chronological order. In most cases my contribution has been collecting and/or processing data of a particular object described in the article. In cases of entries 15, 17, 20, 21, 23, 26, 27 and 28 the co-authorship was based on the internal (e)PESSTO publication policy. Arxiv e-prints indicate articles under review process.

1. Onori et al. (2019), *Monthly Notices of the Royal Astronomical Society*, **489**, 1463: Optical follow-up of the tidal disruption event iPTF16fnl: new insights from X-shooter observations

2. Terreran et al. (2019), *The Astrophysical Journal*, **883**, 147: SN 2016coi (ASASSN-16fp): An Energetic H-stripped Core-collapse Supernova from a Massive Stellar Progenitor with Large Mass Loss

3. Galbany et al. (2019), *Astronomy and Astrophysics*, **630**, A76: Evidence for a Chandrasekhar-mass explosion in the Ca-strong 1991bg-like type Ia supernova 2016hnk

4. Reynolds et al. (2019), *arXiv e-prints*, **a**rXiv:1909.13617: SN 2016gsd: An unusually luminous and linear type II supernova with high velocities

5. Tartaglia et al. (2019), *arXiv e-prints*, **a**rXiv:1908.08580: The long-lived Type IIn SN 2015da: Infrared echoes and strong interaction within an extended massive shell

6. Prentice et al. (2019), *Monthly Notices of the Royal Astronomical Society*, **485**, 1559: Investigating the properties of stripped-envelope supernovae; what are the implications for their progenitors?

7. Cai et al. (2018), *Monthly Notices of the Royal Astronomical Society*, **480**, 3424: AT 2017be - a new member of the class of intermediate-luminosity red transients

8. Banerjee et al. (2018), *The Astrophysical Journal*, **867**, 99: Unraveling the Infrared Transient VVV-WIT-06: The Case for the Origin as a Classical Nova

9. Dey et al. (2018), *The Astrophysical Journal*, **866**, 11: Authenticating the Presence of a Relativistic Massive Black Hole Binary in OJ 287 Using Its General Relativity Centenary Flare: Improved Orbital Parameters

10. Banerjee et al. (2018), *arXiv e-prints*, **arXiv:1809.06801**: Unravelling the infrared transient VVV-WIT-06: the case for an origin in a classical nova

11. Mattila et al. (2018), *Science*, **361**, 482: A dust-enshrouded tidal disruption event with a resolved radio jet in a galaxy merger

12. Goyal et al. (2018), *The Astrophysical Journal*, **863**, 175: Stochastic Modeling of Multiwavelength Variability of the Classical BL Lac Object OJ 287 on Timescales Ranging from Decades to Hours

13. Pastorello et al. (2018), *Monthly Notices of the Royal Astronomical Society*, **474**, 197: Supernovae 2016bdu and 2005gl, and their link with SN 2009ip-like transients: another piece of the puzzle

14. Tartaglia et al. (2018), *The Astrophysical Journal*, **853**, 62: The Early Detection and Follow-up of the Highly Obscured Type II Supernova 2016ija/DLT16am

15. Smartt et al. (2017), *Nature*, **551**, 75: A kilonova as the electromagnetic counterpart to a gravitational-wave source

16. Kankare et al. (2017), *Nature Astronomy*, **1**, 865: A population of highly energetic transient events in the centres of active galaxies

17. Abbott et al. (2017), *The Astrophysical Journal*, **848**, L12: Multi-messenger Observations of a Binary Neutron Star Merger

18. Kangas et al. (2017), *Monthly Notices of the Royal Astronomical Society*, **469**, 1246: Gaia16apd - a link between fast and slowly declining type I superluminous supernovae

19. Blagorodnova et al. (2017), *The Astrophysical Journal*, **834**, 107: Common Envelope Ejection for a Luminous Red Nova in M101

20. Leloudas et al. (2016), *Nature Astronomy*, **1**, 0034: Corrigendum: The superluminous transient ASASSN-15lh as a tidal disruption event from a Kerr black hole

21. Leloudas et al. (2016), *Nature Astronomy*, **1**, 0002: The superluminous transient ASASSN-15lh as a tidal disruption event from a Kerr black hole

22. Elias-Rosa et al. (2016), *Monthly Notices of the Royal Astronomical Society*, **463**, 3894: Dead or Alive? Long-term evolution of SN 2015bh (SNhunt275)

23. Smartt et al. (2016), *Monthly Notices of the Royal Astronomical Society*, **462**, 4094: Pan-STARRS and PESSTO search for an optical counterpart to the LIGO gravitational-wave source GW150914

24. Herczeg et al. (2016), *The Astrophysical Journal*, **831**, 133: The Eruption of the Candidate Young Star ASASSN-15QI

25. Zola et al. (2016), *Galaxies*, **4**, 41: A Search for QPOs in the Blazar OJ287: Preliminary Results from the 2015/2016 Observing Campaign

26. Smartt et al. (2016), *The Astrophysical Journal*, **827**, L40: A Search for an Optical Counterpart to the Gravitational-wave Event GW151226

27. Abbott et al. (2016), *The Astrophysical Journal Supplement Series*, **225**, 8: Supplement: "Localization and Broadband Follow-up of the Gravitational-wave Transient GW150914" (2016, ApJL, 826, L13)

28. Abbott et al. (2016), *The Astrophysical Journal*, **826**, L13: Localization and Broadband Follow-up of the Gravitational-wave Transient GW150914

29. Nicholl et al. (2016), *The Astrophysical Journal*, **826**, 39: SN 2015BN: A Detailed Multi-wavelength View of a Nearby Superluminous Supernova

30. Tomasella et al. (2016), *Monthly Notices of the Royal Astronomical Society*, **459**, 1018: Optical and near-infrared observations of SN 2014ck: an outlier among the Type Iax supernovae

31. Reed et al. (2016), *Monthly Notices of the Royal Astronomical Society*, **458**, 1417: A pulsation analysis of K2 observations of the subdwarf B star PG 1142-037 during Campaign 1: A subsynchronously rotating ellipsoidal variable

32. Valtonen et al. (2016), *The Astrophysical Journal*, **819**, L37: Primary Black Hole Spin in OJ 287 as Determined by the General Relativity Centenary Flare

33. Kangas et al. (2016), *Monthly Notices of the Royal Astronomical Society*, **456**, 323: Supernova 2013fc in a circumnuclear ring of a luminous infrared galaxy: the big brother of SN 1998S

34. Kankare et al. (2015), *Astronomy and Astrophysics*, **581**, L4: On the triple peaks of SNHunt248 in NGC 5806